Variation in powder size distribution for electron beam melting of Ti48Al2Cr2Nb - density and surface roughness effects

by

Tomisin Oluwajuyigbe

A thesis

presented to the University of Waterloo

in fulfillment of the

thesis requirement for the degree of

Master of Applied Science

in

Mechanical and Mechatronics Engineering

Waterloo, Ontario, Canada, 2024

© Tomisin Oluwajuyigbe 2024

Author's Declaration

This thesis consists of material all of which I authored or co-authored: see Statement of Contributions included in the thesis. This is a true copy of the thesis, including any required final revisions, as accepted by my examiners.

I understand that my thesis may be made electronically available to the public.

Statement of Contribution

Chapter 2 of my thesis contains information that is intended to be included in an article. This article is co-authored by myself, Prof. Mihaela Vlasea, Prof. Paria Karimi, Prof. Mohsen Keshavarz and Dr. Mahdi Habibnejad-korayem. In this chapter, I made significant contributions by analyzing powder characterization methods and conducting post-processing on the data, interpreted the results and wrote the chapter. Prof. Mihaela Vlasea, Prof. Paria Karimi, Prof. Mohsen Keshavarz and Dr. Madi Habibnejad-korayem reviewed and provided feedback on the article content. I will be the first author on this work.

Chapter 3 of my thesis contains an article co-authored by myself, Prof. Mihaela Vlasea, Prof. Paria Karimi, Prof. Mohsen Keshavarz, and Dr. Mahdi Habibnejad-korayem. In this chapter, Prof. Karimi and I were involved in developing and executing the experimental plan. My direct contribution involved data processing, characterization design, post-processing of data, interpretation of results, in-depth discussion, and writing the article. Dr. Habibnejad-korayem and Prof. Vlasea conceptualized the article's objective and design, and Prof. Vlasea was involved in reviewing the interpreted results and overall experiment design. Prof. Karimi, Prof. Vlasea, Prof. Keshavarz, and Dr. Habibnejad-korayem reviewed and edited the content of the article. I will be the first author on this work.

Information from Chapter 4 of my thesis is meant to be published in an article. Myself with Prof. Mihaela Vlasea, Prof. Paria Karimi, Prof. Mohsen Keshavarz, and Dr. Mahdi Habibnejad-korayem, will coauthor this anticipated article. I directly contributed to the creation of the experimental strategy, data processing, characterisation design, data post-processing, result interpretation, in-depth discussion, and article writing in this chapter. The goals and layout of the article were conceptualized with contributions from Dr. Habibnejad-korayem and Prof. Vlasea. Prof. Vlasea reviewed the general design of the experiment as well as the interpreted outcomes. Prof. Karimi created the preliminary feasibility experiment. Prof. Vlasea, Dr. Habibnejad-korayem, Prof. Karimi, and Prof. Keshavarz revised and examined the article's content. I will be the first author on this work.

Chapter 5 of my thesis contains information for a co-authored article intended to be published in the future with Professors Mihaela Vlasea, Paria Karimi, Mohsen Keshavarz, and Dr. Mahdi Habibnejad-korayem. I contributed to the experimental plan, data processing, characterization design, post-processing of data, interpretation of results, in-depth discussion, and writing of the article. Prof. Vlasea

defined evaluation criteria and reviewed the experiment design. Prof. Karimi, Prof. Keshavarz, and Dr. Habibnejad-korayem reviewed and edited the content of the article. I will be the first author on this work.

Abstract

Additive manufacturing (AM), also known as 3D printing, is an innovative method for producing complex geometries with minimal material waste. Aerospace, medical, and battery fields are a few sectors that employ AM as a means to further create innovation in materials design, structural design and structural/mechanical property development. The aerospace industry is on of such sectors continuously seeking ways to reduce energy/fuel consumption by shifting towards lightweight and high-temperature resistant materials. Ti-48Al-2Cr-2Nb (γ-TiAl) is a popular choice due to its desirable weight-to-density ratio and superior high-temperature mechanical properties. However, traditional manufacturing methods for the Ti-48Al-2Cr-2Nb alloy are expensive. Additive manufacturing (AM), specifically electron beam melting (EBM), is a cost-effective alternative that offers the potential for optimal ductility and fracture toughness for γ-TiAl. To promote economic sustainability, this study explores varying particle size distribution (PSD) in the EBM process.

The research focuses on Ti-48Al-2Cr-2Nb alloy for PSD 45-150 µm, 38-150 µm, and 38-180 µm, specifically with the potential of PSD 38-180 µm as a more cost-effective reliable material to promote economic sustainability. By examining density and porosity morphology, as well as surface roughness, the study investigates how to maintain good density and surface qualities, irrespective of PSD, as the mechanical properties of the printed materials are dependent on the density, pore formation and surface quality obtained during the AM process. To mitigate pore defects and increase surface quality, process parameters involved in AM must be tuned to ensure the target density, porosity type and surface roughness of the final product. In this work, gamma titanium aluminide (Ti-48Al-2Cr-2Nb) was deployed in an electron beam melting (EBM) powder bed fusion process. The focus was to analyze and classify the printed part quality in terms of surface roughness (SA, STR, and SPC), relative density, lack of fusion defects and gas pore defects to establish trends across the parameter space.

This thesis follows various sets of experiments that detail process parameter combinations that aim to provide a wide range or part quality results, therefore gathering enough unique data to conduct a full analysis on the behavior of the EBM-printed parts. The experimental study involves data analysis and data visualization utilized to identify the relationship between the process inputs (parameters and engineered features such as normalized enthalpy and volumetric energy density), the resulting density and pore type (gas pores and lack of fusion pores) and the surface roughness parameters (spatial, feature, and height parameters).

The EBM process can face challenges in achieving low density levels and poor surface quality due to the applied energy and powder characteristics. More specifically, this thesis examines the relationship between PSD and porosity by identifying and investigating lack of fusion (LOF) and gas porosity types within threshold levels of 'Excellent,' 'Good,' 'Poor,' and 'Failed', with pre-defined ranges for the three classes. Additionally, the relationship between the PSD and surface roughness (SA, STR, and SPC) is also confirmed but utilizing a full factorial design of experiment (DOE) to create three sub-experimental hypothesis that explores the various prominent surface quality influencer (layer thickness and higher energy electron beam). Based on this experimental study, it was found that bulk density ranges spanned 88% - 99.99%, with gas porosity spanning 0.01% - 0.3%, and lack of fusion porosity spanning 0.001% - 12%. Additionally, for surface roughness, SA reports a range spanning (39.41 µm – 109.74 µm), STR reports (0.0984 – 0.8126), and SPC reports (2344.2 1/µm – 4084.31 1/µm) across the reference PSD 45-150 µm and the widest PSD in this study 38-180 µm. Based on resulting outcomes and literature, data distributions and statistical analysis were employed to classify and quantitatively defined the results obtained from the experimental study. The results demonstrate the relationship between the process parameters, density, and porosity type as well as the surface roughness. The study contributes to a comprehensive understanding of the interplay between PSD and porosity as crucial factors in the EBM AM process.

Acknowledgements

I have been incredibly fortunate to have received the support and guidance of so many amazing people throughout my Master's program. They have each played a critical role in helping me achieve my goals, and I am immensely grateful for their contributions. I cannot thank them enough for their unwavering support and encouragement, and for being a part of this incredible journey with me. I just wanted to take a moment to express my gratitude to the wonderful people who have supported me throughout my Master's program.

I am incredibly grateful to Dr. Mihaela Vlasea, my supervisor, for her unwavering support and invaluable guidance throughout my Master's program. Her mentorship not only enriched my academic and project work but also provided a source of encouragement during challenging times. Dr. Vlasea's leadership as a female figure in engineering research has ignited my passion for research and instilled in me the importance of perseverance. I am deeply thankful for her continued assistance and eagerly anticipate our future collaborations.

I also extend my heartfelt appreciation to Dr. Paria Karimi for her invaluable role as a co-mentor, offering insights into the electron beam melting (EBM) process and pushing me to enhance my research skills. Her encouragement has been pivotal in my journey towards completing this program with confidence.

I would like to give a special thanks to Dr. Mohsen Keshavarz and Dr. Esmaeil Sadeghi for their invaluable guidance and support throughout the project. Their expertise and suggestions significantly contributed to the methodologies and analyses conducted in this program.

I am grateful to Dr. Mahdi Habibnejad-korayem for the opportunity to collaborate with AP&C on my thesis project and for his insightful feedback on my research findings and industry presentations.

I would also like to appreciate the funding support received from the Federal Economic Development Agency for Southern Ontario (FedDev Ontario grant # 814654).

Furthermore, I express my sincere gratitude to my thesis examining committee members, Dr. Hamid Jahed Motlagh and Dr. Mustafa Yavuz, for their time and valuable feedback on my thesis.

And to my friends, mentors, and colleagues, thank you for your support and camaraderie. I'm truly grateful for the friends in MSAM who kept me motivated and shared countless laughs, and to those who offered encouragement and support along the way.

Lastly, I extend my deepest gratitude to my family—my parents, sister, and two brothers—for their unwavering support, late-night calls, and constant reassurance. Their love and encouragement have been my greatest source of strength and inspiration.

Dedication

I dedicate this thesis to my family, who have always believed in me. Especially to my parents – Biola and David Oluwajuyigbe, who have always emphasized the importance of education as a means of understanding the world we live in and choosing our own path in life. Thank you for everything you have done and sacrificed to help me get to this point. I pray you receive as much - and more - blessings than you have poured into me.

Table of Contents

Author's Declaration ii

Statement of Contribution iii

Abstract v

Acknowledgements vii

Dedication ix

List of Figures xiii

List of Tables xviii

Chapter 1 Introduction 1

1.1 Background 1

1.2 Electron beam melting 2

1.3 Effect of powder characteristics on EBM process 5

1.4 Effect of process parameter on density analysis 6

1.5 Effect of PSD and process parameter on density analysis 8

1.6 Effect of PSD and process parameter on surface roughness 9

1.7 Research objective 11

Chapter 2 Powder Characterization 13

2.1 Introduction 13

2.2 Materials and methods 13

2.2.1 Camsizer methodology 14

2.2.2 GranuDrum methodology 15

2.2.3 GranuPack methodology 15

2.2.4 Hall and carney methodology 16

2.2.5 Powder computed tomography methodology 16

2.3 Results and discussion 18
2.3.1 Powder morphology via SEM 18
2.3.2 Powder size distribution analysis 20
2.3.3 Powder rotating drum (GranuDrum) 29
2.3.4 Powder tap density (Granupack) 31
2.3.5 Hall/Carney powder flow 33
2.3.6 Powder computed tomography 34
Chapter 3 Density Analysis 51
3.1 Introduction 51
3.2 Materials and methods 51
3.2.1 Powder materials 51
3.2.2 Manufacturing process and parameters 51
3.2.3 Computed tomography and data visualization 54
3.2.4 Classification categories based on porosity (or alternately bulk density) levels 55
3.3 Results and Discussion 56
3.3.1 Powder characteristics 56
3.3.2 Experimentally-derived relationships between process parameters and bulk density 58
Chapter 4 Density Analysis for PSD Comparison 69
4.1 Introduction 69
4.2 Materials and methods 69
4.3 Results and discussion 70
4.3.1 Statistical analysis 80
4.3.2 Further analysis 90
Chapter 5 Surface Roughness Analysis 95

5.1 Introduction 95
5.2 Materials and methods 95
5.2.1 Sample characterization methodologies 97
5.3 Results and discussion 100
5.3.1 Powder characteristics 100
5.3.2 General observations 102
5.3.3 Statistical analysis 110
Chapter 6 Conclusion and Future Works 122
Letter of Copyright Permission 129
References 132
Appendix 142

List of Figures

Figure 1. Electron beam powder-bed fusion process. [17] 3
Figure 2. Different spot size/melt pool for multiple types of beams in welding. [13] 4
Figure 3. Schematic of Hall and Carney flow analysis. 16
Figure 4. Showcases a projection of the internal structure of the bulk particles collected from a CT scanner. a) Porosity in the powder bulk; b) Powder bulk. 17
Figure 5. SEM images of powder particles within the three-powder size distribution; a) 45-150 µm, b) 38-150 µm, and c) 38-180 µm. 19
Figure 6. Schematic of three key size parameters; xc_min the minimum chord diameter, x_area the equivalent circle diameter, and xFe_max the maximum Ferret diameter [53]. 21
Figure 7. xc_min from a particle projection. 22
Figure 8. xc_min particle distribution; a) standard distribution; b) cumulative distribution. 23
Figure 9. x_area particle distribution; a) standard distribution; b) cumulative distribution. 24
Figure 10. xFe_max particle projection. 25
Figure 11. xFe_max particle distribution; a) standard distribution; b) cumulative distribution. 26
Figure 12. sphericity vs particle size plots for all measured size parameters; a) xc_min; b) x_area; c) xFe_max. 28
Figure 13. Dynamic angle of repose for PSD 45-150 µm, 38-150 µm, and 38-180 µm. 30
Figure 14. Cohesive index for PSD 45-150 µm, 38-150 µm, and 38-180 µm. 31
Figure 15. Shows the average packing density measured from the GranuPack machine for the Ti-48Al-2Cr-2Nb powder. 32
Figure 16. Showcases distribution of Equivalent Diameter for All PSD measured; a) Histogram of Equivalent diameter for PSD 45-150 µm, 38-150 µm, and 38-180 µm; b) Violin plot showing distribution of Equivalent diameter for PSD 45-150 µm, 38-150 µm, and 38-180 µm. 35
Figure 17. Represents the violin plots derived for the Aspect ratio of all the analyzed powder set in this study: PSD 45-150 µm, 38-150 µm, and 38-180 µm. 36
Figure 18. Histogram of calculated equivalent diameter of PSD 45-150 µm powder with; a) portrays the total powder particle distribution and particles with porosity distribution; b) portrays total powder particle distribution and porosity distribution. 38
Figure 19. Histogram of measured aspect ratio of PSD 45-150 µm powder that portrays the total powder particle distribution and porosity distribution. 39

Figure 20. Figure showcases aspect ratio of PSD 45-150 µm powder with; a) portrays the total powder particle distribution aspect ratio against the volume; b) portrays total powder particle histogram distribution..... 40
Figure 21. Histogram of calculated equivalent diameter of PSD 38-150 µm powder with; a) portrays the total powder particle distribution and particles with porosity distribution; b) portrays total powder particle distribution and porosity distribution. 42
Figure 22. Histogram of measured aspect ratio of PSD 38-150 µm powder that portrays the total powder particle distribution and porosity distribution. 43
Figure 23. Figure showcases aspect ratio of PSD 38-150 µm powder with; a) portrays the total powder particle distribution aspect ratio against the volume; b) portrays total powder particle histogram distribution..... 45
Figure 24. Histogram of calculated equivalent diameter of PSD 38-180 µm powder with; a) portrays the total powder particle distribution and particles with porosity distribution; b) portrays total powder particle distribution and porosity distribution. 47
Figure 25. Histogram of measured aspect ratio of PSD 38-180 µm powder that portrays the total powder particle distribution and porosity distribution. 48
Figure 26. Figure showcases aspect ratio of PSD 38-180 µm powder with; a) portrays the total powder particle distribution aspect ratio against the volume; b) portrays total powder particle histogram distribution..... 50
Figure 27. Schematics of the printing strategy. a) The hatch melting strategy with a melt pool moving down the layer from side to side with a 90-degree rotation; b) The dimensions of an experimental sample which mirrors the dimensions of all the EBM printed samples in this study. 52
Figure 28. Scanning Electron Microscopy (SEM) representing the virgin powder state of Ti-48Al-2Cr-2Nb with a PSD of 45-150um; a) A 800x magnification image that showcases a large cluster of the powder feedstock; b) A 5000x magnification image showing the outer features of a singular powder samples within the feedstock cluster; c) a 4000x magnification image showcasing the internal structures of a singular powder sample within the feedstock cluster. 57
Figure 29. Isometric and orthographic minimum intensity projection view (top and side view) of the computed tomography images captured for varied density and porosity results in PSD 45-150um; (a) Very high density sample Run 2: sample 11 showcasing the gas and LOF pores ; (b) relatively

medium density sample Run 3: sample 10 showcasing the gas and LOF pores; (c) low density sample Run 5: sample 16 showcasing the gas and LOF pores. 59
Figure 30. Showcase the derived porosity level for each experimental run results for the EBM printed parts against the sample number: (a) represents the porosity level against the sample number in each threshold bins ; (b) represents the volume fraction for each pore type against the samples number in each threshold bin. 61
Figure 31. Showcase the different experimentally derived results for the EBM printed parts: a) represents the relationship between the volumetric energy density (VED) of every sample set and the relative density; b) represents the relationship between the volumetric energy density (VED)of every sample set and the gas porosity; c) represents the relationship between the volumetric energy density (VED) of every sample set and the Lack of Fusion porosity. 63
Figure 32. Showcase the different experimentally derived results for the EBM printed parts: a) represents the relationship between the normalized enthalpy of every sample set and the relative density; b) represents the relationship between the normalized enthalpy of every sample set and the gas porosity; c) represents the relationship between the normalized enthalpy of every sample set and the Lack of Fusion porosity. 64
Figure 33. showcase different violin plots for each threshold class containing the experimentally derived results for the EBM printed parts: (a) represents the distribution of porosity for each threshold bins; (b) represents the distribution of porosity for each defect type (specifically LOF and Gas pores) within each defined threshold bins. 66
Figure 34. showcase different violin plots for each threshold class containing the experimentally derived results for the EBM-printed parts: (a) represents the distribution of the LOF porosity in each threshold bins; (b) represents the distribution of the Gas porosity in each threshold bins. 67
Figure 35. Showcase the different experimentally derived results for the EBM printed parts of both PSD 45-150 µm and 38-180 µm: a) represents the relationship between the volumetric energy density (VED) of every sample set and the relative density; b) represents the relationship between the volumetric energy density (VED)of every sample set and the gas porosity; c) represents the relationship between the volumetric energy density (VED) of every sample set and the Lack of Fusion porosity. 73
Figure 36. Showcase the different experimentally derived results for the EBM printed parts of both PSD 45-150 µm and 38-180 µm: a) represents the relationship between the normalized enthalpy of

every sample set and the relative density / porosity; b) represents the relationship between the normalized enthalpy of every sample set and the gas porosity; c) represents the relationship between the normalized enthalpy of every sample set and the Lack of Fusion porosity. 74
Figure 37. Showcase different violin plots for each threshold class containing the experimentally derived results for the EBM printed parts which represents the distribution of overall porosity for each threshold bins for both PSD 45-150 µm and 38-180 µm. 75
Figure 38. Showcase different violin plots for each threshold class containing the experimentally derived results for the EBM-printed parts of each threshold bin for both PSD 45-150 µm and 38-180 µm: (a) represents the distribution of the LOF porosity in each threshold bins; (b) represents the distribution of the Gas porosity in each threshold bins. 78
Figure 39. Showcase different violin plots for each threshold class containing the experimentally derived results for the EBM-printed parts for both PSD 45-150 µm and 38-180 µm: (a) represents the distribution of the LOF porosity in each threshold bins; (b) represents the distribution of the Gas porosity in each threshold bins. 79
Figure 40. Pareto chart representing the relationship between the process parameters (focus offset, speed, current, and line offset) and the resulting EBM printed samples for the low regime analysis, where the significant standardized effect (4.30) or a significance level of 0.05 for both PSD 45-150 µm and 38-180 µm. a) The pareto chart for the relative density; b) The pareto chart representing the LOF porosity density; c) The pareto chart for the Gas porosity. 83
Figure 41. Pareto chart representing the relationship between the process parameters (focus offset, speed, current, and line offset) and the resulting EBM printed samples for the high regime analysis, where the significant standardized effect (4.30) or a significance level of 0.05 for both PSD 45-150 µm and 38-180 µm. a) The pareto chart for the relative density; b) The pareto chart representing the LOF porosity density; c) The pareto chart for the Gas porosity. 85
Figure 42. Pareto chart representing the relationship between the process parameters (focus offset, speed, current, and line offset) and the resulting EBM printed samples for the super-high regime analysis, where the significant standardized effect (4.30) or a significance level of 0.05 for both PSD 45-150 µm and 38-180 µm. a) The pareto chart for the relative density; b) The pareto chart representing the LOF porosity density; c) The pareto chart for the Gas porosity. 89
Figure 43. The main effect plots for the relative density in the low, high, and super-high regime for PSD 45-150 µm. 91

Figure 44. The main effect plots for the relative density in the low, high, and super-high regime for PSD 38-180 µm. 92
Figure 45. Image of the side surface for the Ti-48Al-2Cr-2Nb EBM-printed samples in this experiment. 96
Figure 46. Schematic of printed samples and the surface roughness scanning location. 98
Figure 47. Schematic images of the three surface roughness parameters and their derived calculation; a) SA; b) STR; c) SPC. [80] 100
Figure 48. Powder representative graphs for both PSD 45-150 µm and 38-180 µm; a) The PSD distribution and; b) the sphericity for the PSD distribution. 101
Figure 49. Violin plots showcasing the SA distribution for all the experimental analysis; a)The overal distribution; b) the distribution of SA results are overlayed to identify the change in values for the powder size distribution and the experimental runs. The blue dotted line indicates the best performing surface roughness for this material, as reported in the literature [82] and the black dotted line indicates the best surface roughness (SA) for Ti-48Al-2Cr-2Nb material in this experiment. 106
Figure 50. Violin plots showcasing the STR distribution for all the experimental analysis; a)The overall STR distribution; b) The distribution of STR results are overlayed to identify the change in values for the powder size distribution and the experimental runs. The dotted line indicates the the best surface roughness (STR) for Ti-48Al-2Cr-2Nb material in this experiment. 108
Figure 51. Violin plots showcasing the SPC distribution for all the experimental analysis; a)The overall SPC distribution; b) The distribution of SPC results overlayed to identify the change in values for the powder size distribution and the experimental runs. the black dotted line indicates the best surface roughness (SPC) for Ti-48Al-2Cr-2Nb material in this experiment. 110
Figure 52. The Pareto Chart derived for all the SA experimental analysis for both PSD 45-150 µm and 38-180 µm; a) Run 1 base experiment; b) Run 2 layer thickness experiment; c) slower and sharper beam experiment. 113
Figure 53. The Pareto Chart derived for all the STR experimental analysis for both PSD 45-150 µm and 38-180 µm; a) Run 1 base experiment; b) Run 2 layer thickness experiment; c) slower and sharper beam experiment. 116
Figure 54. The Pareto Chart derived for all the SPC experimental analysis for both PSD 45-150 µm and 38-180 µm; a) Run 1 base experiment; b) Run 2 layer thickness experiment; c) slower and sharper beam experiment. 118

List of Tables

Table 1. The test summary of the full powder characterization for the Ti-48Al-2Cr-2Nb with PSD 45-150 µm received from AP&C. 14
Table 2. Size Distribution percentile of xc_min, x_area, and xFe_max. 21
Table 3. Table of bulk density for PSD 45-150 µm , 38-150 µm , and 38-180 µm and the calculated Carr index and Hausner ratio powder flowability. 32
Table 4. Table of hall and carney flow rate results for PSD 45-150 µm, 38-150 µm, and 38-180 µm. 34
Table 5. Table of particle and porosity count identified in the quantified data. 34
Table 6. Ti-48Al-2Cr-2Nb thermal properties within the EBM process. [62,63] 53
Table 7. Threshold class developed for experimental study of Ti-48Al-2Cr-2Nb with PSD 45-150 µm. 56
Table 8. The powder morphology of the Ti-48Al-2Cr-2Nb used in the EBM process. 57
Table 9. Experimental design for the low, high, and super-high regime. 81
Table 10. The forecasted optimized density and LOF pore voxel count for the low regime, high regime, and super-high regime. 93
Table 11. The energy representation for the VED and NE for the forecasted optimized process parameter reported for each PSD and experimental regime. 94
Table 12. Identical experimental design for both PSD 45-150 µm and PSD 38-180 µm in this study. 97
Table 13. The specific powder size of the PSD 45-150 µm and 38-180 µm for D10, D50 and D90. 100
Table 14. Feasibility study to define the SA range for Ti-48Al-2Cr-2Nb printed in the EBM system. 103
Table 15. Showcases the process parameter that results in the best surface roughness (SA, STR, and SPC) for each experimental run hypothesis, with the corresponding best surface roughness and the reported worst surface roughness (SA, STR, and SPC). 104
Table 16. The resulting optimized Surface roughness for SA, STR, and SPC with the corresponding process parameter predicted 119
Table 17. The resulting optimized Surface roughness for SA, STR, and SPC with the corresponding process parameter predicted 121

Chapter 1
Introduction

1.1 Background

Gamma titanium aluminide (γ-TiAl) alloys are intermetallic compounds that have shown material properties comparable to nickel-based superalloys, including high-temperature oxidation and creep resistance, high-temperature strength, and modulus retention up to the brittle-ductile transformation temperature (700-800 °C)[1–3]; however, γ-TiAl alloys have a significant advantage over nickel-based alloys when considering their weight-to-strength ratio. The use of γ-TiAl alloys becomes advantageous when considering critical aircraft engine components, where high-performance turbines built with γ-TiAl alloys would be lighter, resulting in fuel savings [1,4]. One of the bottlenecks in adopting γ-TiAl for critical aerospace applications is that these materials are not easy to machine or forge, where the brittle nature of TiAl alloys at low temperatures makes them hard to manufacture into complex shapes [4,5]. Investment casting is used to conventionally produce γ-TiAl components, with notable challenges associated to the high reactivity of the alloy and limitations related to the resulting size and geometries that can be fabricated.

Ti-48Al-2Cr-2Nb, an alloy in the γ-TiAl class, tends to be difficult to manufacture into specific geometries owing to the formation of stress and dislocations during traditional manufacturing processes; induced failure within formed γ-TiAl is prevalent because of stress formation [6]. Additive manufacturing (AM) enables the fabrication of complex parts made of Ti-48Al-2Cr-2Nb with substantially decreased stress and improved resistance to failure [7] specifically when using the electron beam melting (EBM) – a technology under the AM processes often used to process Ti-48Al-2Cr-2Nb [8]. EBM operates by sequentially spreading thin layers of powder and selectively melting the powder at specific locations in each layer using an electron beam energy source to create a 3D part layer-by-layer based on a CAD (computer aided design) model [1]. EBM allows for the production of complex parts that cannot be achieved using conventional manufacturing processes such as machining, forming, and joining [1,2]. Moreover, EBM is an effective way to process Ti-48Al-2Cr-2Nb, as EBM can operate under elevated chamber temperature and vacuum [9]; such processing conditions are required for the Ti-48Al-2Cr-2Nb material due to its high melting point, high thermal conductivity, great structural stability (especially at high temperatures), low ductility and fracture toughness [10]. Furthermore, for Ti-48Al-2Cr-2Nb, employing a high-temperature powder bed-based AM technology like EBM diminishes the occurrence of internal stress or thermal stress-induced cracking compared to

conventional methods such as casting and milling. This reduction is attributed to enhanced diffusion processes within the materials. [6]. Furthermore, the vacuum environment in EBM facilitates a low oxidation process by eliminating gaseous molecules from the chamber atmosphere [9]. Therefore, EBM a is highly preferred method for processing of Ti-48Al-2Cr-2Nb [6,8].

1.2 Electron beam melting

Electron Beam Powder-Bed Fusion is a highly advanced manufacturing technique that utilizes an electron beam to melt a layer of metal powder, thereby creating a fused material [11]. The process involves a CAD/STL file of the desired object being developed and inputted into the EBM computer. Once the process starts, a layer of metal powder is spread on the build plate and is often determined by the layer thickness often ranging from 50 µm to 150 µm [12]. The powder utilized in this process often can determine the material properties of the EBM-printed parts. The overall recommended powder size ranges from 40-105 µm to maintain high flowability, density and electric conductivity[12–14]. One unique quality about the EBM process is the preheat strategy that is often employed to stabilize the powder-bed before melting[12]. Generally, the entire chamber temperature is increased to partially sinter the power layers before melting, which can often reduce mechanical property issues such as crack formation due to the loose powder or precipitate on the powder-bed [12]. Within the EBM process, an electron beam from a tungsten filament is directed towards the print line, which is controlled by magnetic coils that focus and deflect the beam. The beam has a specific spot size that melts the powder layer in alternating lines until the corresponding area of the CAD file is joined together [12]. The build plate is lowered, and the process is repeated with the next layer of powder spread over the previous one until the final object is produced[12,15]. The post-processing includes de-powdering, where the powder around and inside the object is removed, either through power air blast, depending on the fragility of the printed part [16]. This manufacturing technique has various benefits and downsides [7].

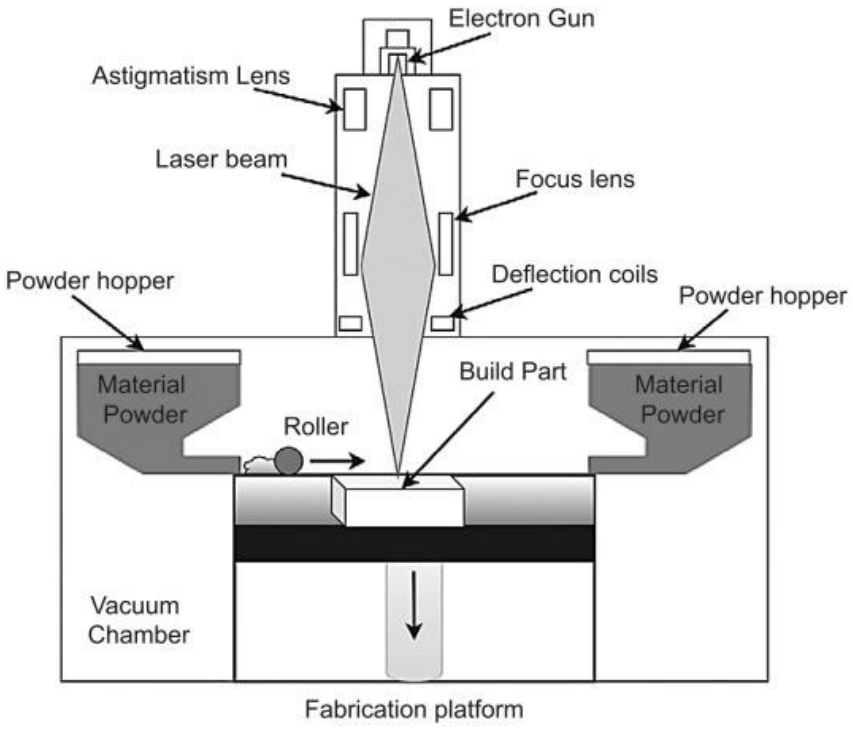


Figure 1. Electron beam powder-bed fusion process. [17]

Electron Beam Powder-Bed Fusion technology offers several advantages over traditional manufacturing processes [7]. One of the key benefits is the fast and efficient rate of the machine. Compared to traditional manufacturing, where it can take a lot of resources like time, cost and people to efficiently outsourcing and develop all the separate parts needed to create a final print, AM enables the production of more consolidated parts or sections of an entire build, and greatly reduces the amount of parts and resources needed to create a completed project build [5,18]. Moreover, the high-temperature working capability of EBM can achieve specific mechanical properties and microstructure granulation only achievable at a high-temperature application [16]. The entire print area is heated, and materials that support high-temperature usages such as TiAl or Nickel-based alloys are easily printed using this technology [19,20]. In other manufacturing processes, it can be challenging to work with these materials or fully melt the powder to provide a satisfactory joining.

Furthermore, electron beam melting utilizes a vacuum chamber to allow the electron beam to move in a straight line without causing deflections due to interaction with other particles in the air [4,7]. The EBM vacuum is often ranging from 10^{-3} to 10^{-6} mbar which is detonated as a medium vacuum level and allows for a low impurity level within metal EBM-printed materials such as Ti-48Al-2Cr-2Nb

because of the lack of H, N, or O in the atmosphere to interfere and bond with the alloys[1,4,13]. EBM is able to produce a high energy melting environment as the electron beam collides with the powder-bed surface [19]. This interaction often allows for roughly 80% energy transfer from the kinetic energy in the electron beam to heat energy absorbed on the powder surface [13]. Therefore, due to the high energy concentration of the electron beam, as seen in Figure 2, a deep and narrow melt pool can be formed. This melt pool formation provides an avenue for fine microstructures development within the materials utilized in EBM [12,16]. These structures produce generally very beneficial properties such as an enhance ductility and fracture toughness, due to the reduced area of the grainsize, which leads to an increase in dislocation density and the mentioned properties [7].

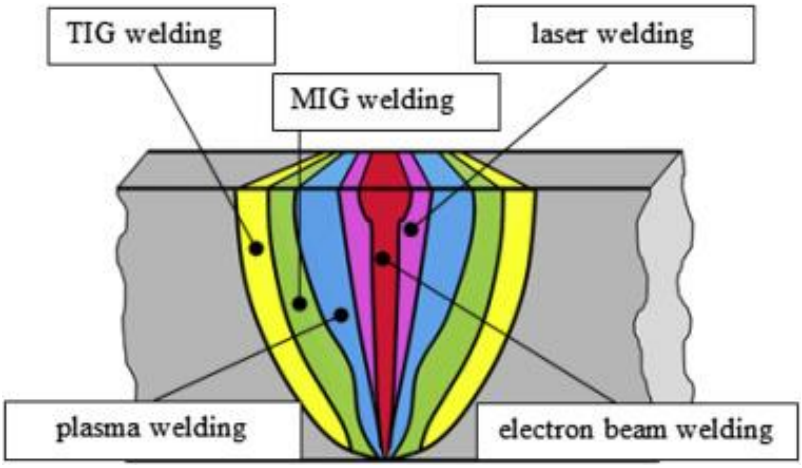


Figure 2. Different spot size/melt pool for multiple types of beams in welding. [13]

The EBM process, despite its numerous advantages, has some limitations [7]. One such disadvantage is the surface finish produced, which is not always considered a disadvantage in some cases, such as in biomechanical applications where a rougher surface allows for better tissue grip in osseointegration [21]. However, for parts that require tight tolerances, this can be seen as a disadvantage [22]. To combat this issue, post-processing of the material, such as grinding or sandblasting, is necessary, which adds to the overall cost and time required to produce a completed part [12].

Support structures are often needed during the EBM process depending on the geometry of the printed part to prevent the parts from bending, shifting, or warping [7]. While this is necessary to ensure the quality of the final product, support structure consume more powder, which can become a costly

endeavor due to the cost of AM metal powders [7]. AM is still a relatively new manufacturing process, and producing powder alloys is costly. However, researchers are working to produce less expensive parts by using gas or water atomized powder and also developing process parameter schemes where reusing powder has less impact on the quality of the resulting EBM-prints [4]. Despite these disadvantages, the EBM process is still seen as a highly efficient and cost-effective technology overall, especially for specific materials that have good high-thermal properties and are often difficult to manufacture traditionally [4,7,16].

1.3 Effect of powder characteristics on EBM process

Additive manufacturing (AM) technologies allow production of designed parts without the use of tooling. The AM technologies work on the principles of joining of materials to form a predesigned structure replicating a virtual 3D CAD model [1]. The AM sector has been on the rise the past few years, showcasing that AM can drastically reduce the processing steps needed to complete a product as well as demonstrating potential time/cost benefits [1]. As the interest in AM technologies increases, various studies are conducted to achieve an optimized print quality. Therefore, various explorations that look at the machine parameters, beam properties and powder/feedstock properties are conducted [6,23]. Regarding the powder properties, various powder features within AM are identified as influential on the results obtained after the AM process. The spreading performance, packing ability and powder consolidation are the main aspects within EBM that are influenced by the powder. The powder features can be classified into both the physical and chemical properties [24]. Flow resistance and packing density of powder affects how the powder material is spread with in the EBM technology as a result of the material type, surface conditions, and powder morphology. There are various methods used to quantify the powder properties within AM. Some of these measurements are powder size distribution (PSD), flowability, compressibility, and packing density [25].

Powder size distribution informs on the size and shape statistics of the powder [24,26]. Flowability refers to the ability of powder particles to move in bulk according to an applied force (gravitational, or external); there are various ways to measure flowability of metal powders within AM [27]. Compressibility is a measure of a powder's ability to evenly spread and settle using powder spreading techniques (rollers or re-coaters); this data gives more insight to the behavior of the AM material and can be fed to models that predict how much energy should be provided in each layer of powder during consolidation [25]. Similar to the compressibility, the packing density quantifies a powders' ability to

be packed together in bulk. The packing density looks at the bulk powder particles and mow much volume space the powder can occupy when pressure has been applied to the powder. The packing density provides insight to the estimated powder count in each layer during the melting process as well as the powder's ability to move when spread in the AM machine [28].

The different powder properties are interconnected. For example, a study by Popov V et al.[28] focused on Ti-6Al-4V powder that was inspected to identify and correlate changes in recycled powder properties on mechanical properties [28]. Based on the study, the PSD was shown to have an influence on the packing density and the flowability, where a larger PSD powder leads to a decreased packing density due to the volume that generally cannot be filled without having smaller powder particles. The flowability also performs worse for the wider PSD powders, which affected the mechanical properties [28]. Yim et al [14]. also studies the effect of powder morphology on the spreading behavior in the Ti-48Al-2Cr-2Nb powder using discrete element method (DEM) simulation in AM technologies [14]. Yim et al [14]. investigates the flowability of Ti-48Al-2Cr-2Nb powder based different morphologies generally found in the metal powders often utilized in AM such as: spherical particles, spherical + satellite particles, spherical + elongated particles, and spherical + satellite + elongated particles [14]. These different morphologies produce varied flowability and pore formation in the powder-bed, where powder particles with more elongated powder or satellite particles tend to produce issues in the particle alignment in the powder-bed creating larger or wider pore formation in the powder-bed [14]. Based on these studies, the powder behavior of the Ti-48Al-2Cr-2Nb material will differ depending on the morphology and PSD. Therefore, investigating the effect of the defined powder features of all the different Ti-48Al-2Cr-2Nb PSD's in this study will detail the expected effect of the powder behavior on the resulting quality (density and pore morphology, as well as surface roughness) of the EBM-printed parts.

1.4 Effect of process parameter on density analysis

The occurrence of pores is a common challenge in metallic parts fabricated by AM, affecting the mechanical properties of printed components [29]. In AM, an increase in porosity negatively impacts ultimate tensile strength (UTS), yield strength (YS), fatigue (F), and elongation (EL) [29,30]. For instance, Galarraga et al. [29] examined the effect of different porosity levels on the mechanical properties of EBM printed Ti-48Al-2Cr-2Nb samples. It was concluded that an increase in porosity level causes a detrimental change in the mechanical properties due to porosity locations acting as a

nucleation site for crack propagation [29]. Relative density and pore defect morphology are considered factors that affect mechanical properties, with process parameter selection playing a significant role in performance outcomes [29]. Various other studies report on the effect of process parameters on porosity outcomes. For instance, Baudana et al.[31] and Gaytan S. M.[32] et al. studied the impact of process parameters, specifically current, speed, and layer thickness, on the characteristics of the resulting Ti-48Al-2Cr-2Nb and Ti-6Al-4V EBM-printed samples for respectively [31–33]. Based on these studies, the relative density ranges from 92%-99% with dependence on the process parameter combination, where a lower applied energy results in a lower relative density.

Although porosity defects are known to affect mechanical properties, there are available methods to reduce or diminish porosities in metal objects. One method is the hot isostatic pressure (HIP) process. HIP is considered one of the most efficient ways of reducing porous defects in metal samples and influencing microstructure to tailor mechanical properties by using a high temperature and pressure environment [34]. To investigate the extent of pore closure, Tammas-Williams S et al. [35] investigated the porosity changes in Ti-6Al-4V EBM-printed samples with porosities ranging from 0% - 2.02% and observed a 100% pore removal after HIP; however, samples with porosity levels higher than 2% resulted in pore reduction of 60-80% after HIP [35]. Identifying acceptable target density (or porosity) levels is important when optimizing process parameters in EBM. Overall, the research suggests that density is identified as a critical factor influencing the parameter design of the EBM process [31–35], as it known that mechanical properties are influenced by the types of defects formed in the material [36].

Pore analysis is important to quantitatively represent the porosity and density information of printed samples. Some of the features that are collected to inform pore analysis are pore morphology such as the surface area, volume, aspect ratio, X-Y-Z coordinates, and spatial distribution [29,37]. Data from X-ray Computed Tomography (CT) can be processed to reveal spatially-resolved voids such as pore defects and internal cavities within the volume of the parts, based on resolution constraints of the detector, reconstruction and segmentation algorithms [37]. Pore analytics from CT can resolve aspects such as the pore morphology, aspect ratio, orientation, size, and spatial distribution of the pores [37]. Therefore, looking at studies that integrate CT measurements to report porosity levels in AM can provide more insight to the current pore analysis methodologies. Most studies that focus on density or porosity in EBM-printed parts, prioritize the overall porosity value, with a less in-depth analysis of the classes of pores present. The few studies that analyze the varied porosity type, such as Cunningham et

al. [36] and Tammas-Williams et al. [38], connects the relationship between the input energy and powder feedstock contamination with the characteristics of the developed pores in the EBM prints [36,38]. It is crucial to validate these findings and determine the effect of each specified process parameter and the overall influence of the applied energy on the density and porosity. The expansive printing process combinations will provide a medium to fully investigate the density and pore defect results.

1.5 Effect of PSD and process parameter on density analysis

Mechanical properties are intricately tied to various quality outcomes that result in the electron beam melting (EBM) process such as microstructure, surface roughness, relative density, porosity, and pore defect morphology [29]. The formation of defects is often attributed to the applied energy from the electron beam when melting the metal powders and the powder morphology at the time of printing [29]. These main reasons are reported to largely influence the formation of porosity within the EBM-printed samples. Quantitative analysis of the influence of process parameters in conjunction with powder properties on the porosity development needs to be confirmed. Notably, the two main types of defects, lack of fusion (LOF) defects and gas pore type defects, as defined by the pore morphology, are directly attributed to insufficient energy applied during the layer melting and material vaporization process, as well as the inclusion of porosities arising from internal pores within the powder respectively [31–33,35].

The influence of powder size distribution (PSD) on the EBM-printed results has been scarcely fully investigated through experimental methods, especially when establishing the relationship between pore defect type and the PSD. There have been various studies researching into the influence of powder characteristics such as flowability and packing density of the feedstock during EBM-printing process, especially through simulation modelling [39,40]. Recent studies investigate different PSD distribution and how the PSD influence the various powder characteristics. Zhao et al [40]. investigated the influence of powder characteristics (size morphology, flowability, and packing density) and the EBM process features (preheat temperature scheme, melting parameters). The findings showed that as the thickness of the powder layer increased, the packing density of the powder also increased [40]; however, mixing powder blends with large and small mean sizes may increase the packing density to some extent, but it could have a negative impact on the flowability. The study by Habibnejad-Korayem et al. [39] aimed to establish the relationship between the PSD and flowability. The findings indicate

that having a larger mean size and a narrower size distribution can reduce inter-particle friction, which has a positive impact on the properties of powder bulk and rheology [39]. Additionally, Habibnejad-Korayem et al. [39] discovered the dynamic flowing behavior of the powder, such as the dynamic cohesion index and dynamic angle of repose, is only linked to the powder's mean size and not to PSD. There have not been many investigations into connecting the influence of varying PSD directly on the resulting defects in EBM. As additive manufacturing (AM) advances, these detailed insights on the technology and material features that affect the resulting density become integral to tailoring and optimizing EBM processes for advanced materials like Ti-48Al-2Cr-2Nb. The ongoing pursuit of a comprehensive understanding of these intricate relationships will undoubtedly drive advancements in both the theory and practical application of additive manufacturing techniques, particularly in the production of high-performance components. More notably, these studies are important, as different powder size distributions may be more economical to produce, thus driving the economic sustainability of the EBM process.

1.6 Effect of PSD and process parameter on surface roughness

Surface roughness is a measure used to describe the surface features of a material. In AM, the surface quality is an important feature that influences performance and reliability of printed parts [22]. The different AM technologies produce various ranges of roughness values depending on the type of AM process [15]. For the EBM process, the surface quality tends to be rougher as a result of the physics behind the interaction between the material and the energy source used to melt the material system. Specifically, EBM is a unique AM class of technologies that utilizes an electron beam as means to fuse powder particles together, layer-by-layer, whereby the high precision electron beam creates a adjacent melt tracks within the core of the part and a solid perimeter around the part that is surrounded by adjacent powders. As a result, due to cycling heating phenomena and material sequential layering, the resulting surface exhibits asperities related to fused powders, layering and over-melting [22].

There are instances where a relatively high surface roughness can be considered as being beneficial, or conversely, it can be considered as a drawback. Firstly, in orthopaedic applications, a higher surface roughness is generally preferred. Deligianni et al.[41] and Ponader et al.[42] propose that a high surface roughness can be advantageous to enhance osseointegration. As such, implants require a very specific surface quality whereby a divot on the surface of the material inserted provides an avenue for better attachment and proliferation of cells [21,41]. Additionally, in various other fields in engineering, there

are instances where a rough surface texture can create a specific response when studying fluid flow. For example, in fluid systems such as heat exchangers, a rough surface can drastically reduce fluid flow rate and increase heat transfer; and many studies such as Kaur et al. [43] are investigating the implementation of a porous and textured surface to increase performance of such systems [43,44].

However, there are instances where a smaller surface roughness is preferred [31]. For examples, in the aerospace sector a poor surface quality is not ideal when aiming to achieve the best mechanical properties available for a specified material[15,45]. A poor surface quality can potentially introduce cracks at the surface and lower fatigue life due to the formation of stresses along the surface at critical points created by the surface peaks[15,45]. Nicoletto et al. [46] and Chern et al. [45] found that the fatigue limit is directly correlated to the surface roughness. Studies deployed on various Ti-6Al-4V EBM printed samples with different surface roughness values were compared and the fatigue limit was found to change depending on the surface [45,46], where a smaller surface roughness tends to produce a higher fatigue limit. Therefore, surface roughness is said to influence the fatigue limit to a large extent and a better-quality surface is preferred in instanced where fatigue limit is observed [47]. Another instance where a lower surface roughness is preferred are parts that require good surface finishing for aesthetic, functional, or assembly fit purposes; this consideration is even more pressing for complex-shape components. At a lower surface roughness, the post-processing time and cost is reduced significantly. Overall, achieving a good surface roughness can be a driving requirement in EBM, depending on the design complexity and post-processing cost constraints.

The surface roughness outcomes are dependent on the powder and printing conditions of the build in EBM [48], specifically the powder features (morphology, PSD [D10, D50, D90], material properties (heat capacity, specific heat, absorptivity)), process parameters (layer thickness, focus offset, current, speed, number of contours, and line offset) and applied energy to the melting process [48,49]. The preheat process parameters (accelerating voltage, preheat temperature) and digital CAD design (step-stairwell effect, tessellation) are also features of the EBM machine that affects the melting and solidification process of the targeted metal. Various studies have defined different EBM parameters as the most influential on the surface roughness. For example, Carolo et al. [44] summarized that layer thickness and powder size distribution are some of the predominant parameters influencing surface roughness in the EBM process; however, additional experiments are needed to statistically confirm this theory [44]. The side surface or lateral surface quality of EBM printed materials is also dependent on applied energy. According to Carolo et al. [44], increasing the energy density increases the thermal

accumulation in the part, which creates a scenario where the high-temperature gradient captures powder particles just outside of the melt pool, thus generating partially melted particles at the part borders [44,48]. These particles affect the surface quality. It was found that having a sharper and slower electron beam is expected to result in a higher surface roughness[44].

Generally, studies utilize RA as a measure for the surface roughness value for experimental measurements. However, Rosemtritt et al. states that this method presents issues with misleading results, where the high and low peaks in the samples are not always accurately represented due to a very small sample size measurement and the 2D quality of the measurements [50]. RA measures a singular line on the desired surface, therefore, the surface roughness can be massively understated for surfaces with complex spatially-distributed features [50,51]. Hence, arithmetic mean height (SA) measurements are utilized instead to describe a surface area captured in the measurement zone of interest [50]. SA, similar to RA, measures the average absolute value of the surface peaks (the difference in height of each point compared to the arithmetical mean of the surface); however, the SA confirms the values over a 3D surface of the sample instead of the RA, where 2D topology projection of a line on the sample surface is measured [50]. For this study, the SA value will be used to better represent the experimental surface. Additionally, Texture Aspect Ratio (STR) and Arithmetic mean peak curvature (SPC) are other surface roughness features of interest that provide further insights into the size distribution and spatial arrangement of the peaks in the EBM-printed parts. The SA, STR, and SPC features can provide a better means to analyze the surface roughness formation in the EBM process and draw meaningful conclusions on the effect of process parameters on surface quality outcomes.

1.7 Research objective

Overall, there are various aspects of the EBM process hypothesized as influential in the mechanical properties of the final Ti-48Al-2Cr-2Nb printed material. The aspects such as process parameters and powder feedstock characteristics have been researched to identify some of the dominant impact of each EBM parameters and their effect on the EBM-printed parts. This study elucidates the qualitative and quantitative relationship between the various levels of the PSD in conjunction with EBM process parameters on the resulting density, porosity type, and surface roughness. Additionally, the EBM process parameter combination themes (high energy combination, low energy combination) are investigated to understand the trend and threshold of the density, porosity type, and surface roughness formations for each PSD type. Overall, the resulting behavior of Ti-48Al-2Cr-2Nb material in EBM is

confirmed in this study, providing an avenue to develop future machine learning (ML) models or analysis that can accurately and repeatably predict the EBM-printed outcomes. The research goals or objective for this thesis can be defined into four main objectives, with pertinent studies captured in respective chapters.

Objective 1: Investigating the powder features of three different PSD ranges for Ti-48Al-2Cr-2Nb powder particles. The methodologies, results, discussion, and conclusions are captured in Chapter 2

Objective 2: Investigating the comprehensive pore defect analysis for EBM-printed Ti-48Al-2Cr-2Nb. The methodologies, results, discussion, and conclusions are captured in Chapter 3.

Objective 3: Investigating and comparison analysis of pore defect for different PSD EBM-printed Ti-48Al-2Cr-2Nb. The methodologies, results, discussion, and conclusions are captured in Chapter 4.

Objective 4: Investigating and comparison analysis of surface roughness for different PSD EBM-printed Ti-48Al-2Cr-2Nb. The methodologies, results, discussion, and conclusions are captured in Chapter 5.

Chapter 2
Powder Characterization

2.1 Introduction

Prior powder feature research in available literature predominantly centers on the trends in the behavior of powder before melting in the EBM and LPBF technologies. There are a few papers that examine the effect of powder feature on the resulting powder-bed spread before melting using simulation and various ML models. This study however investigates the different PSD Ti-48Al-2Cr-2Nb powder features such as the morphology, flowability, density, and cohesivity. In addition to the behavior of the powder, the entire 3D internal structure of the various Ti-48Al-2Cr-2Nb powder is confirmed, specifically the powder porosity. These different features of the powder are confirmed to identify the effects on the experimental EBM-printed samples in this study.

2.2 Materials and methods

In order to thoroughly examine how the size distribution of powder affects the density properties of Ti-48Al-2Cr-2Nb (AP&C – A GE additive company, Montreal, Quebec) printed by electron beam melting (EBM) powder bed fusion process, various methods of characterization were utilized to gather relevant data for this research. This chapter concentrates on the impact of different Particle Size Distribution (PSD) on the properties of powder. The primary objective is to investigate the relationship between powder properties and PSD with the help of characterization techniques. A full powder characterization was conducted on the virgin powder received from AP&C using a Camsizer X2 (Retsch, Haan, Germany), FT4 Powder Rheometer (Freeman Technology, Gloucestershire, UK), Hall/Carney Flowmeter Funnel (HMK-Test, Dandong Liaoning, China), GranuDrum (GranuTools, Wallonia, Belgium), and GranuPack (GranuTools, Wallonia, Belgium). The various characterization equipment provides in-depth quantitative data on the particle size distribution, standard flowability, compressibility, Hall flow, flowability, and packing density for the three PSD observed, 45-150 µm, 38-150 µm, and 38-180 µm.

The Camsizer X2 machine is an image-based particle size analyzer with a X-Dry with X-Jet dispersion model. This machine was utilized to determine actual powder size distribution of the Ti-48Al-2Cr-2Nb powder received from AP&C. The FT4 Powder Rheometer was used to determine the standard flowability and compressibility of the 45-150 µm powder. The Hall/Carney Flowmeter Funnel tested

the hall flowability of the powder (under the Hall metrics). The GranuDrum also measures the flowability of the powder, but under no additional pressure, only gravitational force (flowability of powder at a free surface). The GranuPack analysed the packing density at varied levels of tapping. All experiments were performed in triplicate, for each powder type respectively. In this study, the powder was visualized under a scanning electron microscopy (SEM) imaging machine (TESCAN VEGA 3, TESCAN, Brno, Czech Republic).

Table 1. The test summary of the full powder characterization for the Ti-48Al-2Cr-2Nb with PSD 45-150 µm received from AP&C.

Instrument	Purpose	Repetitions
Camsizer X2	Particle size distribution	3 (3 for each powder)
FT4 Powder Rheometer	Standard flowability	3 (3 for each powder)
FT4 Powder Rheometer	Compressibility	3 (3 for each powder)
Hall/Carney Flowmeter Funnel	Hall flow	3 (3 for each powder)
GranuDrum	Flowability	3 (3 for each powder)
GranuPack	Packing density	3 (3 for each powder)

The various instruments have specific methodologies designed to obtain the powder characterization data. Based on Table 1, the various methodologies for the data collection is as described below:

2.2.1 Camsizer methodology

The size and shape statistics are measured under the Camsizer X2 powder analyzer. This machine is versatile and can measure various powder, granules and particle morphology using dynamic image analysis. The Camsizer X2 can measure particles between 0.8 µm and 8 mm diameters. Therefore, this machine is an appropriate tool to employ to accurately decipher the various powder features. For example, xc_min [µm], xFe_max [µm], and x_area [µm] are specific diameter distributions that form the shape characteristics of the powder particles. To obtain the diameter distribution in the Camsizer X2, images of the powder particles poured into the system using a dual camera are captured. Three different distribution percentiles are highlighted in the post processing of the images, which are the 10%, 50%, and 90% of the various diameter size distribution. To further identify the distribution of the diameter, the cumulative percentages of the volume proportion of particles smaller than a particular size and the non-cumulative proportion of the powder particles or histogram distribution are derived from the images captured in the dual camera.

2.2.2 GranuDrum methodology

GranuDrum is a machine designed to measure powder flowability in powder particles. The Rheological properties are identified using the rotating drum principle implemented in the GranuDrum system. In order to guarantee uniformity in powder behavior and operational handling, at least three replicates of each powder were tested. The powder was homogenized by transferring it to a metal can and rolling it, then 50mL of powder was measured and placed in a special drum with transparent end windows. The GranuDrum device rotated the drum at 17 predetermined angular velocities, ranging from 2 to 20 rpm in increments of 2 rpm, followed by 25 to 60 rpm in increments of 5 rpm. We used a different velocity sequence for each replicate to minimize internal sequence effects and took replicate measurements on unused powder until the supply was exhausted. The powder was re-homogenized before continuing testing to ensure representative sampling and minimize time series effects across replicates.

The dynamic angle of repose is the angle at which the surface of a powder settles. Good flowability corresponds to a low dynamic angle of repose. The cohesive index is a measure of the fluctuation of the interface of a powder compared to its average surface position. The cohesive index of a powder is related to the cohesive forces between the particles. A lower cohesive index indicates a powder that is less cohesive. When a powder is cohesive, its flow is intermittent, while a non-cohesive powder flows smoothly. According to the flow guidelines specified in the instrument software, cohesive index values less than 5 are considered very good, values ranging between 5-10 are considered good, values between 10-20 are considered fair, values between 20-30 are considered passable, values between 30-40 are considered poor, and values greater than 40 are considered very poor.

2.2.3 GranuPack methodology

For each trial in the GranuPack, three powder samples were measured from each powder type with a volume of 35mL and recorded their respective masses and ambient temperature. Firstly, the machine lowered the initialization tube into the vessel and poured in the powder. Once the powder was poured into the GranuPack, the initialization tube is lifted out of the vessel and a small weight, known as a diabolo, is placed on top of the powder bed to keep it level and weighed down. By lifting the initialization tube out of the vessel, the powder that has piled up towards the edge of the vessel can be redistributed back towards the middle to maintain a relatively consistent powder bed before the diabolo is inserted.

2.2.4 Hall and carney methodology

The Hall and Carney experiment involved taking three measurements using a fresh quantity of powder. Care was taken to pour the powder carefully into the center of the flowmeter funnel while blocking the discharge orifice with a gloved finger. No tapping, vibration, or movement of the funnel was allowed. A weighing dish was placed under the funnel orifice to collect the powder. The operator then removed their finger from the orifice and started the timing device simultaneously to allow the powder to flow through the funnel. If the powder did not start flowing, a light tap on the rim of the funnel was permitted to initiate the flow. The timing device was stopped and the time was recorded to the nearest 0.1 s as soon as the last of the powder left the orifice. The Static Flow Method, was employed for all three PSD powders. The process was identical for both the Hall and Carney experiment methods except for the quantity of powder used, which was 50.0g and 150.0g respectively. Figure 3 showcase a sample schematic of the hall and carney flow analysis with the corresponding angle and funnel dimensions.

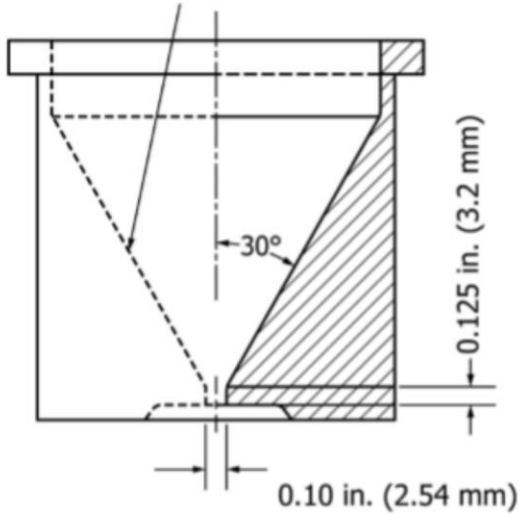


Figure 3. Schematic of Hall and Carney flow analysis.

2.2.5 Powder computed tomography methodology

This analysis is done to confirm the properties of the feed stock by utilizing CT (Zeiss Xradia 520 Versa, ZEISS, Oberkochen, Germany) data. This analysis complies the 3D structure of a select few bulk particles for each of the PSD's 45-150 µm. 38-150 µm, and 38-180 µm in order to confirm the shape and porosity within the powder distribution. In order to achieve accurate results, the powder particles scanned are re-used powder samples to maintain a similar powder structure that is used during

the experimental EBM-printing for the CT analysis. This analysis was conducted using the CT to reconstruct both the external and internal structure of a samples set of the powder feedstock. Each powder sample size was mixed together with hot glue to maintain the integrity and location of the powder during scanning with a 5 µm resolution. Using 3D imaging of each EBM-printed part, an image processing program (Dragonfly Software, Object Research Systems (ORS), Montreal, Canada) was used as a post-processing analysis tool to measure the pore properties. Based on the form, size, and aspect ratio of each powder and pore, various information on the powder morphology was obtained and identified. To ensure a reduced data noise in the collected scan, a filter was defined to remove any artefacts less than 10 µm in volume size. The resulting qualitative data derived from the scan shows the powder distribution as well as the porosity distribution in a set location of the scan. Figure 4 presents the projection of the porosity and powder distribution in the samples scan.

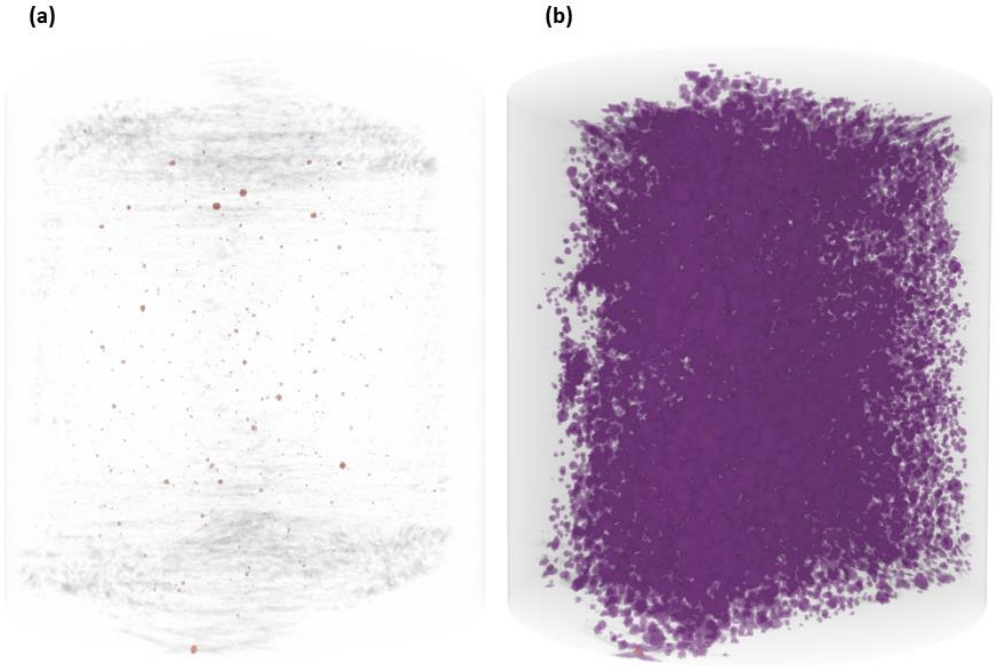


Figure 4. Showcases a projection of the internal structure of the bulk particles collected from a CT scanner. a) Porosity in the powder bulk; b) Powder bulk.

Using Dragonfly software (Dragonfly Software, Object Research Systems (ORS), Montreal, Canada), information of the powder morphology is derived as quantitative data. This information is processed to extract correlations between the PSD and the powder properties.

2.3 Results and discussion

The results of the powder characterization are compiled to identify specific features of the different specified PSD Ti-48Al-2Cr-2Nb feedstocks. This investigation provides insight on the powder features that have been hypothesized to influence the resulting EBM-printed part.

2.3.1 Powder morphology via SEM

The feedstock utilized during the analysis of this study is the Ti-48Al-2Cr-2Nb powder particles (AP&C – A GE additive company). There were three size distributions obtained of this powder material, specifically PSD 45-150 µm, PSD 38-150 µm, and PSD 38-180 µm. PSD 45-150 µm is the "typical" powder that is often used during manufacturing and is the optimized distribution that is observed to provide consistent results in EBM-AM. The other powder distributions are experimental powders that can give insight to how the powder morphology and properties can the powder bed in the EBM technology as well as the powder consolidation during the melting process.

One of the first analysis that can be observed is the physical components of the powder. SEM is able to visually capture various physical features of the feedstock. For example, satellite particles, porosity, and overall shape. Figure 5 shows several images collected from the SEM machine of all three PSDs in the virgin state (as-received) in this study.

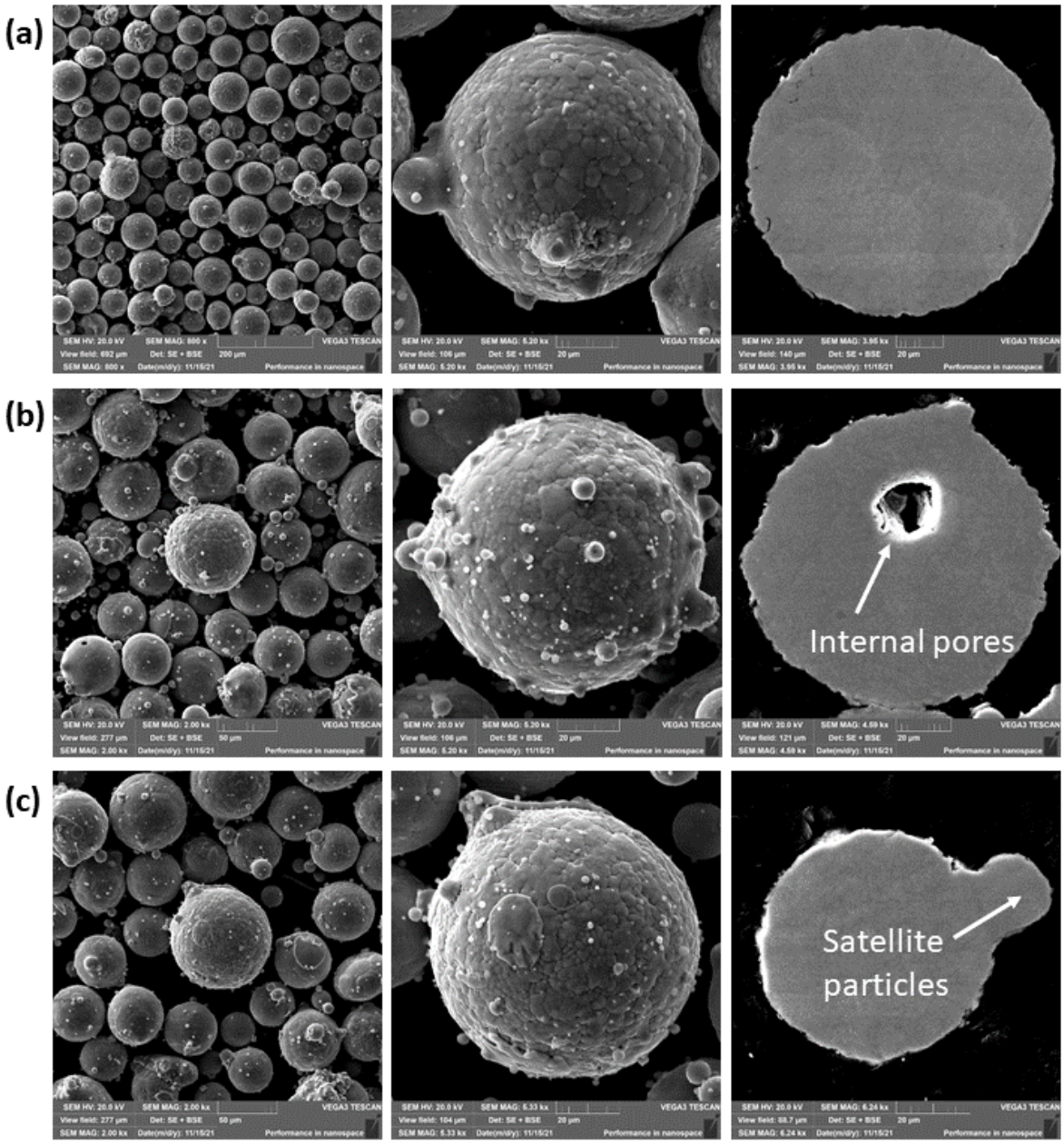


Figure 5. SEM images of powder particles within the three-powder size distribution; a) 45-150 µm, b) 38-150 µm, and c) 38-180 µm.

As seen in Figure 5, satellite particles are present within the bulk powder. There is a difference in concentration of these particles depending on the PSD. PSD 38-180 µm and PSD 38-150 µm appears to have a higher dominance of satellite particles within the powder particles. This is a result of the lower powder size (38 µm) being present as compared to the PSD 45-150 µm (45 µm). In addition, during production of the feedstock powder, nano and micro particle are often not accurately removed and are often joined to large particles creating the inclusion of satellite particles in the feedstock. During the powder manufacturing process, the smaller powder size potentially allows more of these micro particles to agglomerate to the surface of the powder. Additionally, a wider PSD range can lead to more micro particles presence, whereas a smaller PSD range allows for more control on what particles can be presented in the bulk feedstock.

Additionally, another visible feature of the powder particles captured by the SEM machine by viewing powder cross-sections is the powder porosity. This type of defect is usually common and can form as a result of the powder manufacturing process. The porosity in the powder is usually spherical shaped from the presence of Argon. Argon is introduced into the powder during production of the feedstock during plasma atomization. Pressure from the Argon is built on the surface of the pore creating a more spherical shape.

These features can affect the resulting print in EBM to varying degrees. The porosity from the powder can be transferred during consolidation and solidification during the EBM process. Additionally, the satellite parts can affect the spreadablilty of the powder, which can result in inconsistencies in the powder layer after being spread on the build plate [52]. For instance, the layer thickness can vary at different locations on the powder-bed, which can affect the fusing/consolidation of the powder during melting creating lack of fusion porosities.

2.3.2 Powder size distribution analysis

The PSD reported by AP&C for the feedstock is overall PSD 45-150 µm, PSD 38-150 µm, PSD 38-180 µm. However, for a detailed analysis, further information on the powder morphology needs to be obtained; for example, the diameter, longest ferret diameter, and width of the overall cumulative powder particle distribution. Therefore, the Camsizer X2 Image Based Particle Size Analyzer was used to capture more information on the powder particles.

The Camsizer analysis provides information on the xc_min [µm] (width of the particle associated to the sieving). xFe_max [µm] (the longest ferret diameter of the particles), and x_area [µm] (the diameter

of the particles when projected in an equivalent spherical volume) of the Ti-48Al-2Cr-2Nb powder as seen in Figure 6.

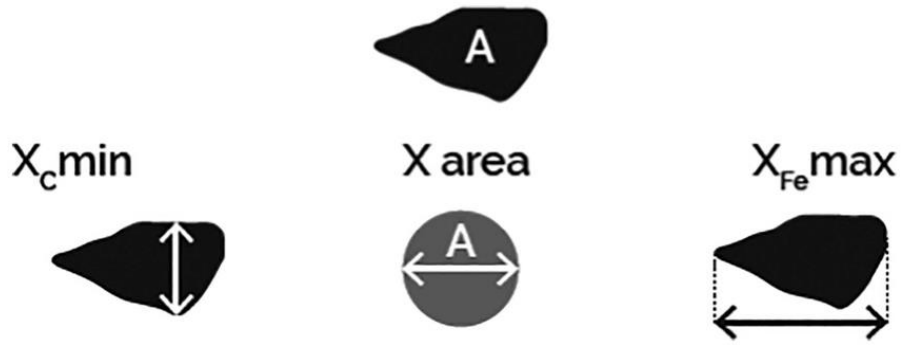


Figure 6. Schematic of three key size parameters; xc_min the minimum chord diameter, x_area the equivalent circle diameter, and xFe_max the maximum Ferret diameter [53].

Based on the Camsizer analysis, the defined D10, D50, and D90 for all the key size parameters are determined along with the standard deviation. These size distribution percentile values are reported in Table 2 below. These percentiles are essential in describing the behavior of powders in the EBM system. For example, there is a correlation between the reported size distribution and the surface roughness result. Additionally, this study will be investigating the effect of PSD on the resulting EBM printed part, therefore the D10, D50 and D90 are important features of the powder that provides more detail to the investigation of PSD effects in EBM.

Table 2. Size Distribution percentile of xc_min, x_area, and xFe_max.

Particle Feature	PSD	D10	D50	D90
Xc_min	**45-150 µm**	55.15±0.19	78.77±0.48	127.58±0.46
	38-150 µm	43.20±0.22	69.49±0.71	126.99±0.68
	38-180 µm	44.82±0.28	77.46±1.16	155.72±0.92
X_area	**45-150 µm**	56.94±0.09	80.12±0.47	131.14±0.42
	38-150 µm	44.83±0.20	72.91±0.76	132.18±0.77
	38-180 µm	46.34±0.18	81.17±0.83	161.68±0.77
xFe_max	**45-150 µm**	58.91±0.06	85.21±0.57	139.21±0.43
	38-150 µm	47.31±0.36	78.90±1.40	141.18±0.76
	38-180 µm	48.86±0.30	87.72±0.40	173.61±0.84

Xc_min

Xc_min is the measure of the particle breath, which is closely related to the observed sieve analysis. Figure 7 shows the xc_min measurement taken from an arbitrary particle.

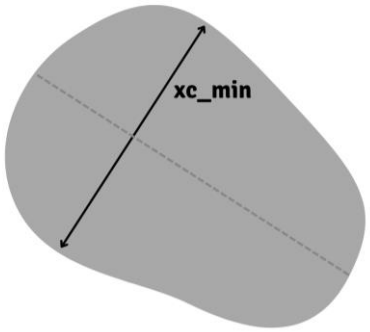


Figure 7. xc_min from a particle projection.

The accumulated xc_min distribution for PSD 45-150 µm, 38-150 µm, and 38-180 µm is derived based on the measurements collected from the Camsizer. The graph Figure 8 below shows both the cumulative and general distribution of particle present is a sample set for all three PSDs. It can be seen that the xc_min measurements are biased towards the smaller powder size distribution range for all powders, with a non-Gaussian distribution.

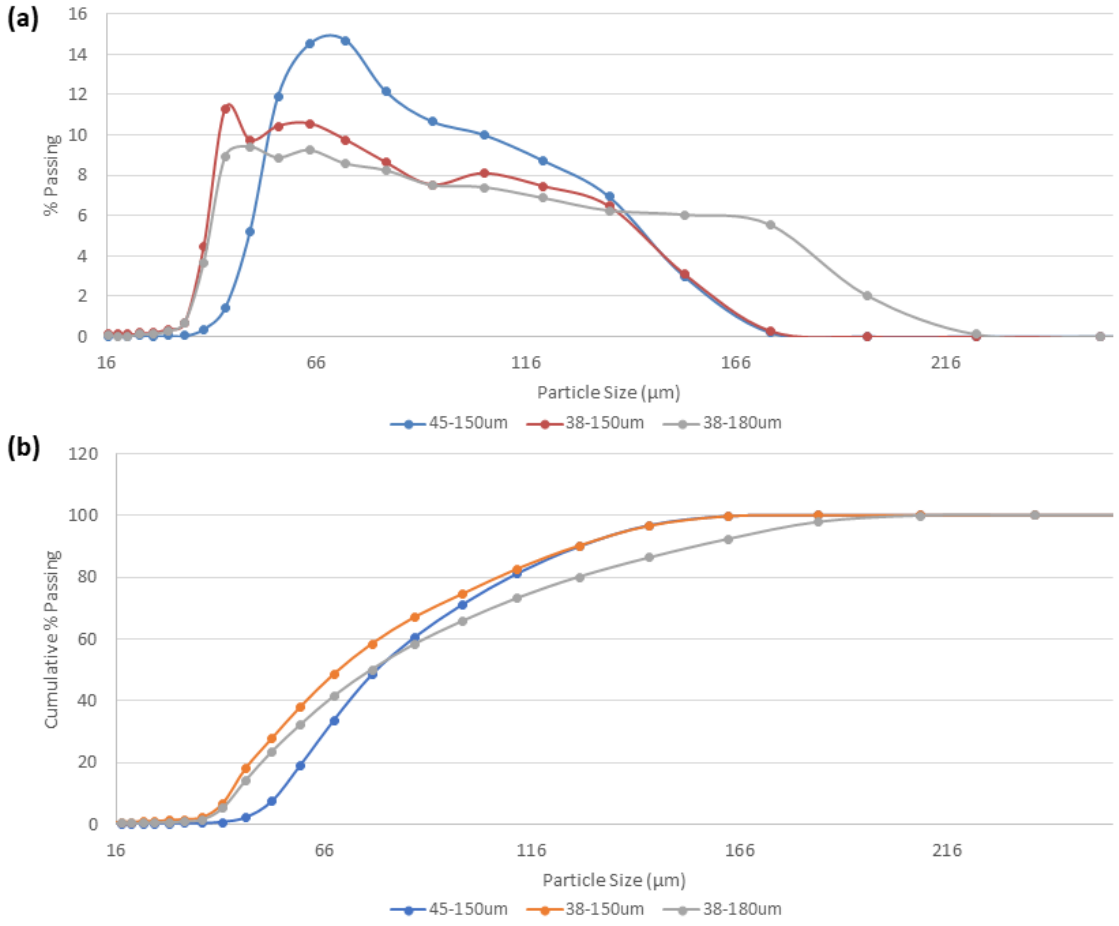


Figure 8. xc_min particle distribution; a) standard distribution; b) cumulative distribution.

X_area

X_area is the diameter of the particle projected based on the equivalent spherical volume of the measured powder particle. Figure 9 shows the distribution of the powder particles based on the x_area. The cumulative and the non-cumulative distribution is represented in Figure 9.

The accumulated x_area distribution for PSD 45-150 µm, 38-150 µm, and 38-180 µm is derived based on the measurements collected from the Camsizer. The graph below shows both the cumulative and general distribution of particle present is a sample set for all three PSDs. Similar to the xc_min, the x_area graphs in Figure 9 are indicative of a non-Gaussian distribution, with a bias towards the smaller PSD range.

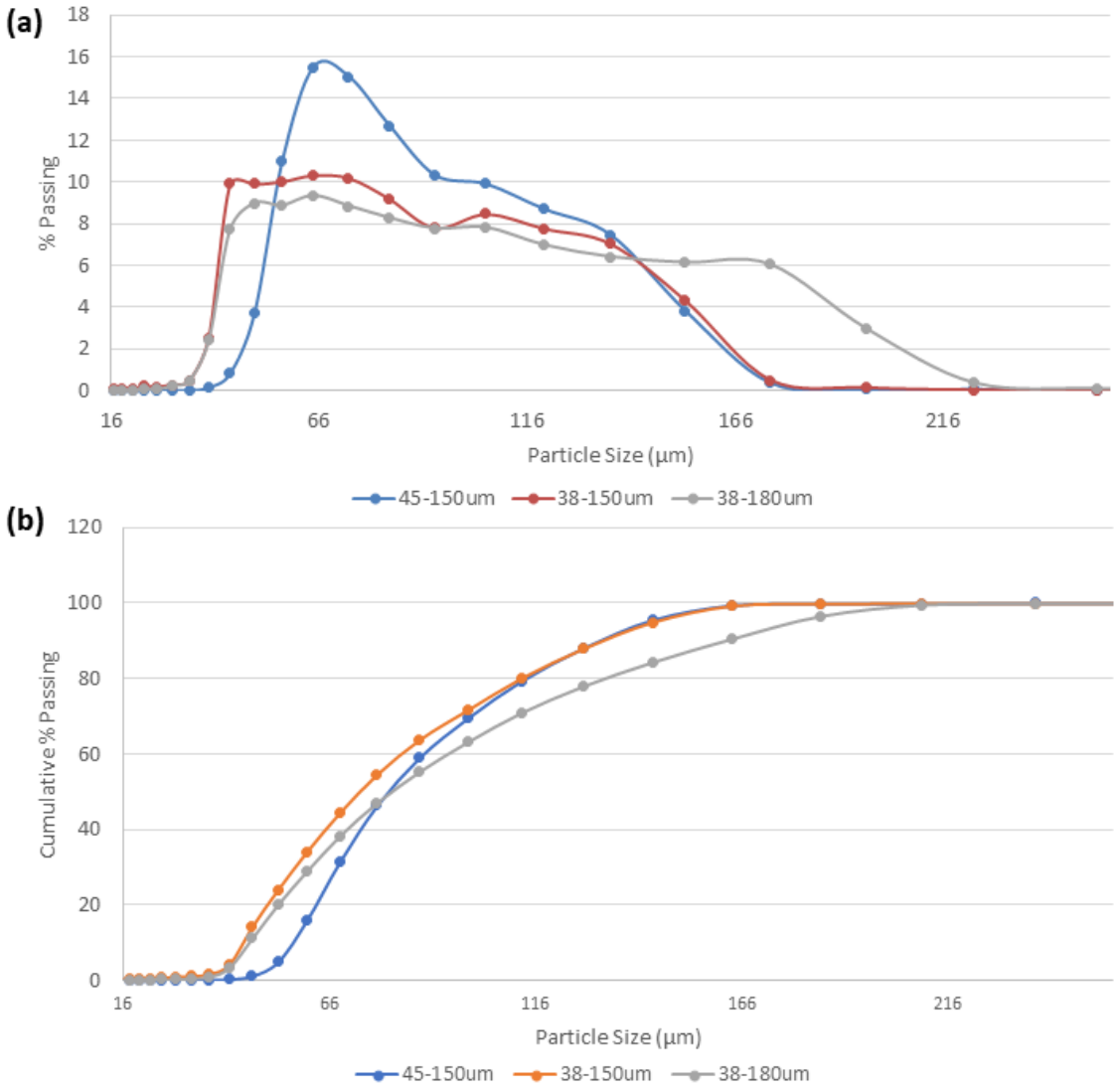


Figure 9. x_area particle distribution; a) standard distribution; b) cumulative distribution.

XFe_max

xFe_max is the measure of the particle breath, which is closely related to the observed sieve analysis. Figure 10 shows the xFe_max particle projection measurement taken from an arbitrary particle.

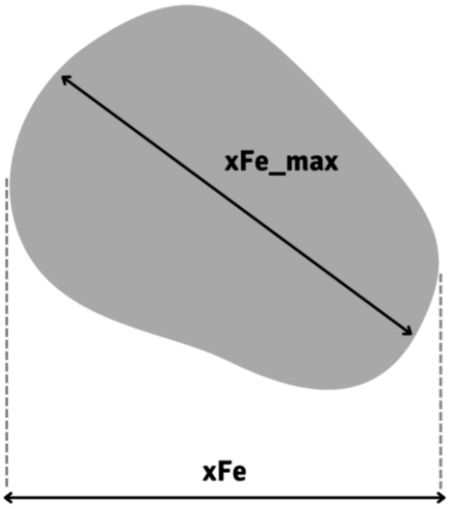


Figure 10. xFe_max particle projection.

The accumulated xFe_max distribution for PSD 45-150 µm, 38-150 µm, and 38-180 µm is derived based on the measurements collected from the Camsizer. The graph Figure 11 below shows both the cumulative and general distribution of particle present is a sample set for all three PSDs. Similar to the x_area and xc_min, the xFe_max measurements are biased towards the smaller powder size distribution range for all powders, with a non-Gaussian distribution, and the particle size distribution is similar to the reported diameter of the different PSDs.

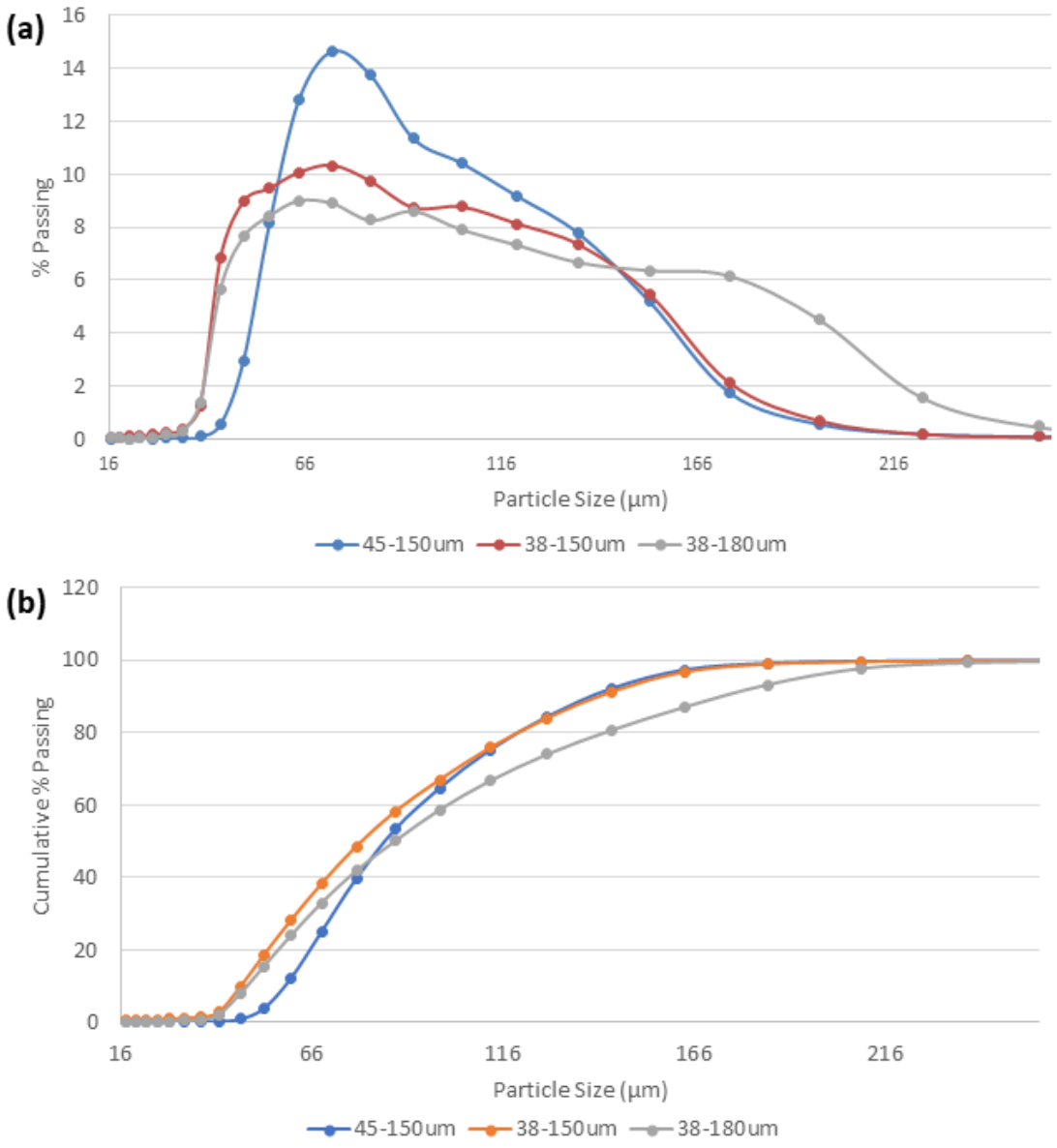


Figure 11. xFe_max particle distribution; a) standard distribution; b) cumulative distribution.

Sphericity

Sphericity measures the circularity of a particle on a scale from 0 to 1. Particles closer to a spherical shape have a sphericity value of 1 and a more irregularly shaped particle has a value close to 0. The equation that defines the sphericity is:

$$\frac{4\sqrt{A}}{P^2} \quad \textbf{(1)}$$

where P is the measure circumference of the particle and A is the calculated projected area. Based on the three different measurements collected xc_min, xFe_max, and x_area, the sphericity is calculated for all PSD's measured. Figure 12 below represents the equivalent sphericity using the various defined powder morphology measured in this study, specifically, xc_min, xFe_max, and x_area. Powder particles appear to be highly spherical; this is typical for plasma atomization.

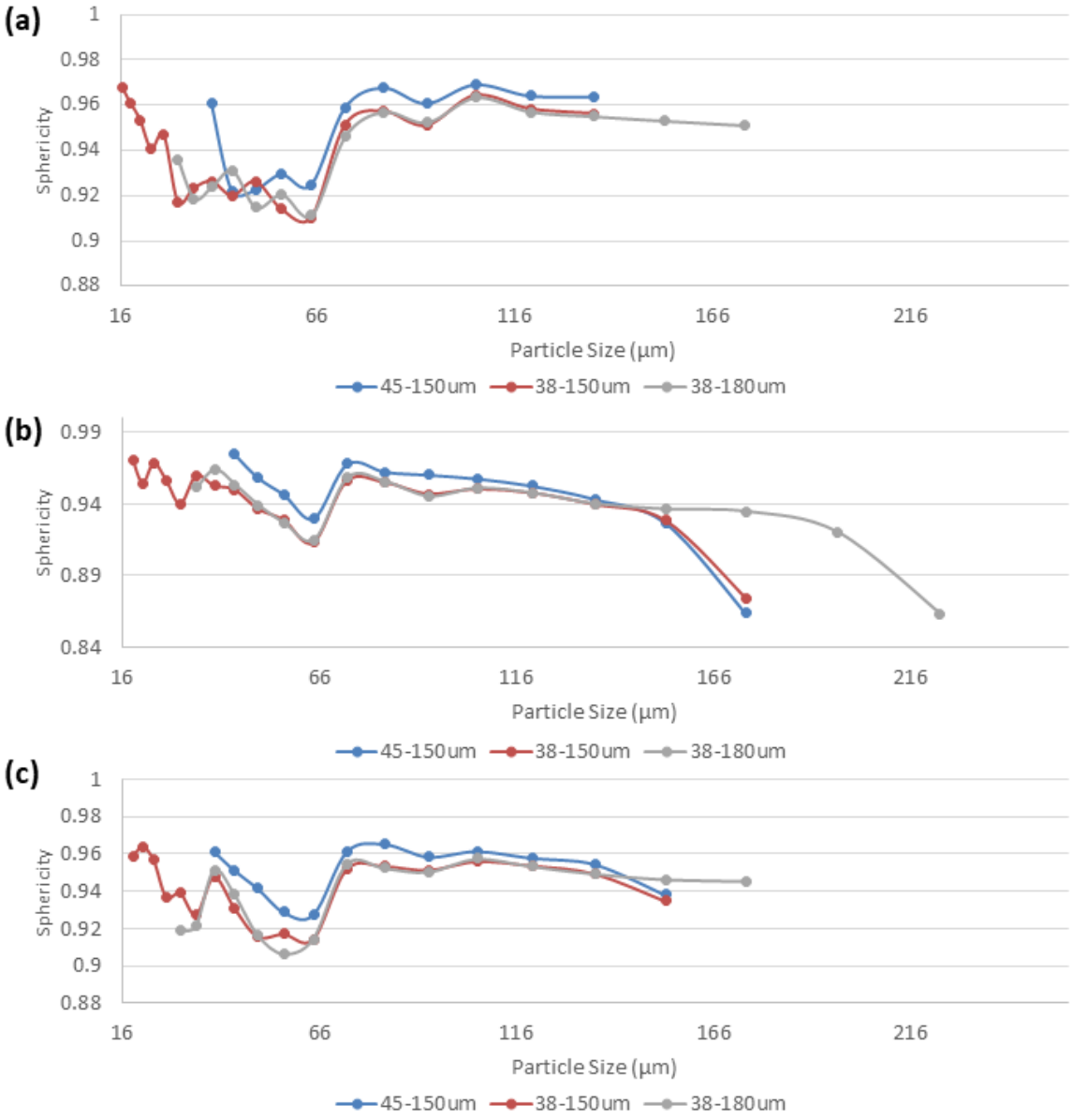


Figure 12. sphericity vs particle size plots for all measured size parameters; a) xc_min; b) x_area; c) xFe_max.

Firstly, the overall trend of all the different powder morphology diameter measurements are consistent with each other. For example, in Figure 12 all the measured morphology, 45-150 µm has the highest sphericity and 38-150 µm, & 38-180 µm have very similar sphericity measurement.

The smaller particles size in the bulk feedstock appears to conform to high sphericity. This means that the non-typical PSD (38-150 µm and 38-180 µm) ranges show promise to be utilized in the EBM process and potentially improve the economics of powder consumption by increasing powder yield for EBM. Additionally, in Figure 8, Figure 9, and Figure 11 all the reported diameter measurement showcases a very similar particle size distribution. This occurrence points to the spherical nature of the particles, especially when comparing the xFe_max to the x_area, where the similar particle size distribution identifies the high sphericity of the overall virgin Ti-48Al-2Cr-2Nb powder.

Another trend identified in the morphology analysis is the fluctuation of the measured sphericity as the particle size changes. Regardless of the PSD and diameter measurement used to derive the sphericity, the particle size ranging from 0 – 66 µm (approximately) produces a higher deviation in the measured sphericity values, with the lowest overall values in each category. Therefore, the smaller particles in the virgin powder are usually not perfectly spherical in shape as compared to the higher particle sizes. However, the sphericity difference is not expected to largely influence the EBM-printing result s when using the Ti-48Al-2Cr-2Nb powder, especially when the lowest measured sphericity is approximately 0.9 (on a scale from 0 - 1).

2.3.3 Powder rotating drum (GranuDrum)

Understanding how powders perform is crucial for ensuring process efficiency and high-quality final products. One important factor that affects powder performance is its flowability. The GranuDrum device, a powder rotating drum, is an automated tool that measures rheological properties, specifically flowability by utilizing the rotating drum method.

Analysis

Based on the description of this method of calculating flowability, the three different PSD's will be compared to identify potential trends that occur when the PSD changes. The angle of repose for all three PSD's at different speeds are represented in the Figure 13 below. Based on what is known about the repose angle, at a lower speed, the angle reported is relatively similar, however, as the speed is increased the narrower PSD (45-150 µm) projects a lower repose angle in comparison to the wider PSD's (38-150 and 38-180 µm). Therefore PSD 45-150 µm is projected to have the best flowability among the different feedstocks. Additionally, PSD 38-150 µm has a lower repose angle compared to

PSD 38-180 µm, therefore PSD 38-150 µm has a better flowability than PSD 38-180 µm. When observing the trends in the figure below, there is a correlation between the powder size range and the flowability. A narrower PSD provides a better flowability than a wider PSD range.

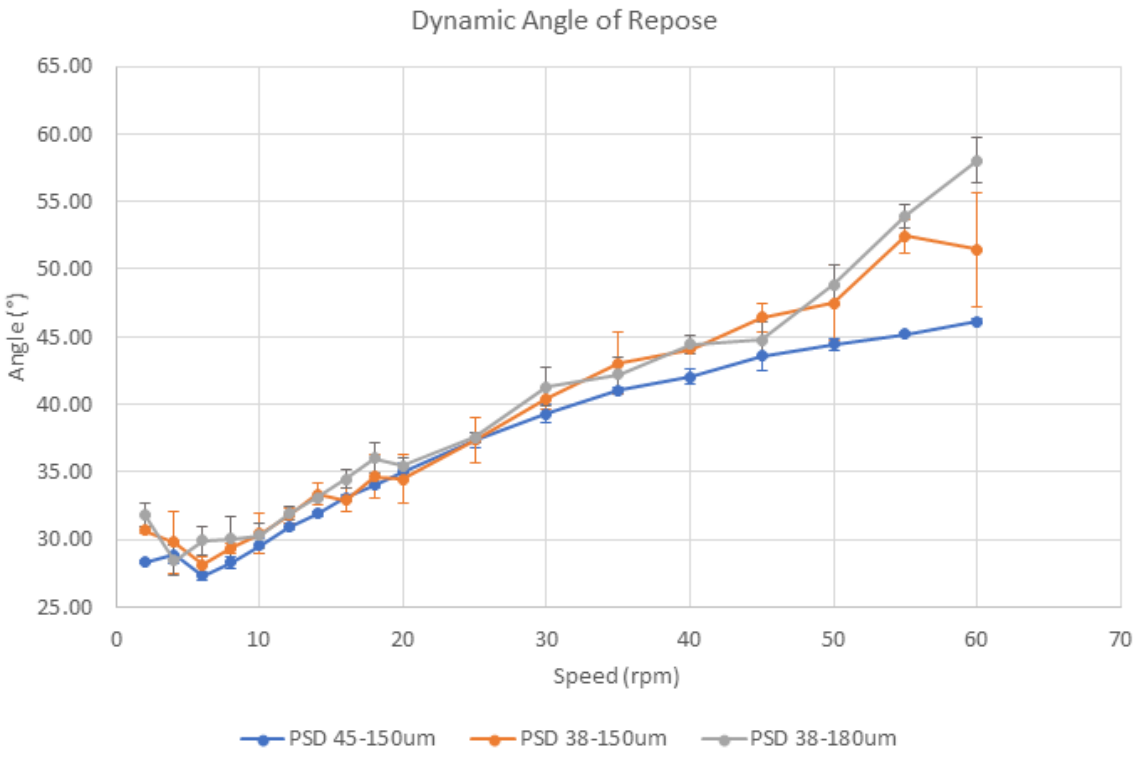


Figure 13. Dynamic angle of repose for PSD 45-150 µm, 38-150 µm, and 38-180 µm.

In Figure 14, the cohesive index of the PSD 45-150 µm is the lowest out if the examined feedstock. Throughout the GranuDrum analysis with various speeds, the cohesive index remains in the "good" cohesion range. The other PSD's measured show a higher cohesion level in comparison to the PSD 45-105 µm. However, the widest PSD (38-180 µm) shows a lower cohesion than the 38-150 µm as the speed increases. The 38-150 µm particles enters the "poor" cohesion level at the highest speed in this GranuDrum analysis. Based on this trend, it is likely that having smaller particles in the distribution increases cohesion of the bulk. The smaller particles have a much smaller gravitational force and more frictional forces present as compared to a higher particles size, with a higher weight and volume, therefore gravitational force is considerable in this regard. Based on this initial understanding, bulk

particles with smaller particles in larger percentages appears to produce less cohesive flow in the feedstock when comparing the 38-150 µm and the 38-180 µm powder classes. The wider PSD does have smaller particles in the bulk, however there is presence of larger particles so the feedstock is not predominantly dominated by smaller particles.

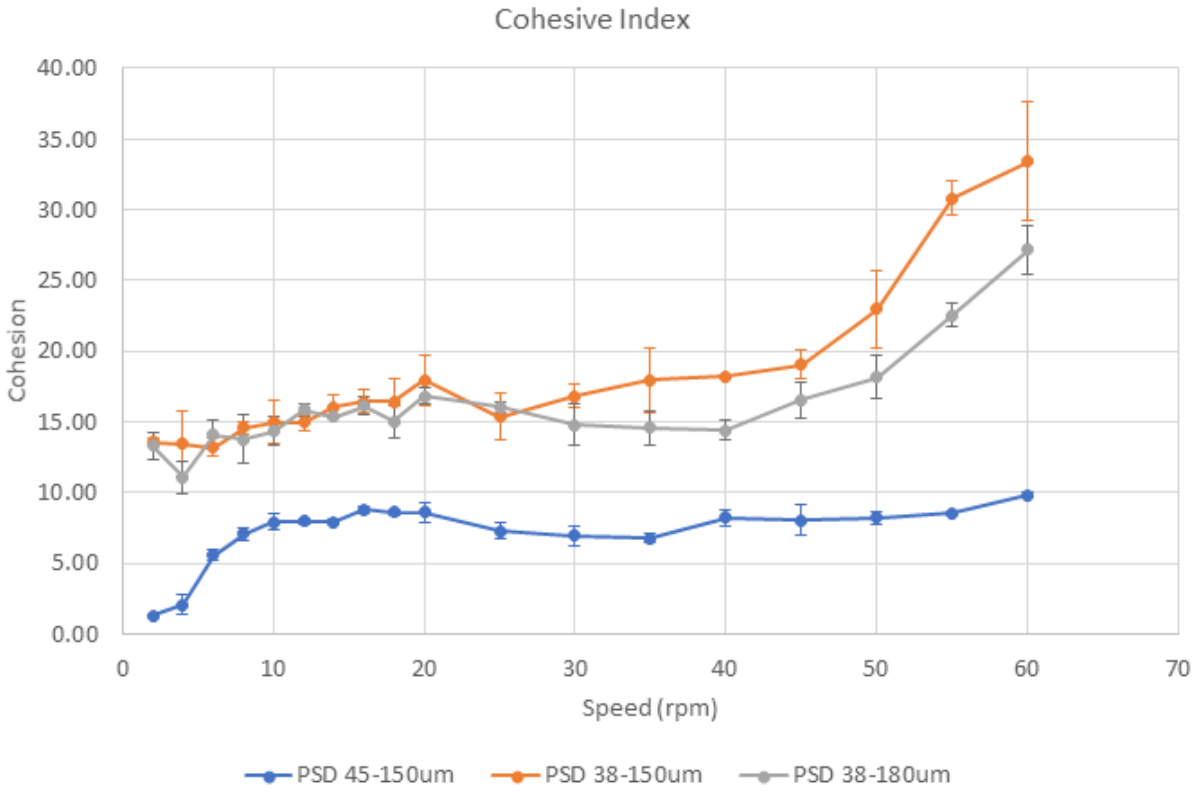


Figure 14. Cohesive index for PSD 45-150 µm, 38-150 µm, and 38-180 µm.

2.3.4 Powder tap density (Granupack)

The powder tap density is another analysis conducted on the Ti-48Al-2Cr-2Nb powder received from AP&C to analyze. This analysis investigates the packing density of the powder used in this experiment.

Analysis

The Table 3 below show the bulk density of the different powders at the beginning of the experiment (ρ[B]), the end of the experiment (ρ[T]), and the extrapolated bulk density value for an infinite amount of taps (ρ[∞]).

Table 3. Table of bulk density for PSD 45-150 µm , 38-150 µm , and 38-180 µm and the calculated Carr index and Hausner ratio powder flowability.

PSD	ρ(B) (g/mL)	ρ(T) (g/mL)	ρ(∞) (g/mL)	Carr Index (C)	Hausner Ratio (Hr)
45-150 µm	2.33±0.01	2.57±0.01	2.64±0.01	0.093	1.103
38-150 µm	2.38±0.00	2.64±0.01	2.71±0.01	0.098	1.109
38-180 µm	2.40±0.01	2.66±0.00	2.73±0.00	0.098	1.108

The results of the GranuPack analysis show some differences between the different powders in Figure 15. PSD 45-150 µm has the smallest packing density life cycle, while PSD 38-150 µm and 38-180 µm have similar result, with PSD 38-150 µm performing slightly better. Therefore, smaller powder particles appear to positively affect the resulting packing density to a much higher effect than larger particles. A higher packing density is preferred in the EBM process to reduce the risk or large pore defect formation and improve the overall repeatability of the process [54].

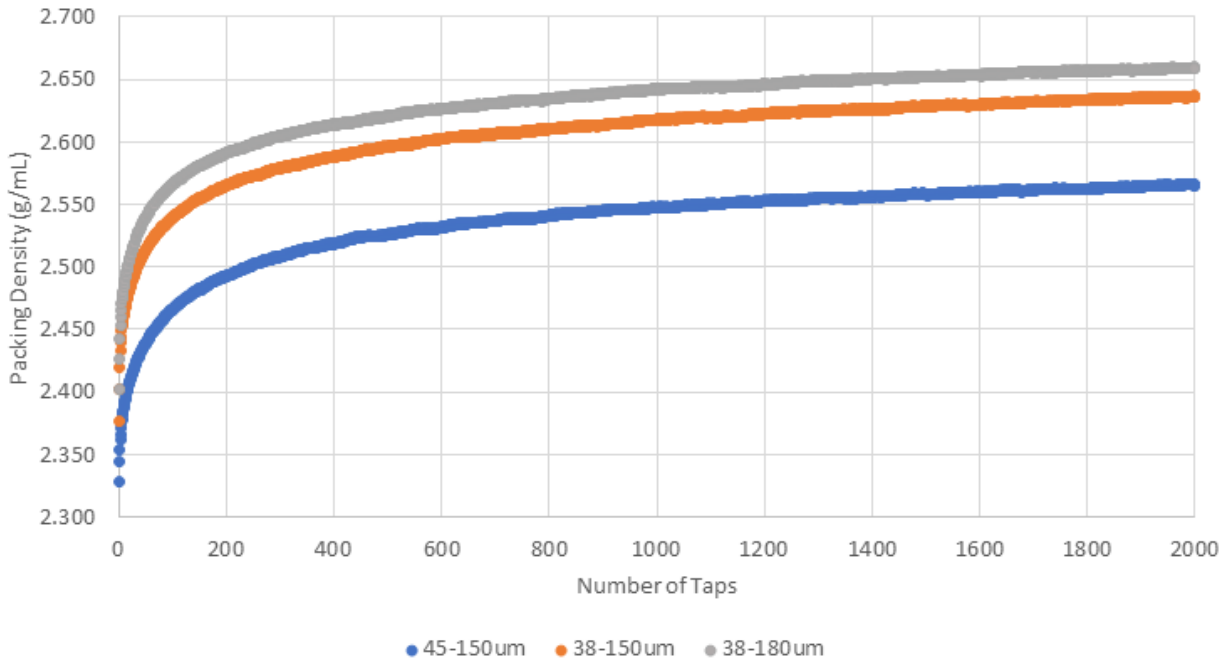


Figure 15. Shows the average packing density measured from the GranuPack machine for the Ti-48Al-2Cr-2Nb powder.

Another way to measure the flow properties is through using indexes and ratios like the Compressibility Index (C) and the Hausner ratio (HR), which are both similar in the information they portray and the information utilized to calculate the data [55]. C informs on the compressibility of the powder during EBM process and the HR details the cohesive nature of the powder measured in this experiment. C values ≤10 and HR values between 1.00 – 1.11 are considered to have excellent powder flowability [52]. Based on the indexes, the powder measured in this study all have excellent flowability. The tapped density (or end of experiment density) and the bulk density are the factors utilized to calculate the indexes [56].

$$\textbf{Carr's index (C)} = \frac{\textbf{Tapped density } (\rho_T) - \textbf{Bulk denisty } (\rho_B)}{\textbf{Tapped density } (\rho_T)} \text{ [56]} \quad \textbf{(2)}$$

$$\textbf{Hausner ratio (HR)} = \frac{\textbf{Tapped density } (\rho_T)}{\textbf{Bulk denisty } (\rho_B)} \text{ [56]} \quad \textbf{(3)}$$

2.3.5 Hall/Carney powder flow

Powder flow can also be measured using the Hall and Carney analysis. This analysis gives a preliminary insight into the powder flow within the EBM system. Analysis on the powder flow control is essential when creating EBM-printed part with repeatability [57]. Therefore, analyzing how powder flows and layers in the EBM chamber provides an understanding on the effects of powder feedstock in EBM [57].

Analysis

The resulting flow rate measured based on the Carney/Hall experiment performed is as shown in Table 4. There is a noticeable difference in the flow rate for each powder distribution. The reference powder, PSD 45-150 µm, is shown to have the lowest flow rate measured. The flowrate is heavily dependent on the geometry of the powder particles, where a smaller powder particle feedstock tends to have a better flow rate. In this study, all three PSD's showcase similar flow rate behavior in the experimental trials, with PSD 38-150 µm and PSD 45-150 µm having the lowest overall flow rate and PSD 38-180 µm having a slightly higher flow rate that is credited to the presence of larger powder particles. However, it is important to note that Hal/Carney measures a singular powder flow behavior, which often does not fully represent the spreading behavior in the powder-bed [57]. Therefore, the reported flow rate is more of a general or preliminary analysis to the powder behavior in the EBM process.

Table 4. Table of hall and carney flow rate results for PSD 45-150 µm, 38-150 µm, and 38-180 µm.

	PSD	Trial 1	Trial 2	Trial 3	Average FR
Hall Flow rate	45-150 µm	30.3	30.5	30.1	(30.15±0.2)/50g
	38-150 µm	31	30.8	30.3	(30.88±0.26)/50g
	38-180 µm	33.5	32.1	31.8	(32.31±0.91)/50g
Carney Flow rate	45-150 µm	10.7	10.7	10.6	(10.7±0.0)/150g
	38-150 µm	10.7	10.7	10.6	(10.7±0.0)/150g
	38-180 µm	10.8	10.5	10.5	(10.6±0.0)/150g

2.3.6 Powder computed tomography

The feedstock used for the computed tomography (CT) study was reused powder, therefore, some changes can occur in the powder analysis as a result of the process [52,58]. When powder is reused, it undergoes some degradation (broken, shattered, elongated, and deformed powder particles) which leads to a mixture that is a bit distinct from the original powder [52]. These deformations are often due to the sintering and melting of particles during the EBM process, particles collision, and sieving process during power recovery [52,55]. Changes in the flowability can be observed due to modifications in the surface characteristics and the creation or dispersion of agglomerates. However, the most significant change occurs in the Particle Size Distribution (PSD) [27].

Analysis - general

The data extracted from the CT scan and data processing software was utilized to present information on the powder particles and porosity, for all PSDs utilized in this study (45-150 µm, 38-150 µm, 38-180 µm). This analysis is conducted on re-used powder to simulate similar particle properties as during EBM-printing. Comparison between all PSD measured is confirmed based on the trends identified in the computed tomography scans. Table 5 is defined based on the defined powder particle and porosity classified in the dragonfly software

Table 5. Table of particle and porosity count identified in the quantified data.

PSD	Powder Particle Count	Porosity Count	Particle: Porosity ratio
45-150 µm	21,953	760	28.89
38-150 µm	18,463	429	43.04
38-180 µm	6,280	918	6.84

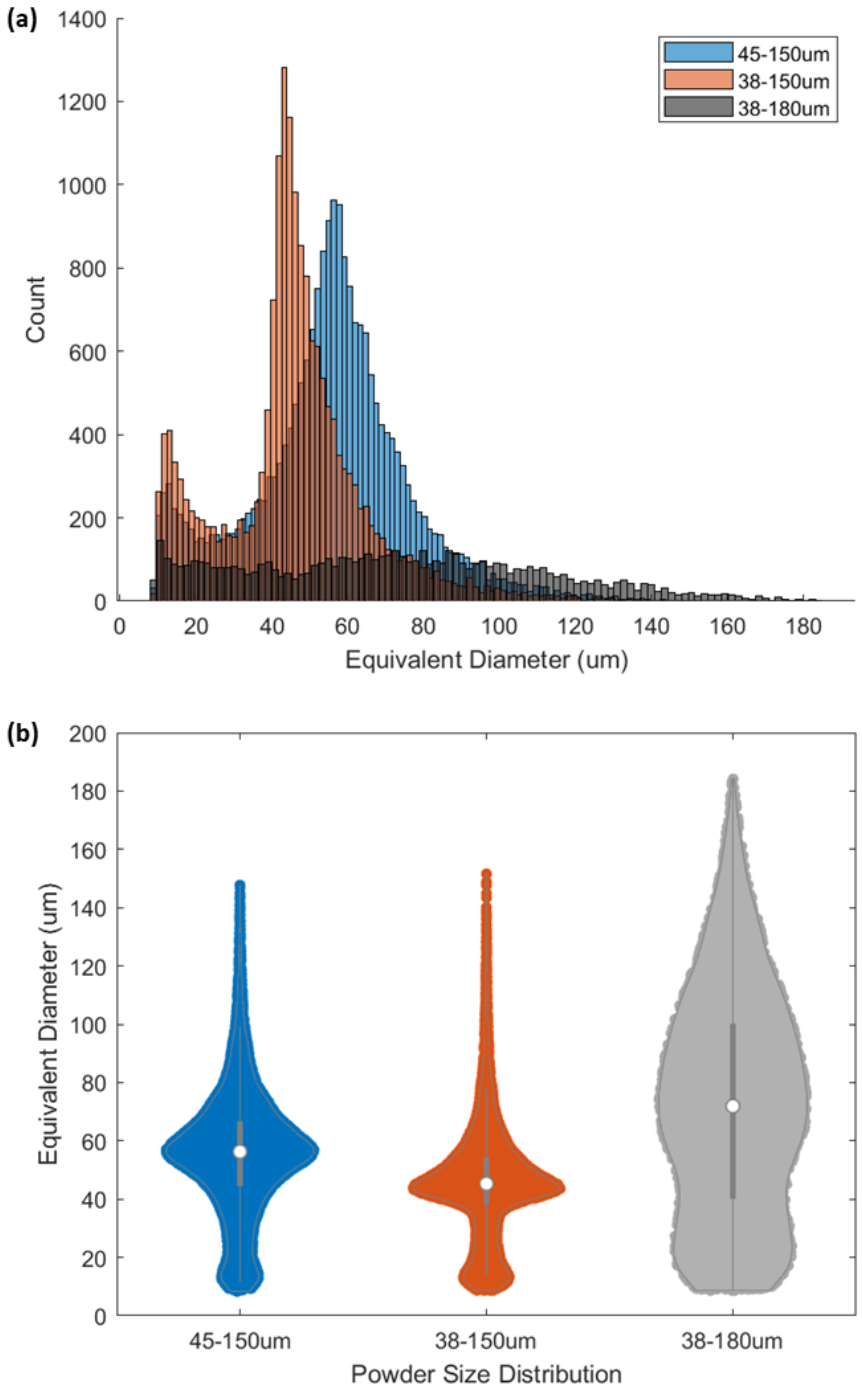


Figure 16. Showcases distribution of Equivalent Diameter for All PSD measured; a) Histogram of Equivalent diameter for PSD 45-150 µm, 38-150 µm, and 38-180 µm; b) Violin plot showing distribution of Equivalent diameter for PSD 45-150 µm, 38-150 µm, and 38-180 µm.

Based on the distribution of equivalent diameters for all studied PSDs, differences in the re-used powder are identified. For all PSD's, the distribution is within the expected range, however, equivalent diameter lower than the limits for all PSD's are identified in the sample size, potentially as a result of the processing of the reused powder or excessive noise created during data processing. As seen in Table 5, the samples size is much larger in the reference PSD as compared to the other PSD's and potentially influences the results seen. PSD 38-150, shows a similar distribution as the reference PSD, which is expected when considering the PSD range of both powder bulk. PSD 38-180 shows a larger range in the distribution than the other powder bulk samples, which is also an expected result considering PSD 38-180 µm is the widest ranged PSD in this study.

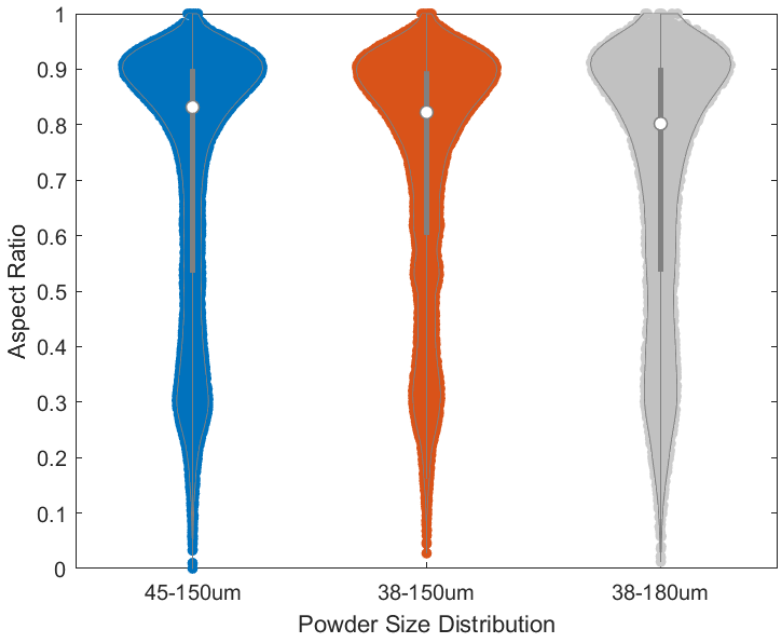


Figure 17. Represents the violin plots derived for the Aspect ratio of all the analyzed powder set in this study: PSD 45-150 µm, 38-150 µm, and 38-180 µm.

Analysis – PSD 45-150 µm

PSD 45-150 µm is the reference powder within the powder set provided for this study and is also the narrowest PSD. The sample size of the powder bulk scanned for this PSD is 21,953 particles, and in these particles, about 760 pores where confirmed.

For the histogram figures shown in Figure 18, the equivalent diameter matches up with the expected distribution, with the closest approximation being the x_area as shown in Figure 9. There are two peaks in the histogram that shows a higher particles count. The lower peak at a smaller equivalent diameter and the larger peak at approximately 20 µm and 60 µm respectively are the prominent point in the Figure 18. The existence of the peak in powder particles a lower than 45 µm (45 µm being the lowest diameter size in the reference PSD 45-150 µm) compared to the data in Figure 9, may be indicative that powder particles appear to be broken down during printing and can remain in the powder feedstock after processing for reuse purpose [52]. Majority of the remaining powder bulk is within the expected range of PSD 45-150 µm as seen in the highest peak in Figure 18. Additionally, the histogram for the powder porosity showcases a prominent count at the lowest equivalent diameter. However, the respective powder particle that contains the porosity mainly appears in the larger particles size as seen in Figure 18(a). Of note, this could be an artefact of the CT scanning resolution creating limitations in the size of powder particles and pores that can be detected.

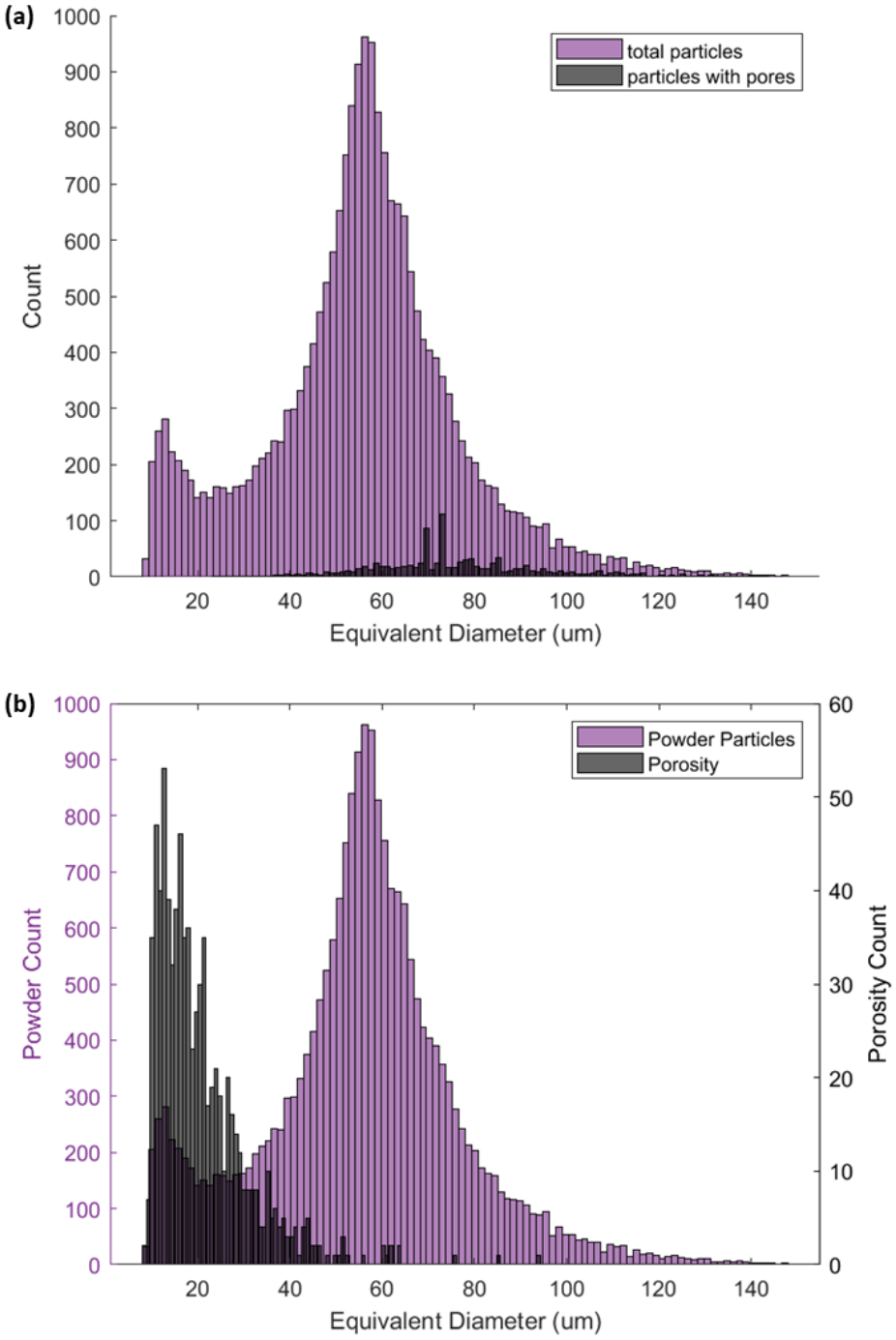


Figure 18. Histogram of calculated equivalent diameter of PSD 45-150 µm powder with; a) portrays the total powder particle distribution and particles with porosity distribution; b) portrays total powder particle distribution and porosity distribution.

For the histogram figure shown in Figure 19, the aspect ratio is spread across the range from 0 to 1, with the highest count at the higher aspect ratio. Therefore, majority of the powder bulk PSD 45-150 µm remains spherical in shape with processing. Additionally, the powder porosity aspect ratio is much higher than the particles, with an approximate lowest value of 0.5, hence the porosity is predominantly spherical.

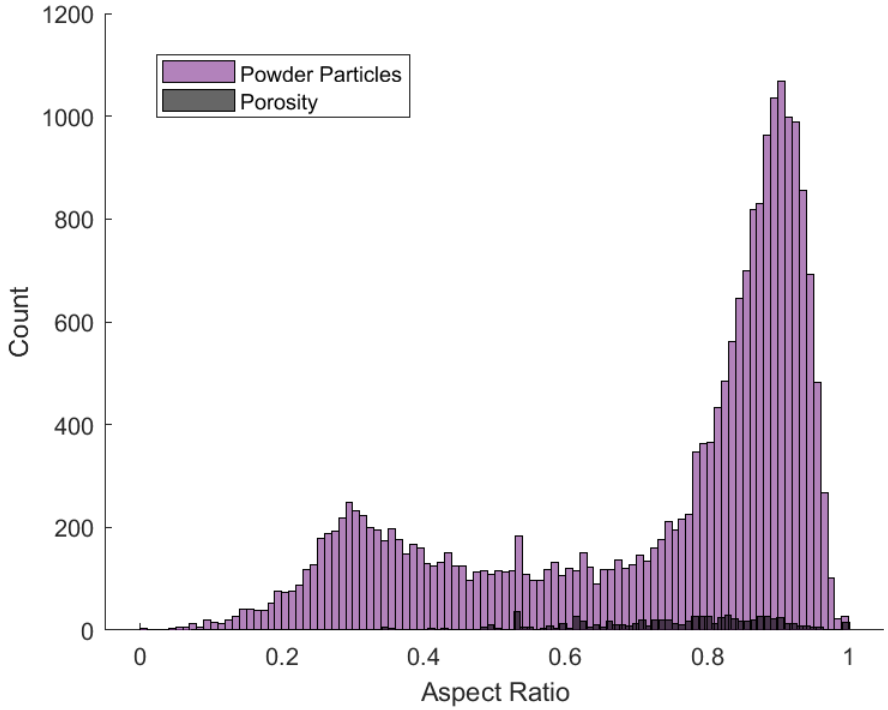


Figure 19. Histogram of measured aspect ratio of PSD 45-150 µm powder that portrays the total powder particle distribution and porosity distribution.

In order to further analyze the trends in the shape of the re-used particles with PSD 45-150 µm, the shape of the particles were categories into spherical and non-spherical particles. The feature used to create this demarcation is the aspect ratio. Aspect ratio values >= 0.7 are categorized into the spherical particle and values < 0.7 are defined as non-spherical particles. Based on Figure 20, there is a larger particle count for samples with a spherical shape as compared to the non-spherical. Another trend identified is the higher volume particles tend to be non-spherical in shape according to Figure 20. This may be indicative of powder satellite formation, powders mechanically breaking or clustering together during processing; these phenomena have been reported previously for EBM powders [52,58].

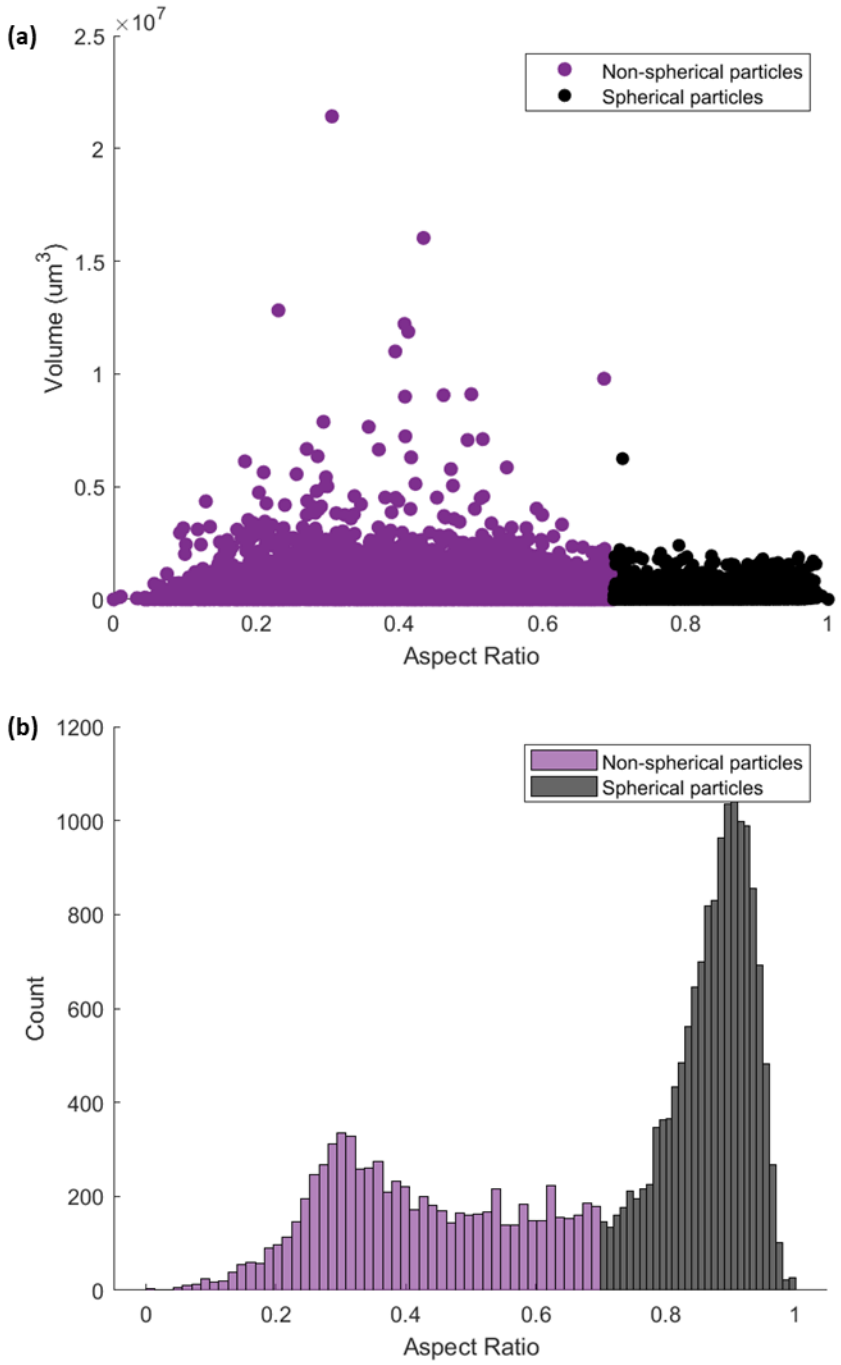


Figure 20. Figure showcases aspect ratio of PSD 45-150 µm powder with; a) portrays the total powder particle distribution aspect ratio against the volume; b) portrays total powder particle histogram distribution.

Analysis – PSD 38-150 µm

PSD 38-150 µm is the second widest PSD ranged powder within the powder set provide for this study, with the same upper threshold as the reference (150 µm) but with smaller particles at the lower threshold of the range (38 µm). The sample size of the powder bulk scanned for this PSD is 18,463 particles, and in these particles, about 429 pores where confirmed.

For the histogram figures shown in Figure 21, the equivalent diameter matches up with the expected distribution. There are two peaks in the histogram that shows a higher particles count. The lower peak at a smaller equivalent diameter and the larger peak at approximately 20 µm and 50 µm respectively are the prominent point in the Figure 21. However, a noticeable difference between the 38-150 µm PSD and the reference is the slightly lower equivalent diameter (50 µm as compared to 60 µm) at the highest peak count on the histogram. The existence of powder particles lower than 38 µm (38 µm being the lowest diameter size in the reference PSD 38-150 µm) could be a result of powder particles breaking down during printing and remain in the powder feedstock after processing for reuse purpose, or can be a result of noise created during the pre-processing of the data. Majority of the remaining powder bulk is within the expected range of PSD 38-150 µm as seen in the highest peak in Figure 21. Additionally, the histogram for the powder porosity showcases a prominent count at the lowest equivalent diameter. However, the respective powder particle that contains the porosity mainly appears in the larger particles size as seen in Figure 21(a). This is consistent with the observations from 45-150 µm PSD range.

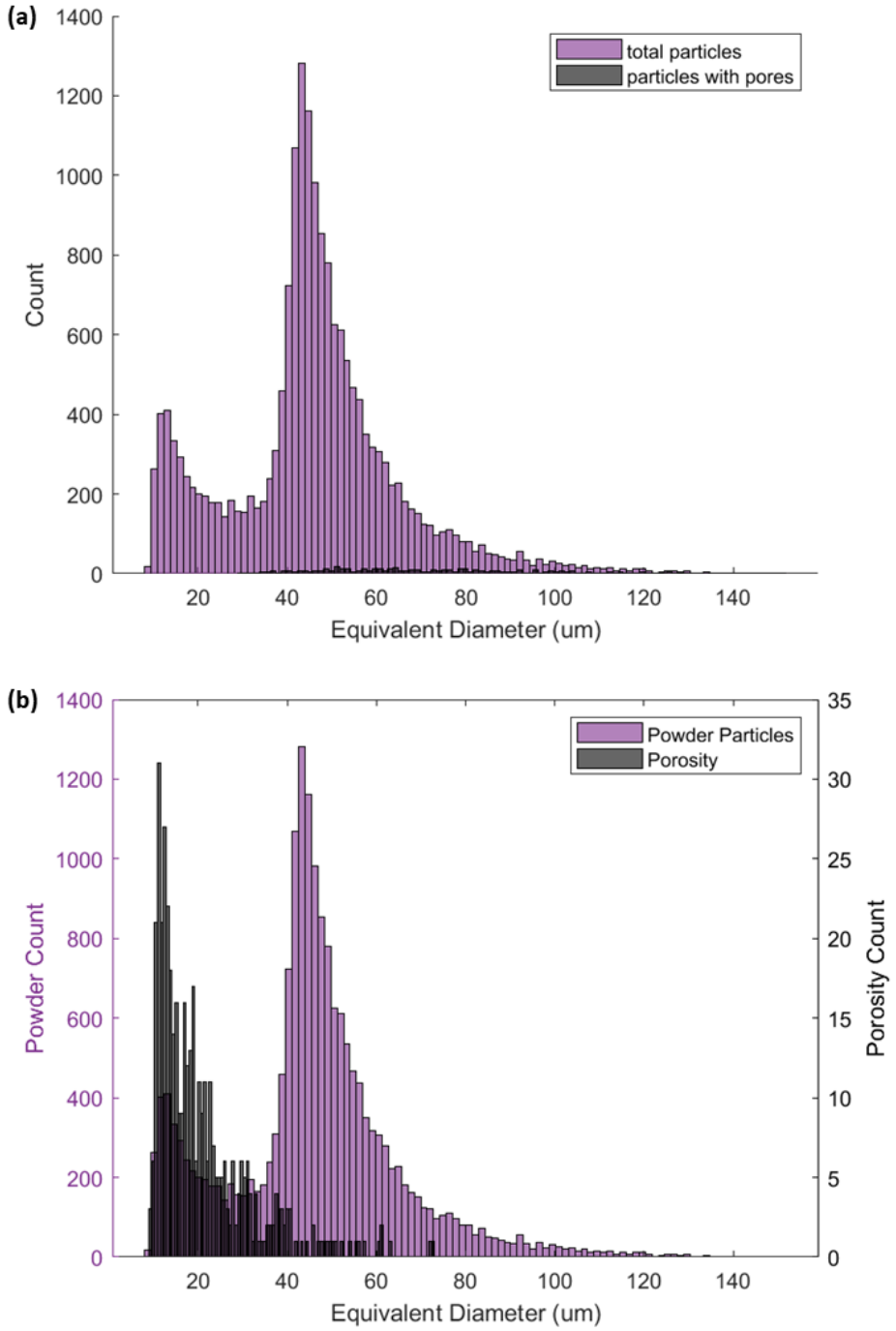


Figure 21. Histogram of calculated equivalent diameter of PSD 38-150 µm powder with; a) portrays the total powder particle distribution and particles with porosity distribution; b) portrays total powder particle distribution and porosity distribution.

For the histogram figure shown in Figure 22, the aspect ratio is spread across the range from 0 to 1, with the highest count at the higher aspect ratio. Therefore, majority of the powder bulk PSD 38-150 µm is spherical in shape. Additionally, the powder porosity aspect ratio is much higher than the particles, with an approximate lowest value of 0.4, hence the porosity is predominantly spherical.

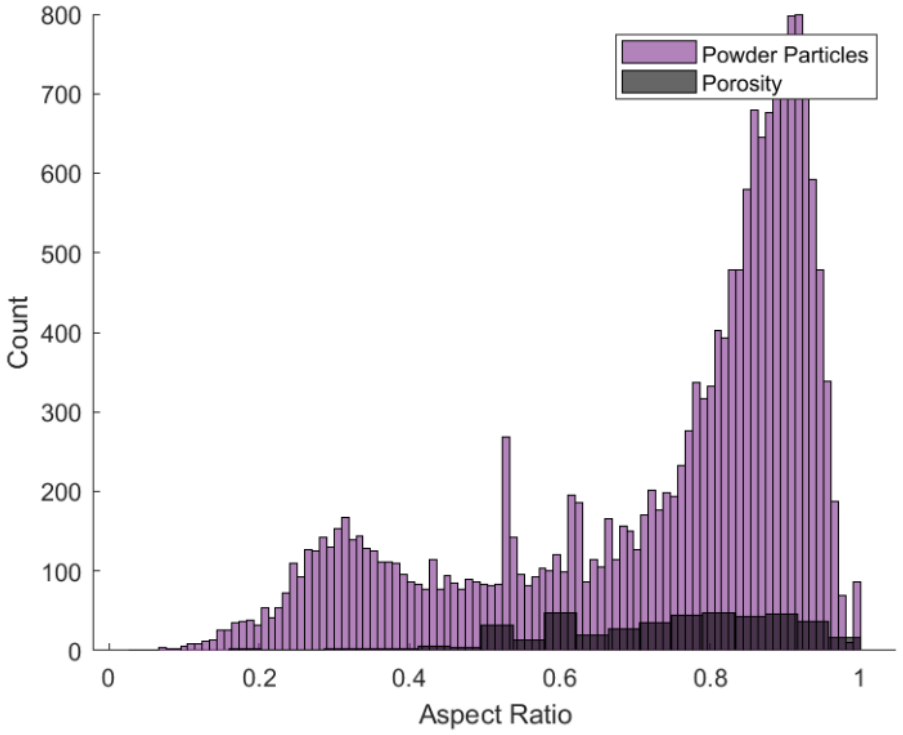


Figure 22. Histogram of measured aspect ratio of PSD 38-150 µm powder that portrays the total powder particle distribution and porosity distribution.

In order to further analyze the trends in the shape of the re-used particles with PSD 45-150 µm the shape of the particles were categories into spherical and non-spherical particles. The feature used to create this demarcation is the aspect ratio. Aspect ratio values >= 0.7 are categorized into the spherical particle and values < 0.7 are defined as non-spherical particles. Based on Figure 23, there is a larger particle count for samples with a spherical shape as compared to the non-spherical. However, the present of non-spherical particles is relatively large especially in comparison to the reference PSD. Another trend identified is the higher volume particles tend to be non-spherical in shape according to

Figure 23. These trends are similar to PSD 45-150 µm where the particles that tend to have the larger volume are the non-spherical particle. The non-spherical particles are assumed to develop from the degradation of the powder during powder recovery for the re-used samples since the virgin powder sphericity is above 0.9 for the entire distribution of the PSD 38-150 µm samples as seen in Figure 12 [52]. The degradation of the powder is often attributed to the pre-sintering of the powder during the EBM-process before the recovery and the sieving of the powder particles during powder recovery [52]. The reused powder feedstock can often times contain large non-spherical particles that remain even after sieving the powder [52]. When comparing the large particles identified in the measured particles, the range of the volume for the larger particles is under $14*10^6$ μm^3, which is smaller than the 45-150 µm PSD ($12*10^7$ μm^3). This difference can be attributed to the presence of a larger quantity or percentile of lower powder particles in the PSD 38-150 µm range.

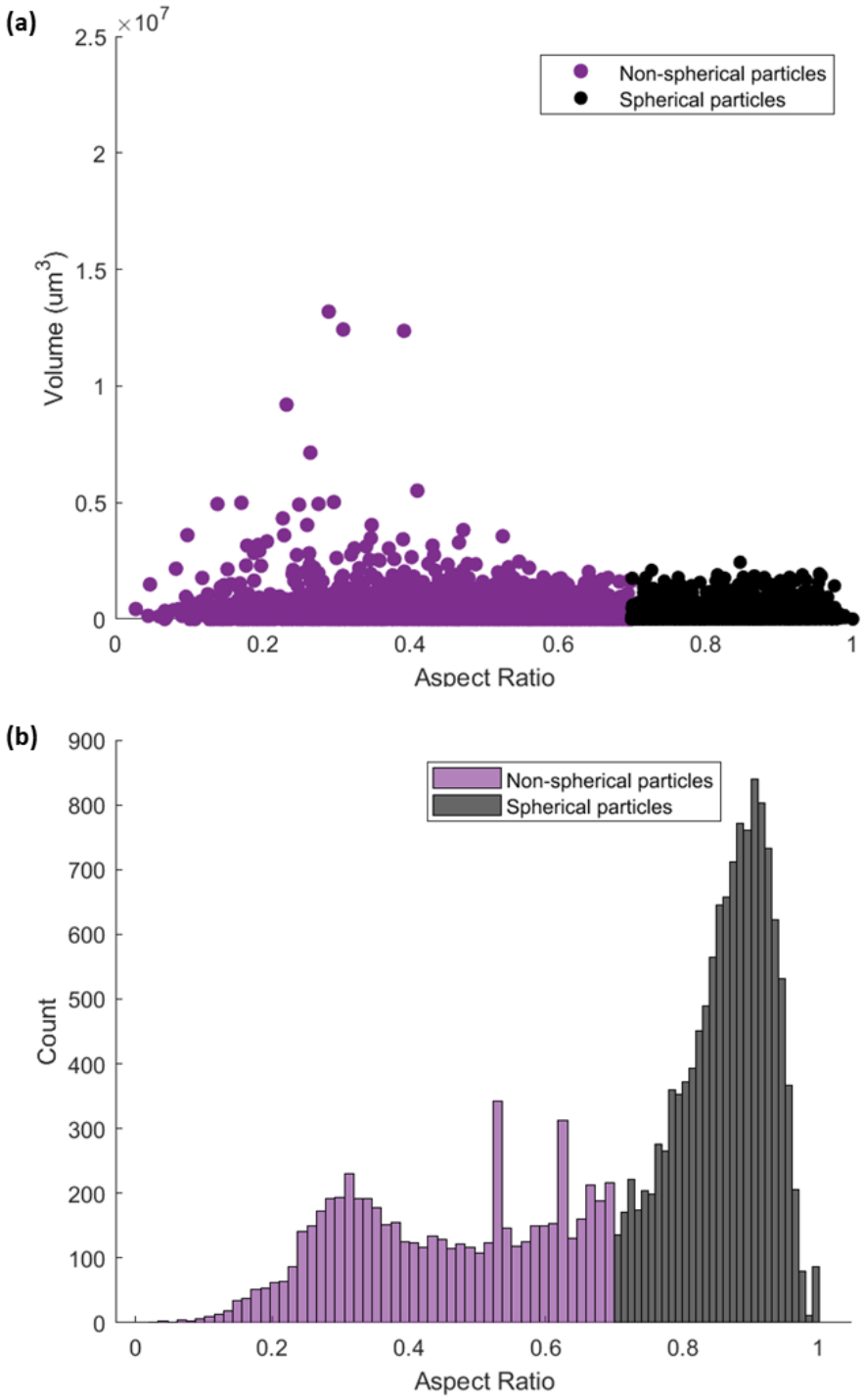


Figure 23. Figure showcases aspect ratio of PSD 38-150 µm powder with; a) portrays the total powder particle distribution aspect ratio against the volume; b) portrays total powder particle histogram distribution.

Analysis – PSD 38-180 µm

PSD 38-180 µm is the widest PSD ranged powder within the powder set provide for this study, with the highest upper threshold (180 µm) and with smaller particles at the lower threshold of the range (38 µm). The sample size of the powder bulk scanned for this PSD is 6,280 particles, and in these particles, about 918 pores where confirmed. Of note, this experiment captured a significantly lower number of particles in the CT field of view; as such, the results may be affected by this.

For the histogram figures shown in Figure 24, the equivalent diameter matches up with the expected distribution. There are two peaks in the histogram that shows a higher particles count. Both peaks have roughly similar counts. Therefore, the presence of particles at both the equivalent diameter is high. The smaller equivalent diameter and the larger equivalent diameter at approximately 20 µm and 50-80 µm respectively are the prominent point in the Figure 24. However, a noticeable difference between the 38-180 µm PSD and the reference PSD is the wider distribution of equivalent diameter at the peak count on the histogram, meaning the particles in this PSD bulk range are spread across a wider equivalent diameter. The existence of powder particles lower than 38 µm (38 µm being the lowest diameter size in the reference PSD 38-180 µm) could be a result of powder particles breaking down during printing and remain in the powder feedstock after processing for reuse purpose, or could also be a result of noise created during the pre-processing of the data. Majority of the remaining powder bulk is within the expected range of PSD 38-180 µm as seen in Figure 24.

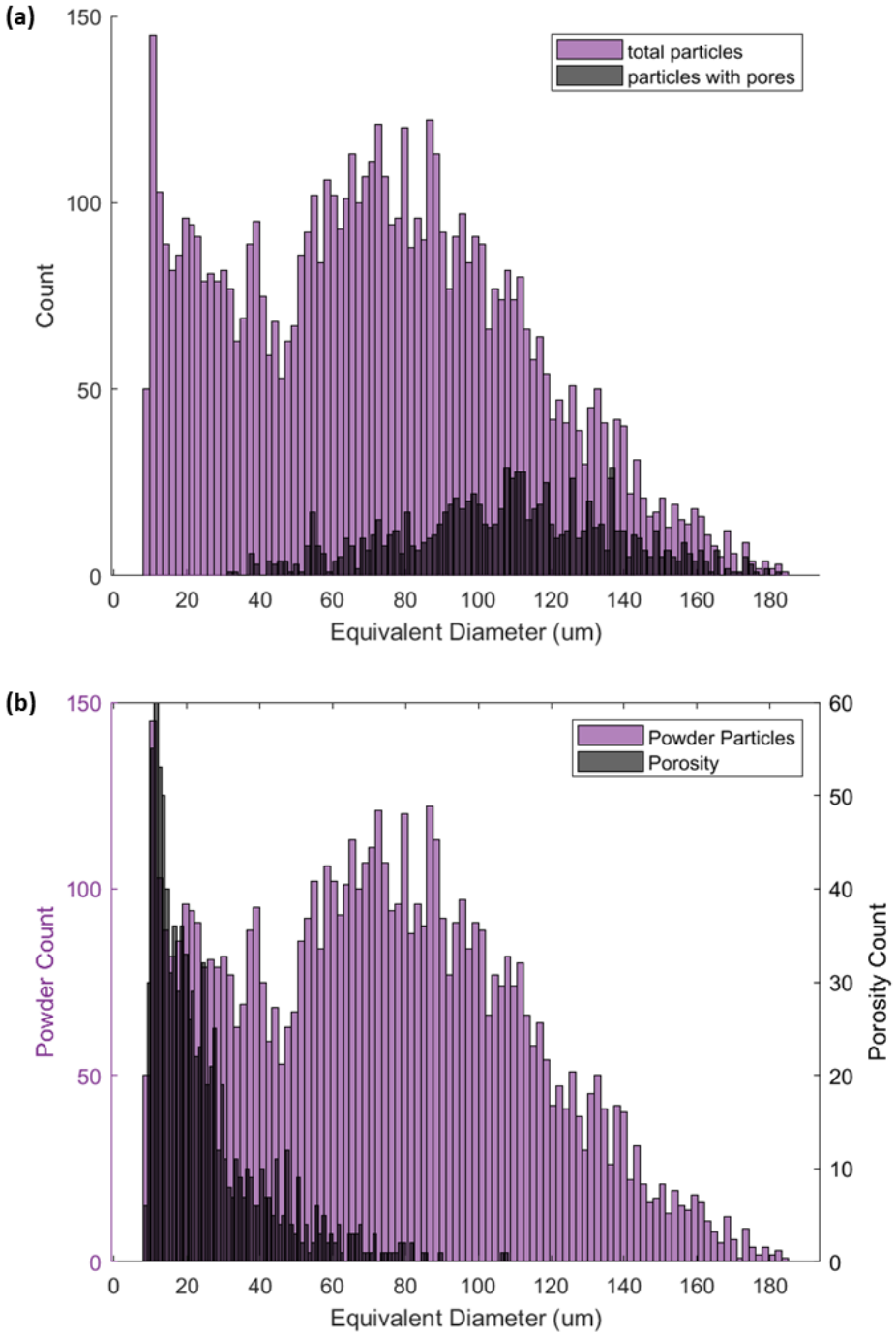


Figure 24. Histogram of calculated equivalent diameter of PSD 38-180 µm powder with; a) portrays the total powder particle distribution and particles with porosity distribution; b) portrays total powder particle distribution and porosity distribution.

For the histogram figure shown in Figure 25, similar to the PSD 45-150 µm and 38-150 µm the aspect ratio is spread across the range from 0 to 1, with the highest count at the higher aspect ratio. Therefore, majority of the powder bulk PSD 38-150 µm is spherical in shape. Additionally, the powder porosity aspect ratio is generally spread across the aspect ratio range available, with predominantly spherical shaped porosities (aspect ratio close to 1).

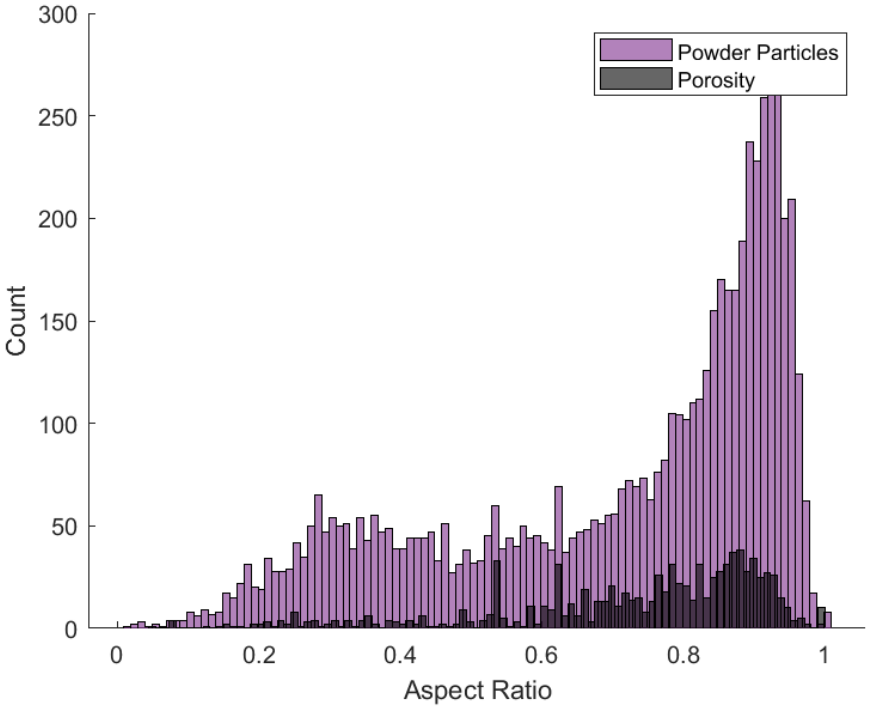


Figure 25. Histogram of measured aspect ratio of PSD 38-180 µm powder that portrays the total powder particle distribution and porosity distribution.

In order to further analyze the trends in the shape of the re-used particles with PSD 45-150 µm, the shape of the particles were categories into spherical and non-spherical particles. The feature used to create this demarcation is the aspect ratio. Aspect ratio values >= 0.7 are categorized into the spherical particle and values < 0.7 are defined as non-spherical particles. Based on Figure 26, there is a larger particle count for samples with a spherical shape as compared to the non-spherical, even more so in PSD 38-180 µm as compared to 45-150 µm and 38-150 µm. Another trend identified is the higher volume particles tend to be non-spherical in shape according to Figure 26. Potentially, larger particles

are more likely to be non-spherical after EBM printing production due to powder deformation, therefore creating the difference between the particle shapes.

These trends are similar to PSD 45-150 µm and PSD 38-150 µm where the particles that tend to have the larger volume are the non-spherical particle. The non-spherical particles are assumed to develop from the degradation of the powder during powder recovery for the re-used samples since the virgin powder sphericity is above 0.9 for the entire distribution of the PSD 38-150 µm samples as seen in Figure 12 [52]. When comparing the large particles identified in the measured particles, the range of the volume for the larger particles is under $2.5*10^7$ μm^3, which is slightly smaller than the 45-150 µm PSD ($12*10^7$ μm^3) and larger than PSD 38-150 µm ($14*10^6$ μm^3). This difference can be attributed of the PSD. The overall trend in the PSD 45-150 µm and PSD 38-180 µm is similar with PSD 45-150 µm having a few more particles with larger volume. PSD 38-150 µm however has the lowest volume range across the entire scanned sample particles.

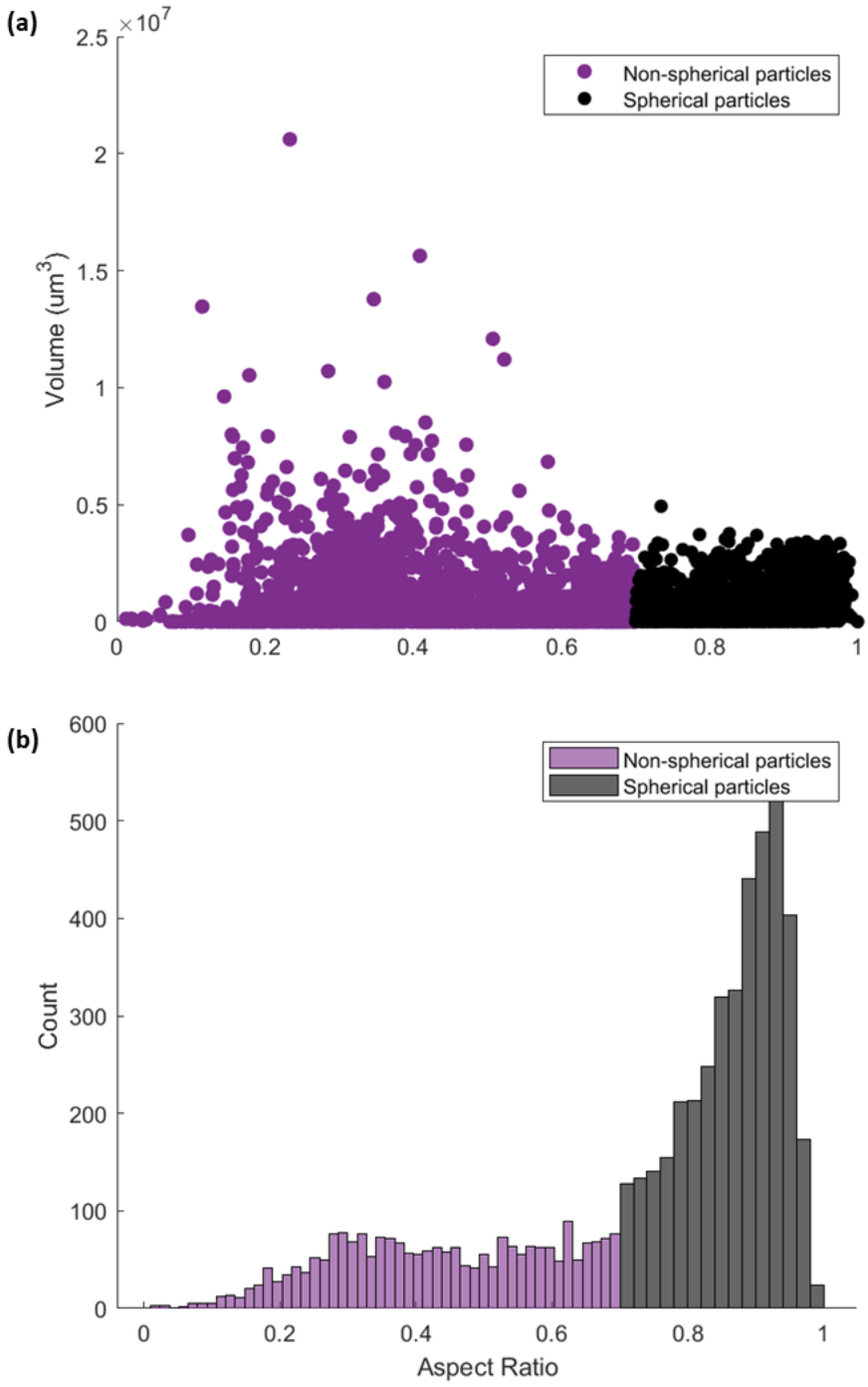


Figure 26. Figure showcases aspect ratio of PSD 38-180 µm powder with; a) portrays the total powder particle distribution aspect ratio against the volume; b) portrays total powder particle histogram distribution.

Chapter 3
Density Analysis

3.1 Introduction

Prior research in available literature predominantly centers on optimizing bulk density through process parameters in alternative technologies such as LPBF. For EBM, existing studies investigate the correlation between a small range of parameters and the relative density in EBM. In contrast, this study focuses on a broad range of EBM parameters, as well as in-depth data analysis to explore the correlation between process parameters and targets such as relative density and pore morphology. The present work will focus on elucidating relationship between process parameters and engineered features on the resulting pore properties such as bulk density, entrapped gas pores, and lack of fusion pores for Ti-48Al-2Cr-2Nb manufactured via EBM. This will be achieved through pore space CT analysis via qualitative assessments (data visualization) and quantitative assessments (density outcomes and pore space analysis).

3.2 Materials and methods

3.2.1 Powder materials

The powder used in this study is plasma atomized Ti-48Al-2Cr-2Nb (AP&C – A GE additive company) with a nominal powder size distribution (PSD) of 45-150um. This alloy contains 48 at.% Titanium, 48 at.% Aluminum, 2 at.% Niobium, and 2 at.% Chromium. A scanning electron microscopy (SEM) (TESCAN VEGA 3, TESCAN, Brno, Czech Republic) was used to study different perspectives on the internal porosities, satellite particles and overall morphology of the powders. The powder samples are mounted on a 1 cm dish to form a thin layer of Ti-48Al-2Cr-2Nb powder particles for imaging, which is then coated with gold particles to increase visibility in the SEM machine. Additionally, powder characterization was conducted on the virgin powder (as-received) using a vision-based powder size analysis instrument (Camsizer X2, Retsch, Haan, Germany), revealing quantitative data on the particle size distribution.

3.2.2 Manufacturing process and parameters

For this study, 107 distinct experimental parts were fabricated using an EBM system (Arcam A2X, GE Additive, Boston, USA). This machine allows for process parameter variations in the melting and

powder pre-heating scheme. Prior to printing the samples, the initial layer of powder and the build plate were preheated to 970°C. The accelerating voltage was held constant at 60V, and a pressure of 2×10^{-3} mbar was achieved in the fabrication chamber before commencing the entire printing process. To ensure consistency in this analysis, all printed samples had common dimensions of 20mm × 20mm × 25mm. The melt strategy employed a hatch pattern, wherein the electron beam moved along the layer either from side to side or in a criss-cross pattern, as illustrated in Figure 27.

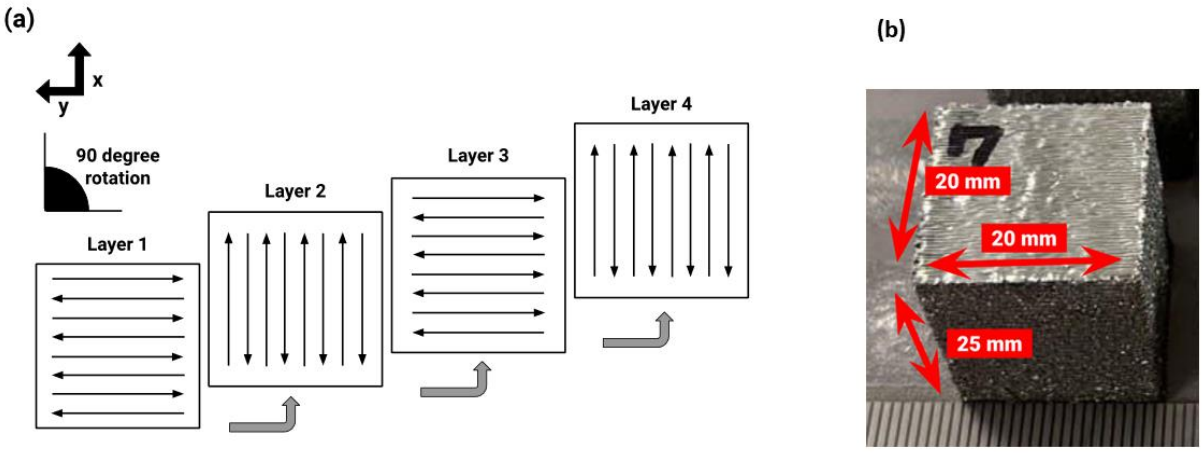


Figure 27. Schematics of the printing strategy. a) The hatch melting strategy with a melt pool moving down the layer from side to side with a 90-degree rotation; b) The dimensions of an experimental sample which mirrors the dimensions of all the EBM printed samples in this study.

This study was comprised of two experimental phases. In Phase 1, a preliminary set of process parameters was designed with the goal of attaining a high bulk relative density. Phase 2 involved testing various hypotheses to achieve a diverse range of relative density outcomes, with an aim to develop a clear relationship between a wide range of density, pore defect types and energy density. The manufacturing process of the experimental samples referred in this paper followed individual process parameter combinations for each of the EBM printed coupons as seen in Supplementary Table 1. In the EBM process, the critical parameters that often are used to represent the applied energy are: line offset, focus offset, beam speed, beam current, and beam spot size. Two engineered features were derived based on process parameters values, the volumetric energy density and normalized enthalpy.

Synthetic parameters representing energy input

Normalized enthalpy (NE) and volumetric energy density (VED) were used as an approximation for the applied energy on the EBM process. Both of these engineered features are calculated based on the input process parameters. NE accounts for the thermal properties of the Ti-48Al-2Cr-2Nb material and the EBM process parameters to calculate a dimensionless parameter as an estimate of the energy applied [59,60]. The resulting quantitative number represents the normalized energy applied at a singular spot on the powder bed when melting and joining the layers.

$$h^* = \frac{A*P}{\frac{k*T_m}{\alpha}*\sqrt{\pi\alpha v D^3}} \text{ [59]} \qquad \alpha = \frac{k}{\rho*c_p} \text{ [61]} \qquad \textbf{(4)}$$

The normalized enthalpy (h*) calculation is represented in Equation 4, where absorptivity (A, [%]), power (P, [W]), thermal conductivity (k, $[cm * C]$), melting temperature (Tm, [C]), thermal difusivity (α, $[cm^2/s]$), beam speed (v, [cm/s]), beam spot size (D, [cm]), density (ρ, $[g/cm^3]$**)**, and heat capacity (c_p, $[J/(kg * C]$) are utilized for the Ti-48Al-2Cr-2Nb normalized enthalpy calculation. The normalized enthalpy themal properties are referenced based on the melting temperature of Ti-48Al-2Cr-2Nb material.

Table 6. Ti-48Al-2Cr-2Nb thermal properties within the EBM process. [62,63]

Density (g/cm^3)	**Heat Capacity ($J/(kg * C)$)**	**Thermal Conductivity ($W/(cm * C)$)**	**Thermal diffusivity (cm^2/s)**	**Absorptivity of electron beam (%)**	**Melting point (C)**
4100	700	23	8.013*10-6	80	1460

Another means of expressing the energy input of the EBM process is via VED. The VED considers the average applied energy on a volume of the Ti-48Al-2Cr-2Nb material. VED is calculated from the applied process parameters (current, speed, voltage, layer thickness, and line offset) [64]. The VED calculation, as seen in Equation 5 is much simpler that the NE calculation and it is usually implemented as a common measurement of applied energy during an AM process [64].

$$VED = \frac{Voltage(kV) * Current\ (mA)}{Speed\ (^{mm}/_{s}) * Line\ offset(\mu m) * Layer\ thickness(\mu m)} \qquad \textbf{(5)}$$

Both of these energy features provide a general representation of the energy applied to melt and join each layer within the EBM process.

Another set of expressions for energy input are line energy (LE) and area energy (AE), as described below. LE refers to the calculated applied or input energy from the electron beam on a continuous melt line in the EBM system. While the AE refers to the applied energy of the electron beam on a specific area in a single layer within the EBM print. The LE equation is calculated using the (current, speed, voltage), while the AE includes the line offset as a parameter to quantify the energy effect on a specified area (current, speed, voltage, and line offset)

$$\boldsymbol{LE = \frac{Voltage(kV) * Current\ (mA)}{Speed\ (^{mm}/_{s})}} \quad \boldsymbol{AE = \frac{Voltage(kV) * Current\ (mA)}{Speed\ (^{mm}/_{s}) * Line\ offset(\mu m)}} \qquad \textbf{(6)}$$

3.2.3 Computed tomography and data visualization

X-ray Computed Tomography (CT) (Zeiss Xradia 520 Versa, ZEISS, Oberkochen, Germany) was used to capture the internal pore architecture of the experimental samples. For this analysis, all coupons printed in the EBM process were scanned at a resolution of 10µm. The resulting TXM files was roughly set at 9.8 mm diameter and 10 mm height. All the printed sample scans were cropped to a height of 8 mm, by removing cone effect, which typically occurs in CT analysis, from the top and bottom layer in the initial CT scans [65]. For phase 1 samples, a height of 6,000 microns of the measured CT data was analyzed, while phase 2 height was set at 8,000 microns for each sample. For all the data processed, a similar coordination was obtained by defining the data from the center of the scan.

An image processing software (Dragonfly Software, Object Research Systems (ORS), Montreal, Canada) was utilized as a post-processing analysis tool to quantify the pore characteristics based on the 3D imaging of each EBM-printed part. The spatial and size distribution of porosity were extracted and different types of pores were classified based on the shape, size/, and aspect ratio of each pore. For this study, an aspect ratio from a scale from 0 to 1 was utilized to define the type of pore. The two main types of porosity defect witnessed in EBM are lack of fusion (LOF) pores created due to insufficient applied energy needed to melt and fuse the layers in the EBM process, and gas porosity which are generally believed to be transferred from the powder/feedstock into the melted layers. Within this study, the LOF defects and the gas porosity defects are defined in each category based on aspect ratio < 0.7 for LOF and ≥ 0.7 for gas pores, respectively. This aspect ratio creates a demarcation between a more 'spherical' defect and an 'irregular' defect [38]. Equation 1 was utilized to quantify the relative density of each EBM printed part.

$$\boldsymbol{Relative\ Density = \frac{Voxel\ count\ of\ solid}{Voxel\ count\ of\ entire\ ROI}} \qquad \textbf{(7)}$$

The voxel count of just the pores that are identified as LOF and gas pores were extracted as well to estimate the different types of porosity using Equation 2 and Equation 3.

$$\boldsymbol{LOF\ porosity} = (\mathbf{1} - \boldsymbol{relative\ density}) * \frac{\boldsymbol{Voxel\ count\ of\ LOF}}{\boldsymbol{Voxel\ count\ of\ LOF\ and\ gas\ pores}} \quad \textbf{(8)}$$

$$\boldsymbol{gas\ porosity} = (\mathbf{1} - \boldsymbol{relative\ density}) * \frac{\boldsymbol{Voxel\ count\ of\ gas\ pores}}{\boldsymbol{Voxel\ count\ of\ LOF\ and\ gas\ pores}} \quad \textbf{(9)}$$

3.2.4 Classification categories based on porosity (or alternately bulk density) levels

To categorize the printed samples based on their quality level with respect to bulk density, we defined a 4-class threshold. Samples that fall under the "Excellent," "Good," "Poor," and "Failed/Unacceptable" ranges were identified. The criteria for each threshold class were defined based on the main factors that impact the mechanical properties of the printed samples.

- **Excellent Threshold:** Samples that fall in this range showcase optimal result (close to 100% relative density) in the as-built condition. The mechanical properties are not heavily influenced in this range. Are expected to be fully closed in HIP.
- **Good Threshold**: Samples that fall in this range are reasonably appropriate results. The defects are more prominent, however, the samples in this range are not expected to drastically affect the mechanical properties, similar to fully dense prints; expected to be mostly closed in HIP.
- **Poor Threshold:** Samples that fall in this range present poor mechanical properties in the as-built condition. Pore defects may be closed in this range with HIP, but not guaranteed.
- **Failed/Unacceptable Threshold:** Samples that fall in this range are not expected to produce good/dense parts even after HIPing due to size of potential pore defect connecting with the surface of printed samples, therefore interfering with the ability to close the defects using HIP.

The values for each threshold were derived based on previous studies conducted on Ti-alloy samples printed via EBM. EBM printed Ti-alloy samples generally produce porosity values ranging from 0.15% - 5% [34,66,67]. Various studies showcase the optimized and unoptimized sample defect results, as well as the effect of HIP in closing the pores in printed samples. Generally, samples with porosity < 0.2% are expected to be fully closed using HIP and as the porosity gets larger, the less effective HIP is in closing the pores [35,67]. In some cases, porosity can be increased due to pore connection to the exposed surface during HIP, which often occurs in prints with higher porosity levels [35]. Samples with porosity > 2% are expected to have reduced mechanical performance [35]. Based on the available

literature and the class definitions above, the thresholds for the Bulk density and bulk porosity are shown in Table 7.

Table 7. Threshold class developed for experimental study of Ti-48Al-2Cr-2Nb with PSD 45-150 µm.

Target	No. of classes	Threshold Class		
		Class	**Threshold (%)**	**Maximum tolerance (range)**
Relative density	4	**Fail**	d < 98.0	-
		Poor	98.0 < d < 99.6	1.6
		Good	99.6 < d < 99.8	0.2
		Excellent	d > 99.8	0.2
Porosity	4	**Fail**	2.0<p	-
		Poor	0.4< p < 2.0	1.6
		Good	0.2< p < 0.4	0.2
		Excellent	p < 0.2	0.2

3.3 Results and Discussion

The objective of this study is twofold. Firstly, experimental result results are analyzed and visualized to gain a deeper understanding of the process performance. Secondly, machine learning was deployed to further represent and identify the relationship between density and the EBM process, as well as to classify the resulting density outcomes into four classes representative of quality performance for EBM.

3.3.1 Powder characteristics

The powder characterization of Ti-48Al-2Cr-2Nb was conducted using various instruments. The particle size distribution results include information on the xc_min (width of the particle associated to the sieving), xFe_max (the longest ferret diameter of the particles), and x_area (the diameter of the particles when projected in an equivalent spherical volume) of the Ti-48Al-2Cr-2Nb powder. The morphology of the powder directly affects the packing density of the powder and how the powder is spread on the build platform. This in turn affects the melt pool geometry formed in the EBM process [23,68]. Therefore, the recommended PSD range of 45-150µm is utilized for this experiment. The powder feedstock utilized in this experiment is analyzed to confirm the morphology features. The

powder morphology remained consistent with the expected values without significant changes, thus, the powder feedstock is not expected to have a significant unexpected influence on the density results.

Table 8. The powder morphology of the Ti-48Al-2Cr-2Nb used in the EBM process.

Analysis	Material	D10 (µm)	D50 (µm)	D90 (µm)
Xc_min	Ti-48Al-2Cr-2Nb (45-150um)	55.15 ± 0.19	78.77 ± 0.48	127.58 ± 0.46
XFe_max	Ti-48Al-2Cr-2Nb (45-150um)	56.94 ± 0.09	80.12 ± 0.47	131.14 ± 0.42
X_area	Ti-48Al-2Cr-2Nb (45-150um)	58.91 ± 0.06	85.21 ± 0.57	139.21 ± 0.43

Based on the SEM images of the virgin powder of Ti-48Al-2Cr-2Nb as seen in Figure 28, there are some noticeable physical features of the powder. Satellite particles and porosity within the powder can influence the properties of the final printed part [23,68]. Powder porosity can increase overall sample part porosity due to the presence of Argon in the powder pores, which develops into the gas porosity formation found in EBM printed parts [35,68,69]. Also, satellite particles can affect flowability of the feedstock and create regions of powder build-up, which can influence the melting formation of the Ti-48Al-2Cr-2Nb powder in the EBM machine [68]. Based on the powder analysis, a layer thickness of 90 µm was selected as a suitable layer thickness in the EBM process.

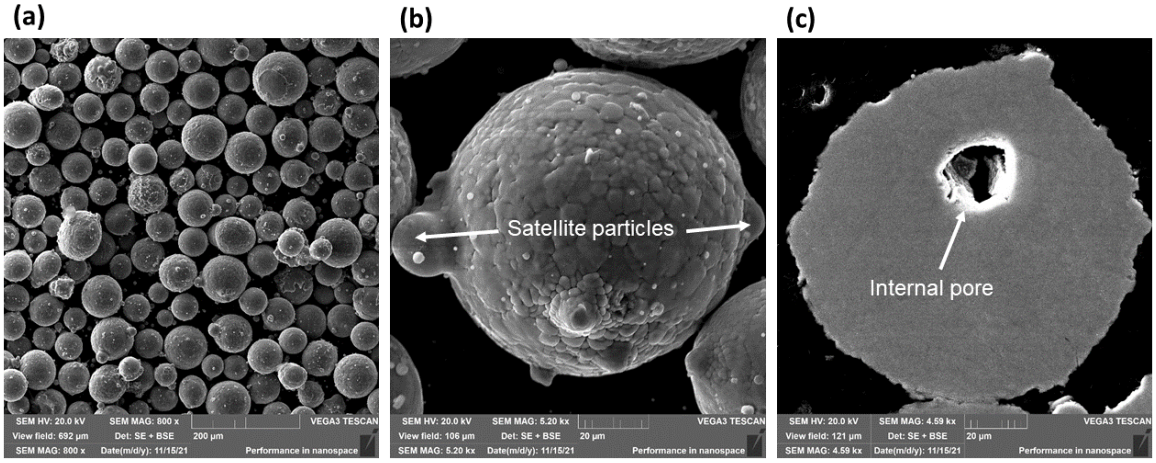


Figure 28. Scanning Electron Microscopy (SEM) representing the virgin powder state of Ti-48Al-2Cr-2Nb with a PSD of 45-150um; a) A 800x magnification image that showcases a large cluster of the powder feedstock; b) A 5000x magnification image showing the outer features of a singular powder samples within the feedstock cluster; c) a 4000x magnification image showcasing the internal structures of a singular powder sample within the feedstock cluster.

3.3.2 Experimentally-derived relationships between process parameters and bulk density

This study addresses the primary cause of pore defects formation, which is due to insufficient energy applied to melting each layer of the γ-TiAl material (LOF porosity) and material vaporization and/or porosities from internal pores within the powder (Gas porosity) [11]. The mechanical properties of the electron beam-powder bed fusion (EBM) Ti-48Al-2Cr-2Nb (γ-TiAl) samples are heavily influenced by relative density, defect size, and defect morphology. Thus, this study looks at the relationship between the defect formation and the process parameters defined for γ-TiAl samples [23,30]. The EBM-printed samples exhibit identifiable relationships between the input features and density outcomes. Figure 29 showcases examples of the resulting orthographic images of select samples printed with parameters detailed in Supplementary Table 1 to illustrate the range in pore morphology and density distribution within the experimental results. To examine the porosity and relative density, computed tomography (CT) processed data is utilized to extract quantitative information. Each identified pore has associated sphericity, size, and location properties that provide further information on the EBM printing outcomes [30]. The results of this study are presented in Figure 29, which demonstrates the orthographic projection of three different levels of density and applied energy. Among the samples, Run 2: sample 11 has the highest bulk density of 99.98% and one of the overall highest calculated normalized enthalpy/VED values. On the other hand, a low-density print with a bulk density of 96.6% is observed in Run 5: sample 16, which also has one of the overall lowest calculated normalized enthalpy/VED values. The middle-level normalized enthalpy/VED value is observed in Run 3: sample 10, which has a bulk density of 99.6%.

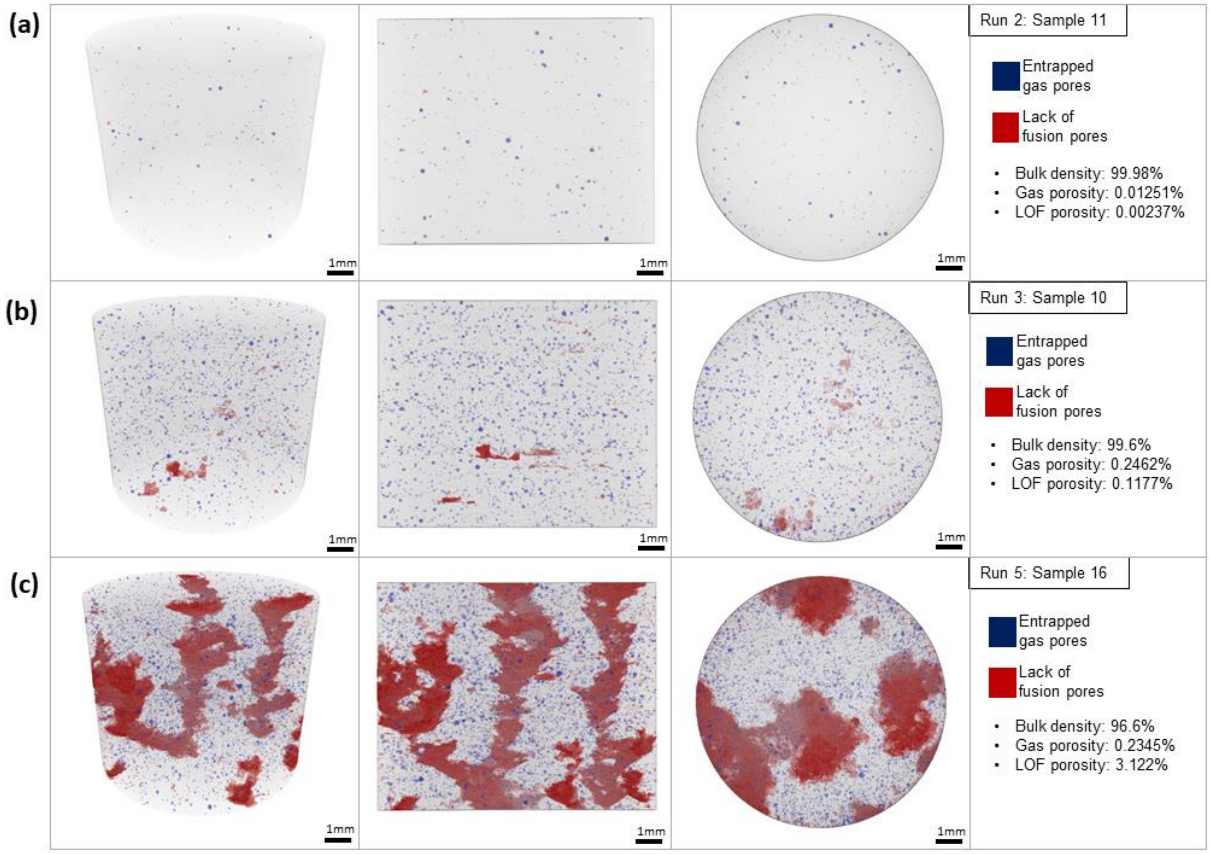


Figure 29. Isometric and orthographic minimum intensity projection view (top and side view) of the computed tomography images captured for varied density and porosity results in PSD 45-150um; (a) Very high density sample Run 2: sample 11 showcasing the gas and LOF pores ; (b) relatively medium density sample Run 3: sample 10 showcasing the gas and LOF pores; (c) low density sample Run 5: sample 16 showcasing the gas and LOF pores.

It can be observed that the presence of gas porosity is a common occurrence in the printed samples, irrespective of the input features and process parameter combinations. However, the concentration and size of these gas pores vary based on the process parameter combination. The presence of gas pores is associated with the feedstock porosity that is formed during the powder atomization process [35]. Gas porosity in parts is developed due to the processing of the Ti-48Al-2Cr-2Nb powder, which usually contains Argon [35,69]. The powder properties are predetermined by the powder synthesis process [70,71]. These porosities are transferred to the solidified layer after the electron beam melts the powder [35,38]. The heat energy directly transferred from the electron's kinetic energy allows for an environment where the gas is trapped under the melted and/or solidified metal layer [35,38]. The

spherical nature of the defects leads to the evidence of gas being present. It is believed that a comparable pore dimension is translated from the powder pore to the final print pore [34,72]. Therefore, regularly-shaped (spherical pores) porosity developed during the EBM process is assumed to result from the inclusion of gas pores in the powder material [11,38,72].

Another phenomenon speculated to affect the EBM's gas-entrapped porosity is a high energy input [73]. At a high energy input, the gas-entrapped pores potentially dissipate out of the melted layer, where enough time and energy allows the gas particles to be pushed out of the melt pool before solidification transformation [33,74]. The change in gas porosity levels as the applied energy is increased can be seen in the experiment conducted for this study. Overall, as the energy density increases, the spherical pores can diminish in quantity ever slightly.

All the pores with an aspect ratio < 0.7 are categorized as lack of fusion (LOF) porosity. There is a significant increase in the non-spherical pores as the overall applied energy on the samples increases. At an insufficient energy input in the EBM process, the powder layer is not fully melted and fused to the previous layer [67,72]. Thus, significant irregular elongated defects are formed, which are often stress concentration points under mechanical loading, resulting in premature failure of the sample [70,72]. The LOF defects appear to be the largest contributor to the porosity when the porosity increases, which shows the close relationship between the overall density and the LOF defects. Therefore, the process parameter, which determines the energy level, is expected to be the greatest contributor to the LOF and relative density.

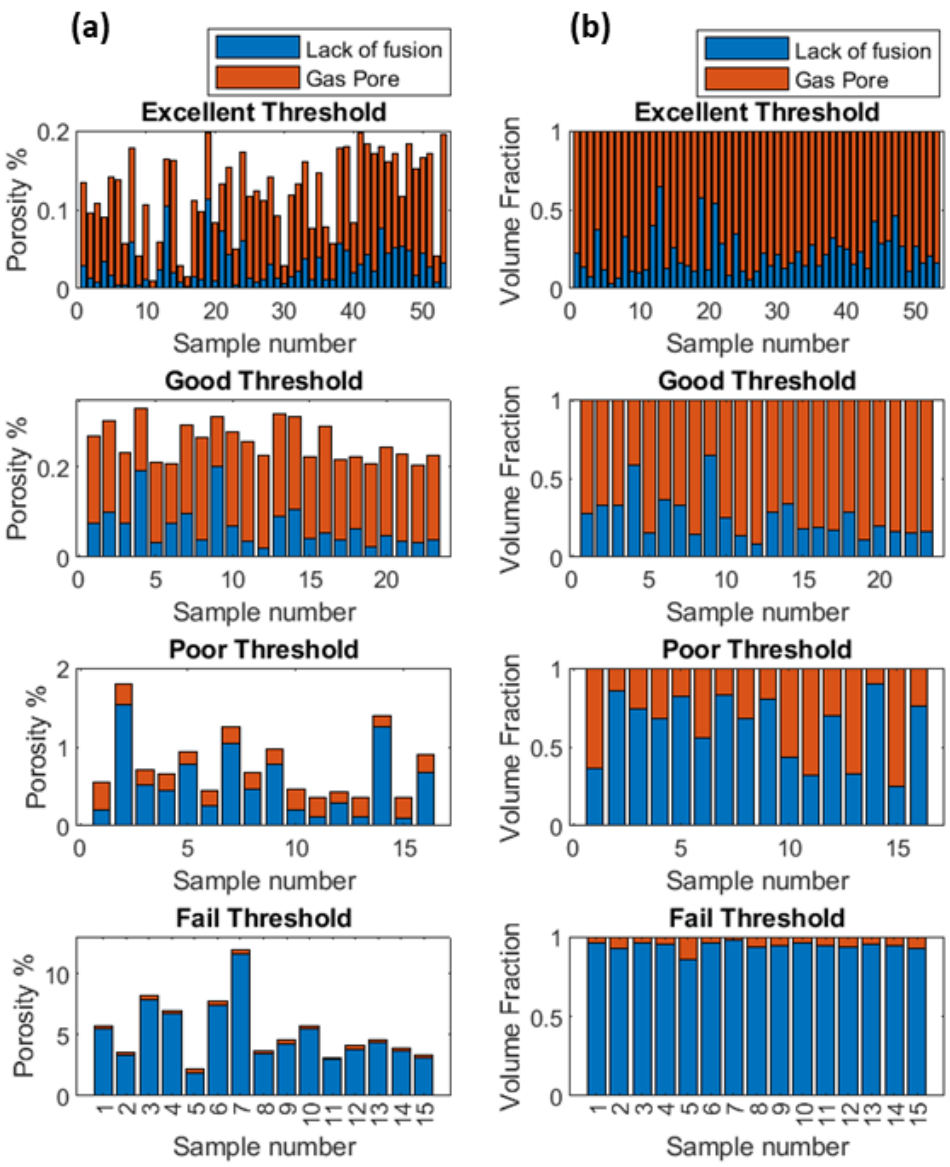


Figure 30. Showcase the derived porosity level for each experimental run results for the EBM printed parts against the sample number: (a) represents the porosity level against the sample number in each threshold bins ; (b) represents the volume fraction for each pore type against the samples number in each threshold bin.

Each sample and their corresponding porosity level were classified into the four threshold categories, as described in Section 3.2.4. Furthermore, for each sample, the LOF and Gas porosity thresholds were

deployed to visualize the proportion of the two contributing sources of porosity in each sample. The results for each performance bin (“Excellent”, “Good”, “Poor”, “Failed”) are visualized in Figure 30. Figure 30a showcases the proportion of LOF and Gas pores as porosity %, while Figure 30b presents the normalized volume fraction for each pore type – LOF and Gas pores for each sample in each class. The visualization can be used to identify trends in the type of pore defects are expected for each class. It can be seen that the predominant defects in the "Failed Threshold” and "Poor Threshold" are LOF pores, whereas the Gas pores are more dominant in the ‘Excellent Threshold’ and ‘Good Threshold’. The predominant presence of irregular-shaped pores in EBM-produced samples with low density is consistent with findings from Iebba and Tammas-Williams et al [33,38]. From these studies, elongated pores are attributed to the lack of proficient applied energy necessary to fully consolidate all the un-melted powder and granules on the EBM powder bed layers [33,38]. Generally, these types of defects are associated with potential damage in the resulting prints due to the large size of the resulting defect and the presence of stress points created from the irregular shape of the pore defect [38]. This is an important finding, as the presence of irregular-shaped pores contributes to poor mechanical performance [73].

The influence of process parameters on resulting density outcomes can be visualized using the VED and NE parameters. Since both VED and NE implicitly refer to EBM parameters and material properties respectively, observing both energy representations to understand the trend in the density and porosity offers a good insight into optimal performance ranges, where both the occurrence of LOF can be minimized and mitigation of Gas pores can be addressed.

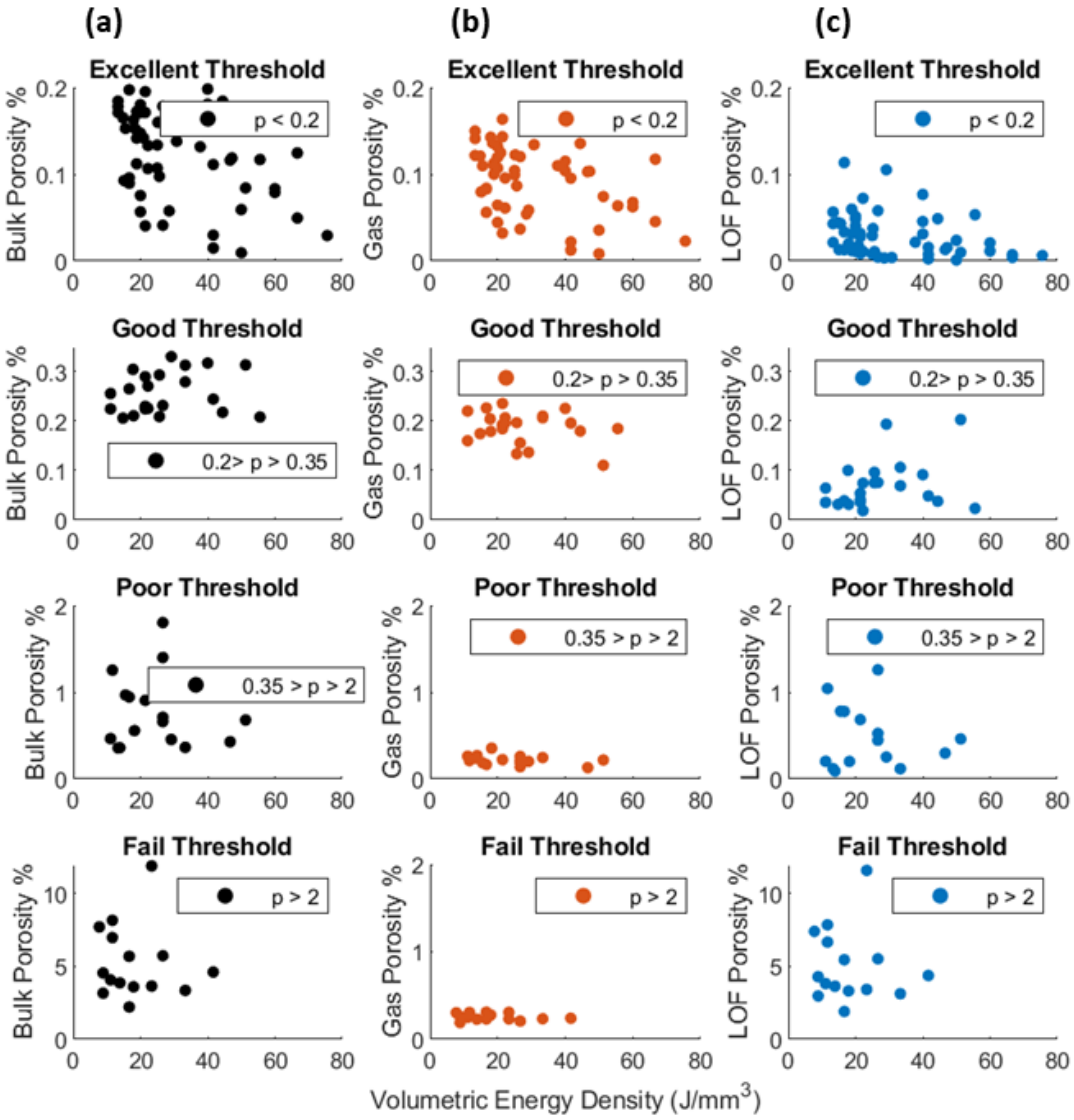


Figure 31. Showcase the different experimentally derived results for the EBM printed parts: a) represents the relationship between the volumetric energy density (VED) of every sample set and the relative density; b) represents the relationship between the volumetric energy density (VED)of every sample set and the gas porosity; c) represents the relationship between the volumetric energy density (VED) of every sample set and the Lack of Fusion porosity.

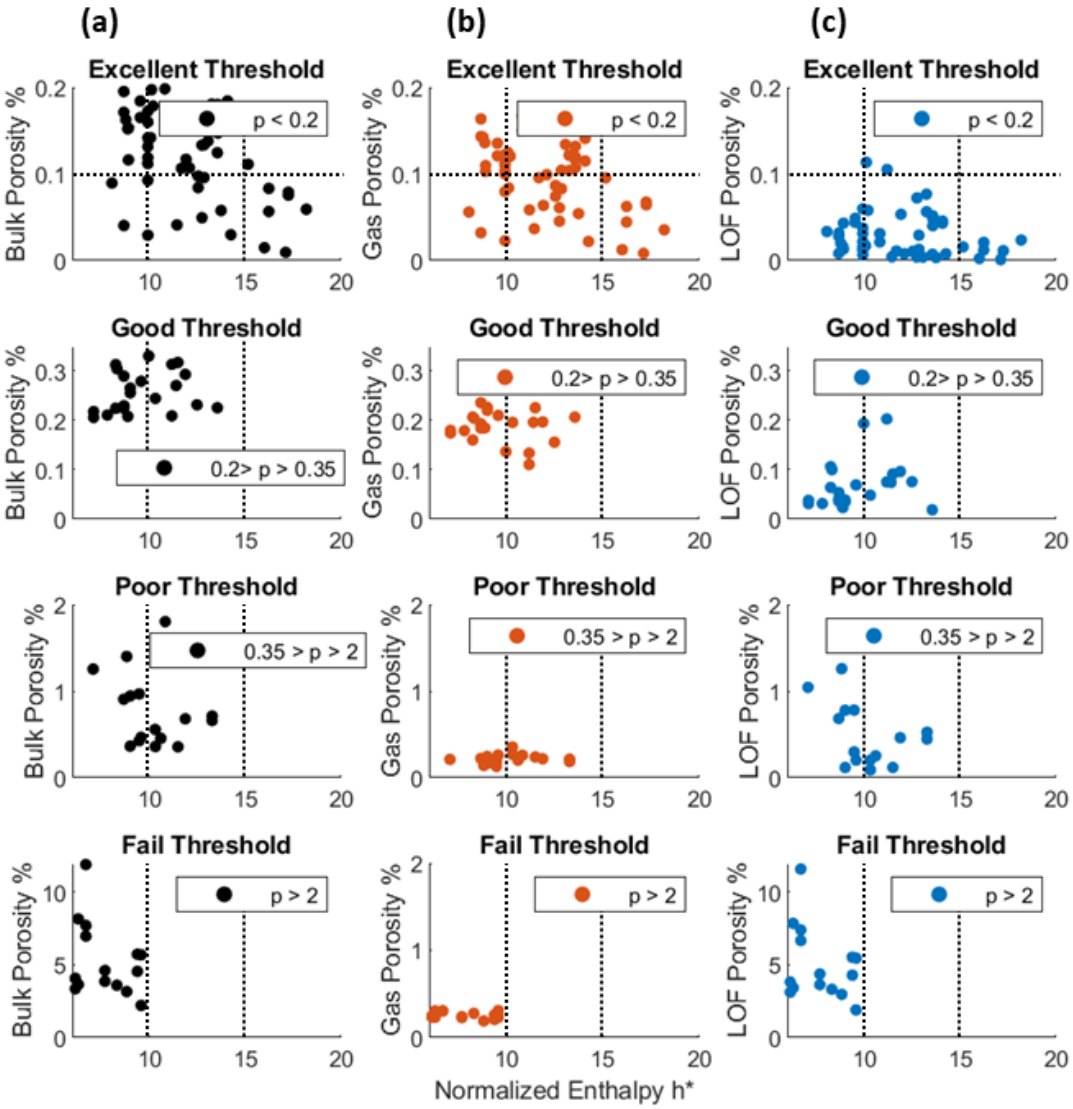


Figure 32. Showcase the different experimentally derived results for the EBM printed parts: a) represents the relationship between the normalized enthalpy of every sample set and the relative density; b) represents the relationship between the normalized enthalpy of every sample set and the gas porosity; c) represents the relationship between the normalized enthalpy of every sample set and the Lack of Fusion porosity.

Figure 31 and Figure 32 showcases an overall trend in all 4-class thresholds whereby a higher energy level produces a lower bulk porosity (negative linear trend). There is an observed pattern with the experimental data provided in this study for the porosity and the Energy representation. Figure 31a and

c. as well as Figure 32a and c show a similar strong trend between the bulk porosity and LOG porosity. This relationship is seen over the different performance classes for VED in Figure 31a, whereby the LOF porosity follows the same trend and scale of the bulk porosity values. However, when observing the Gas pores trends, the data appears to be more random, whereby the Gas porosity remains fairly consistent within a general % range for each class Nevertheless, there is a tendency for the porosity level in the Gas porosity to decrease when the energy increases for the "Excellent" and "Good" performance classes. The reduction in Gas pores is consistent with findings in literature. The development of Gas pores is often attributed to the presence of porosity in the feedstock utilized during the EBM process, and various research suggests these porosities are very challenging to remove and various studies have been unable to remove the Gas pores during the EBM printing process before heat treatment [33]. However, there have been speculations as to a potential reduction method of these pores to some extent [38,74]. Tammas-Williams et al. [38] suggests that the addition of high applied energy / heat to the powder bed provides a larger time period for solidification to fully take place, therefore allowing some of the gas bubbles to escape by breaking though the melt pool surface before the metal fully turns into solid state [38]. The escape of these gas bubbles is heavily dependent not only on the high heat applied, but also on the melt pool shape, convective and buoyancy forces needed to hold a controlled melt pool as the electron beam moves on the powder bed [38,75].

The visualization in Figure 32b appears to showcase a better correlation of NE with the density and porosity types, given that the NE takes into account both the influence of the beam process parameters and the thermal properties of the Ti-48Al-2Cr-2Nb, in contrast to VED, where the formula does not have the ability to distinguish between a low current / low speed parameter combination as compared to a high current / high speed combination resulting in similar VED values, but expected to be in different physics regimes. NE provides a better insight to the applied energy in EBM with respect to material properties. It can be seen that within the Excellent class, there is a region of NE >15 where the bulk porosity and Gas porosity are below 0.1%, with minimal contribution from LOF (<0.03%) and that Poor and Good performance overlaps at 10<NE<15, while Failed samples are all generally at NE<10. A similar delineation is difficult to discern for VED. This is an important finding, as it demonstrates the efficacy of using NE instead of VED as a descriptor in experimental DoE or data science efforts for process parameter optimization for minimizing porosity (or maximizing density) as an objective function.

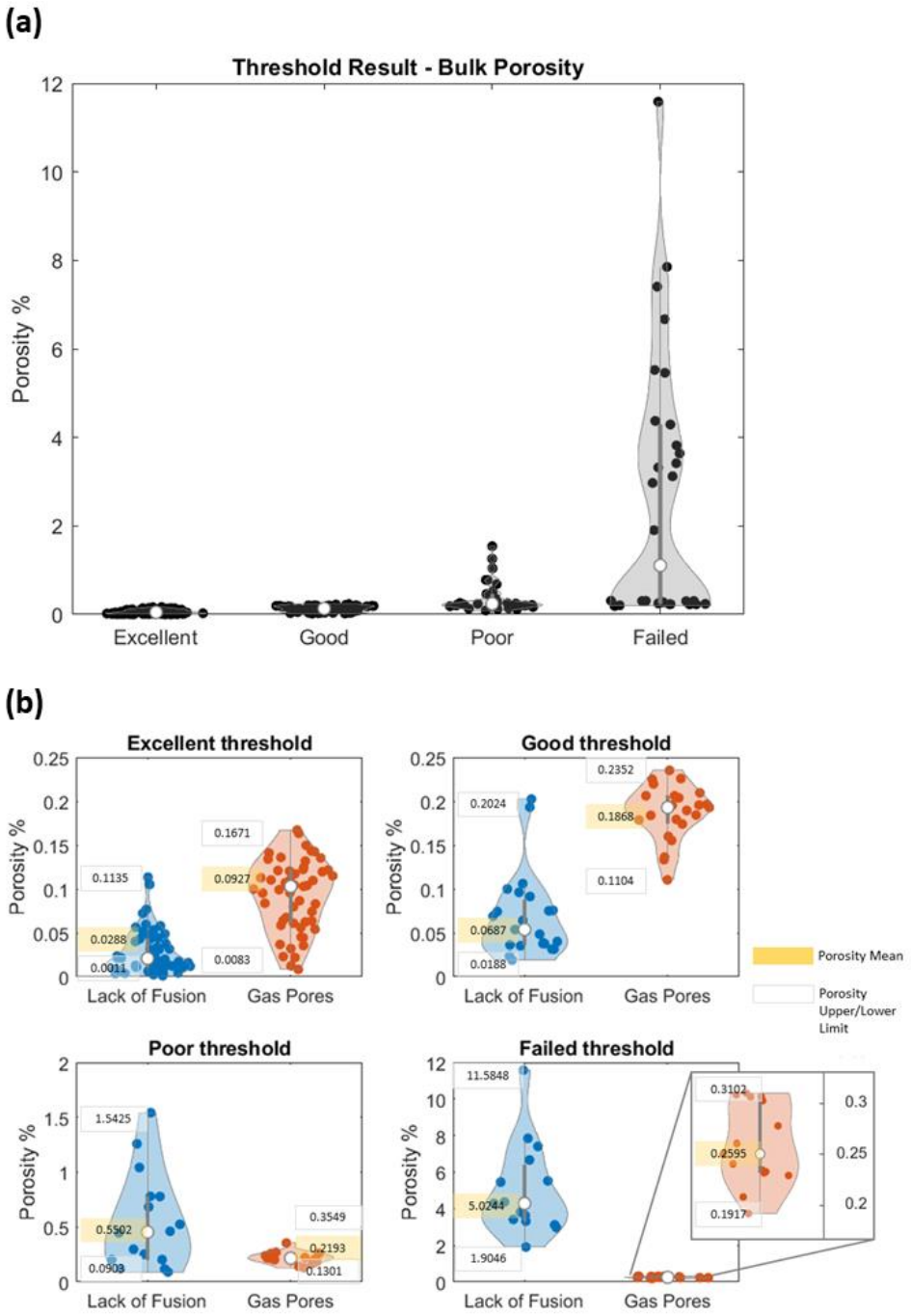


Figure 33. showcase different violin plots for each threshold class containing the experimentally derived results for the EBM printed parts: (a) represents the distribution of porosity for each threshold bins; (b) represents the distribution of porosity for each defect type (specifically LOF and Gas pores) within each defined threshold bins.

Figure 33 illustrates the distribution of porosities in each class as violin plots. Within the Excellent class, the overall bulk porosity is at the lowest in distribution; as we move from Excellent, to Good, Poor, and Failed classes, the bulk porosity levels increase sharply. In each class, the predominance of each pore defect type – LOF and Gas pores – switches. Within the Excellent class, the Gas pores as are more dominant (mean of 0.0927%) compared to lack of fusion (mean of 0.0288%); similarly, for the Good performance class, the Gas pores are more predominant than LOF. As the thresholds move to Poor, and Failed, the LOF predominance increases sharply.

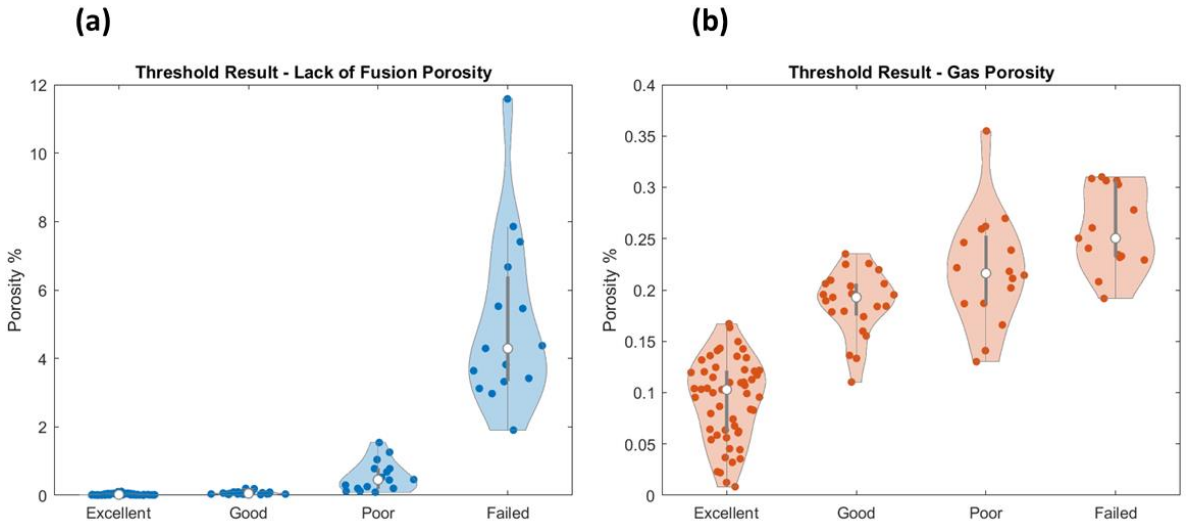


Figure 34. showcase different violin plots for each threshold class containing the experimentally derived results for the EBM-printed parts: (a) represents the distribution of the LOF porosity in each threshold bins; (b) represents the distribution of the Gas porosity in each threshold bins.

As seen in Figure 34, there is a strong increase in the LOF porosity level as the class moves from Excellent to Failed. However, the Gas pore does not reflect a similar trend. The Gas pores have a comparable porosity level regardless of threshold; there is a slight linear increase, however the porosity values overlap in each performance class, therefore the Gas porosity appears to be more random in its occurrence as compared to the LOF pores.

To increase the relative density, reducing the lack of fusion porosity by altering the process parameters to result in a higher NE will achieve a higher desired relative density. Care must be taken in not exceeding NE values that result in excessive material vaporization and over-melting that will result in poor shape fidelity and build failure (such regimes were not explored in this study. The data

visualization and analysis stage illustrates the performance of samples across the process parameter space and de-couples, for the first time in EBM, the contribution of LOF and Gas pores across different performance classes. In addition, the importance of NE as a performance discriminant across classes is shown. It is important to find regimes where LOF pores are minimized, as these pores increase the likelihood of cracks forming from the edges of the defect [3,76,77]. Another conclusion is that, in general, reducing LOF also results in a reduction of general bulk porosity. To further generalize the utility of these datasets, future work will focus on feature importance analysis and a machine learning classification framework, with a focus on bulk density and LOF classification, given that Gas pores appear consistently across all classes. This approach can help in modeling the influence from individual input features on the resulting class outcome beyond what the data visualization can achieve.

Chapter 4
Density Analysis for PSD Comparison

4.1 Introduction

The present study is focused on investigating the complex relationship between process parameters in EBM and the resulting mechanical properties of Ti-48Al-2Cr-2Nb (γ-TiAl) samples for two powder size distributions, a narrow distribution of 45-150 µm and a wide distribution of 38-180 µm. The aim is to uncover critical nuances that significantly influence relative density and defect characteristics, which are fundamental to ensuring the quality and performance of components produced through EBM. This study conducts an extensive and in-depth examination of the intricate relationship between various process parameters, powder size distributions (PSD), and overall porosity levels in Ti-48Al-2Cr-2Nb samples produced through the Electron Beam Melting (EBM) process (Arcam A2X, GE Additive, Boston, USA). Furthermore, this is the first study which looks at pore morphology, in addition to bulk density, to inform conclusions.

4.2 Materials and methods

The EBM technology was employed to manufacture the experimentally-printed samples to complete the analysis. The vacuum induction gas atomized Ti-48Al-2Cr-2Nb powder (manufactured by AP&C - A GE Additive Company) with a nominal PSD of 45-150 µm and a wider range of 38-180 µm was utilized during the printing phase of this study. This particular alloy is composed of 48 at.% Titanium, 48 at.% Aluminum, 2 at.% Niobium, and 2 at.% Chromium. To analyze the internal porosities, satellite particles, and overall morphology of the different powders provided for this study, scanning electron microscopy (SEM) (TESCAN VEGA 3, TESCAN, Brno, Czech Republic) was employed from various perspectives. Chapter 2 delves into the powder characteristics of the different powders provided throughout this study. The preheating scheme utilized to print these Ti-48Al-2Cr-2Nb parts is consistent for the experimental design in Section 3.2, where the preheating temperature was set to 970°C. While the accelerating voltage and pressure was held constant at 60V, and $2 \times 10{-}3$ mbar respectively at the beginning of the printing process in the EBM fabrication chamber. The dimension of the printed coupons analyzed in this study was set at 20mm × 20mm × 25mm. This chapter looks into detail of the comparison between the EBM-printed PSD 45-150 µm and 38-180 µm samples. The process parameter

utilized for both PSD 45-150 µm and 38-180 µm is referred to in Supplementary Table 1 and Supplementary Table 2 respectively.

To capture the internal structure of the printed samples, X-ray Computed Tomography (CT) scans from Zeiss Xradia 520 Versa (ZEISS, Oberkochen, Germany) were utilized. Additionally, to quantify the 3D imaging of the internal/bulk of each EBM-printed part, the Dragonfly Software (Object Research Systems (ORS), Montreal, Canada) was employed as an image processing software for post-processing analysis. Section 3.2.3 reports on the experimental details employed in the dragonfly post processing steps for both PSDs in this study, specifically the powder size information, density of printed parts, porosity and different types of porosity defect of the printed parts, the defined thresholds to classify the quality of the density, and the energy representation utilized to report the applied energy effect on the prints. The classification threshold is defined into 4 different thresholds (Excellent, Good, Poor, and Failed), with the main factors utilized to justify and define the value of each threshold bins are reported in Section 3.2.4. Additionally, the density, porosity, lack of fusion porosity, and gas porosity are the main features of the data that are utilized in this density analysis, with associated methodologies for analysis previously described.

Although the thresholds are defined based on the overall density (or porosity) level, the equivalent LOF and gas pores classifications are derived based on the classified porosity bins. The LOF and gas pores are defined based on the aspect ratio. Pores with aspect ratio >= 0.7 are identified as gas pores and any pores <0.7 are identified as LOF pores (Full detail of data collection and post processing designation is identified in Section 3.2.3. For this chapter, the volumetric energy density (VED) and the normalized enthalpy (NE) are the specified applied energy features utilized to interpret the relationship between the energy and the density results. Section 3.2.2 provides more detail to the derivation of the energy representation, as well as the selected EBM parameters that are included in each energy analysis. Both PSD 45-150 µm and 38-180 µm utilize the same data collection post processing for all the analysis in this chapter as is in Section 3.2 (data analysis of the relative density and porosity distribution, threshold classification, and energy representation for the EBM system).

4.3 Results and discussion

A comparative analysis was conducted on EMB-printed parts based on outcomes from two distinct powder size distributions (PSD), 45-150 µm and 38-180 µm, to bring to light specific trends in porosity and density as related to the input powders. The analysis unveiled various nuances that significantly

influence the pore properties of the final product. One notable observation is the increase in LOF porosity levels as the threshold progresses from an 'Excellent' to a 'Failed' state. This underscores the critical role that process parameters and PSD play in achieving robust fusion and structural integrity during the EBM process as seen in Figure 35.

One of the key aspects of this study involves using energy representation as an engineered feature describing process parameters. Normalized Enthalpy (NE) and Volumetric Energy Density (VED) encompass various EBM parameters, with NE encompassing material properties as well. Figure 35 and Figure 36 depict a consistent trend across all 4-class thresholds for both PSD 45-150 µm and 38-180 µm, where higher energy levels correspond to lower porosity, demonstrating a negative linear trend. The percent ratio of Gas pores to Lack of Fusion (LOF) is higher in the 'Excellent' range, but decreases significantly as the threshold progresses to the 'Failed' range in both PSD ranges.

The experimental data in this study establishes a strong relationship between bulk porosity and lack of fusion (LOF) porosity, evident in Figure 35a and c, as well as Figure 36a and c, across all the four different thresholds. The similarity in trends suggests a close correlation between the LOF porosity and the overall porosity, however, this trend is not identified between the Gas porosity and the overall porosity. Gas pore trends exhibit a randomized pattern, with porosity levels remaining within an expected range (0.1 % – 0.4 %), as the threshold changes from Excellent, Good, Poor, and Failed. Notably, there is a discernible tendency for gas porosity to decrease with increasing applied energy, highlighting the intricate relationship between energy input and defect characteristics in the EBM process for Ti-48Al-2Cr-2Nb EBM-printed samples [74]. Tammas-Williams et al. [38] states that gas pores can escape the melt pool during the EBM process melting under very specific conditions, where the gas bubble can escape from the melt pool before full solidification is established [38].

To confirm the relationship between the process parameters, energy and the density, analysis on the energy density is employed. Two types of energy representation are selected to encompass specific process parameters of the EBM process to report on the applied energy. These energy representations are VED and NE. To start off the analysis, the relationship between the energy and the porosity measured for all the experiments performed in this study is confirmed. Overall, based on Figure 35 and Figure 36, as the applied energy VED and NE increases in the EBM system, the expected overall porosity is reduced. This trend is identified in all the experimental samples regardless of the threshold. This trend is also witness in the LOF porosity in Figure 35 and Figure 36. The close trend relationship

between the overall porosity and the LOF porosity point out the clear correlation. Firstly, the VED graphs in Figure 35 does not show clear demarcation of the VED values in all the thresholds. An 'Excellent' porosity level as well as a 'Failed' porosity level can have the same VED value, which informs that this energy representation might not be the most appropriate to represent the applied energy. Normalized enthalpy provides a better representation of the relationship between the applied energy and porosity. Figure 36 appears to showcase a larger difference between the applied energy for each threshold. Most samples in the Failed category have a lower NE value, as compared to the better thresholds in Figure 36 and the Excellent threshold has a wider range of enthalpy values as compared to the other threshold.

When comparing the PSD 45-150 µm and 48-180 µm in Figure 36, there is a clearer demarcation for the 45-150 µm that is not reflected in the PSD 38-180 µm. Based on this result, potentially the clear NE demarcation in each threshold bin that identifies which samples fall in a threshold bin can change depending on the PSD. This hypothetically is due to each PSD feedstock having different features for example powder internal porosity, morphology, flowability and packing density [25]. There are multiple other influences that potentially contribute to the different pore formation of a printed part [28]. Therefore, to achieve a low porosity value, there are other factors that need to be investigated. For the wider PSD range 38-180 µm, once the input energy reaches a very high level, other EBM features potentially can have a higher influence on the density result, as compared to the process parameter identified in the NE equation. For example, the powder morphology and beam feature can cause a reduction in the resulting density due to change in flowability and packing density [25,78]. Additionally, at a wider powder range, due to the wide range of the powder particle morphology in the powder bed, the combination of the parameters can introduce instability in the printed sample. Therefore, optimization for a wider PSD needs to be addressed differently as compared to the recommended narrower PSD (45-150 µm) ranges.

To confirm the relationship between the individual process parameter, machine learning (ML) and Statistical analysis may be used to identify the effect of each process parameter can give a clearer insight to the important EBM feature when it comes to density optimization. Regardless, the comparison between PSD 45-150 µm and PSD 38-180 µm provides valuable insights into the impact of energy input on porosity levels in Ti-48Al-2Cr-2Nb samples. The preliminary and general dynamic interplay between energy input, powder size distribution, and resulting defect characteristics is identified.

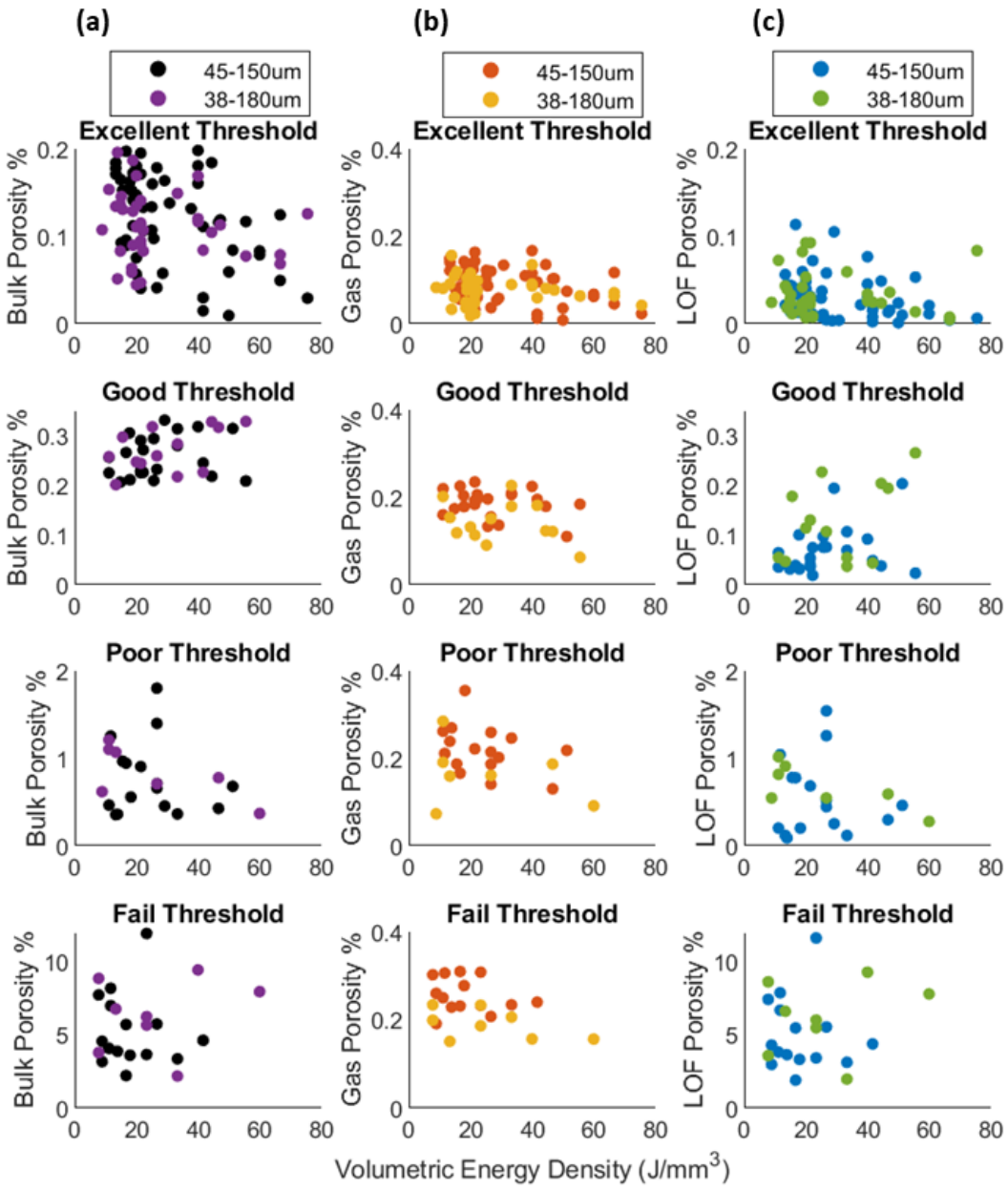


Figure 35. Showcase the different experimentally derived results for the EBM printed parts of both PSD 45-150 µm and 38-180 µm: a) represents the relationship between the volumetric energy density (VED) of every sample set and the relative density; b) represents the relationship between the volumetric energy density (VED)of every sample set and the gas porosity; c) represents the relationship between the volumetric energy density (VED) of every sample set and the Lack of Fusion porosity.

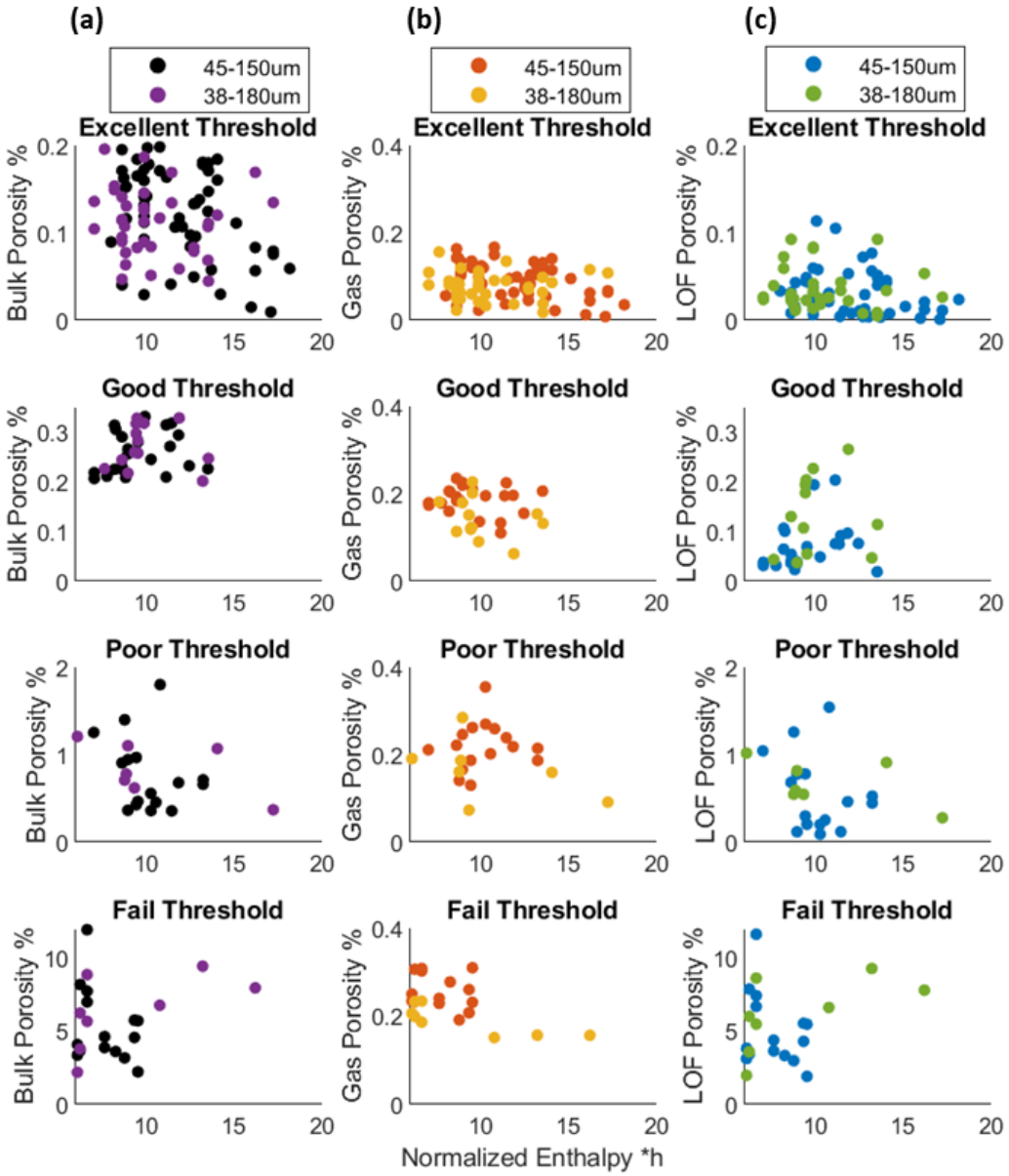


Figure 36. Showcase the different experimentally derived results for the EBM printed parts of both PSD 45-150 µm and 38-180 µm: a) represents the relationship between the normalized enthalpy of every sample set and the relative density / porosity; b) represents the relationship between the normalized enthalpy of every sample set and the gas porosity; c) represents the relationship between the normalized enthalpy of every sample set and the Lack of Fusion porosity.

Based on the 4-class thresholds defined, the data visuals (violin plots) for both PSD 45-150 µm and 38-180 µm were created in Figure 37. These visuals showcase the overall distribution of the measured porosity of PSD 45-150 µm and 38-180 µm. Based on the threshold ranking from Excellent, Good, Poor and Failed, the porosity distributions are presented. There appears to be a similar porosity for both PSD's across the threshold bins.

As thresholds shifted from 'Excellent' to 'Failed' states, bulk porosity levels for both PSD 45-150 µm and 38-180 µm consistently increased, highlighting the similar role process parameters plays in shaping the structural integrity of both PSDs. Moreover, the study discovered that PSD 45-150 µm and PSD 38-180 µm showed a striking similarity in the distribution of overall porosity, underscoring the comparable influence of PSD on the resulting bulk porosity, within the experimental process parameter windows studied. Therefore, it is important to break down the overall porosity into the LOF and Gas porosity type, to better understand other changes.

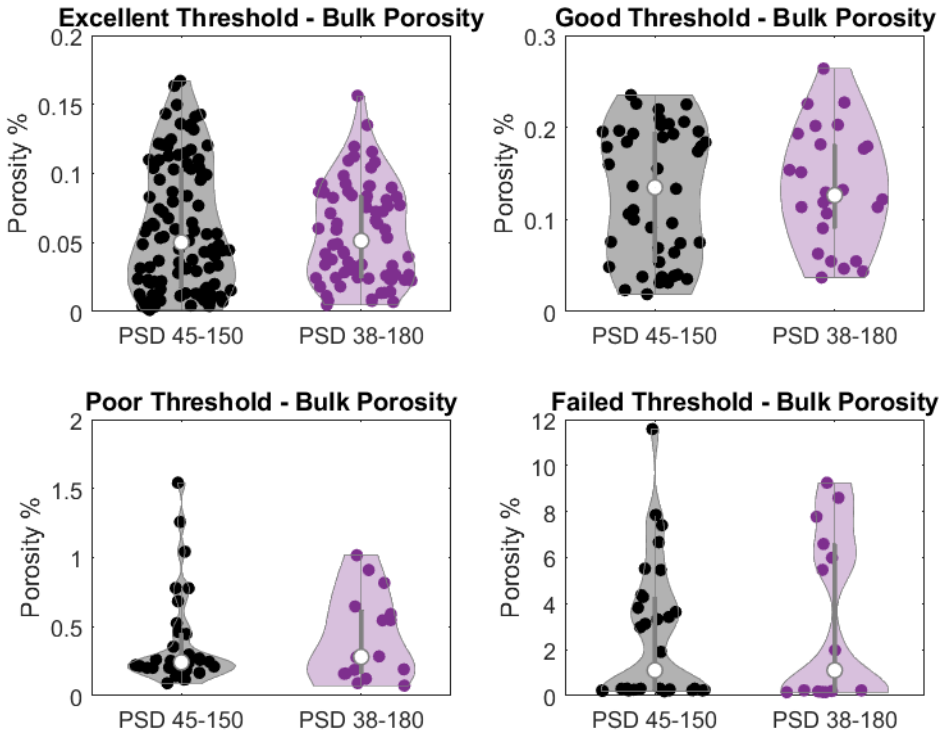


Figure 37. Showcase different violin plots for each threshold class containing the experimentally derived results for the EBM printed parts which represents the distribution of overall porosity for each threshold bins for both PSD 45-150 µm and 38-180 µm.

The distribution of porosity across the defined 4-class thresholds is utilized to evaluate the impact of PSD on overall porosity levels and found a consistent trend across both LOF and Gas porosity data. When examining specific porosity types, as seen in Figure 38, the study found intriguing differences in the distribution of gas porosity for the two PSDs. While the range of gas porosity remained similar in both PSD 45-150µm and PSD 38-180 µm, a slight increase in gas porosity was observed in PSD 45-150 µm, when going from the Excellent to the Failed class. Overall, the analysis reveals a consistent and overlapping porosity trend across the various thresholds. Interestingly, PSD 38-180 µm exhibits a slightly lower Gas porosity level compared to PSD 45-150 µm. This observation suggests that the powder feature for the wider PSD 38-180 µm range may contribute to mitigating variations in defect morphology and size, influencing the resulting porosity levels in Ti-48Al-2Cr-2Nb EBM-printed samples.

A higher percentage of powder porosity in the feedstock for PSD 38-180 µm as seen in Section 2.3.6 should theoretically present with a higher gas porosity level in PSD 38-180 µm as compared to PSD 45-150 µm. The expected trend is not seen in the data as presented in Figure 38. This discrepancy can potentially may be attributed to data scarcity. Regardless, the characterization of gas porosity, with its random distribution and substantial overlap in porosity values across thresholds, underscored the inherent challenges in predicting and managing this type of porosity. The marginally higher gas porosity in PSD 45-150 µm may signal data limitations or a potentially higher presence of LOF pores in PSD 38-180 µm that are not adequately represented as gas pores, necessitating further investigation.

In Figure 38, the LOF pore distribution for PSD 45-150 µm and 38-180 µm showcases a similar distribution regardless of the threshold levels, more so than the Gas pore distribution. Although, it appears PSD 45-150 µm presents a lower porosity limit in the distribution for all four thresholds, as compared to the PSD 38-180 µm. This trend is expected in this analysis considering PSD 45-150 µm is expected to have less LOF pore formation due to high flowability and packing density, which allows for a more consistent melt pool [25]. The difference in the gas pore distribution for the PSD 45-150 µm and the 38-180 µm widens as the porosity level increases as seen in Figure 39.

The study also showed that LOF porosity exhibited an exponential increase in porosity levels as thresholds shifted from 'Excellent' to 'Failed' as seen in Figure 39. This highlighted the intricate dependence of overall porosity levels on process parameters, underscoring the importance of incorporating maximum tolerance within the defined thresholds to ensure a comprehensive evaluation

that accommodates the exponential shift in porosity levels. Inversely, the Gas pores increase slightly as the threshold moves from ‘Excellent’ to ‘Failed’, with majority of the porosity values overlapping across the threshold bins. This trend in Figure 39 points to the random distribution of the Gas pores that has a lesser degree of influence from the applied energy as compared to the LOF pores.

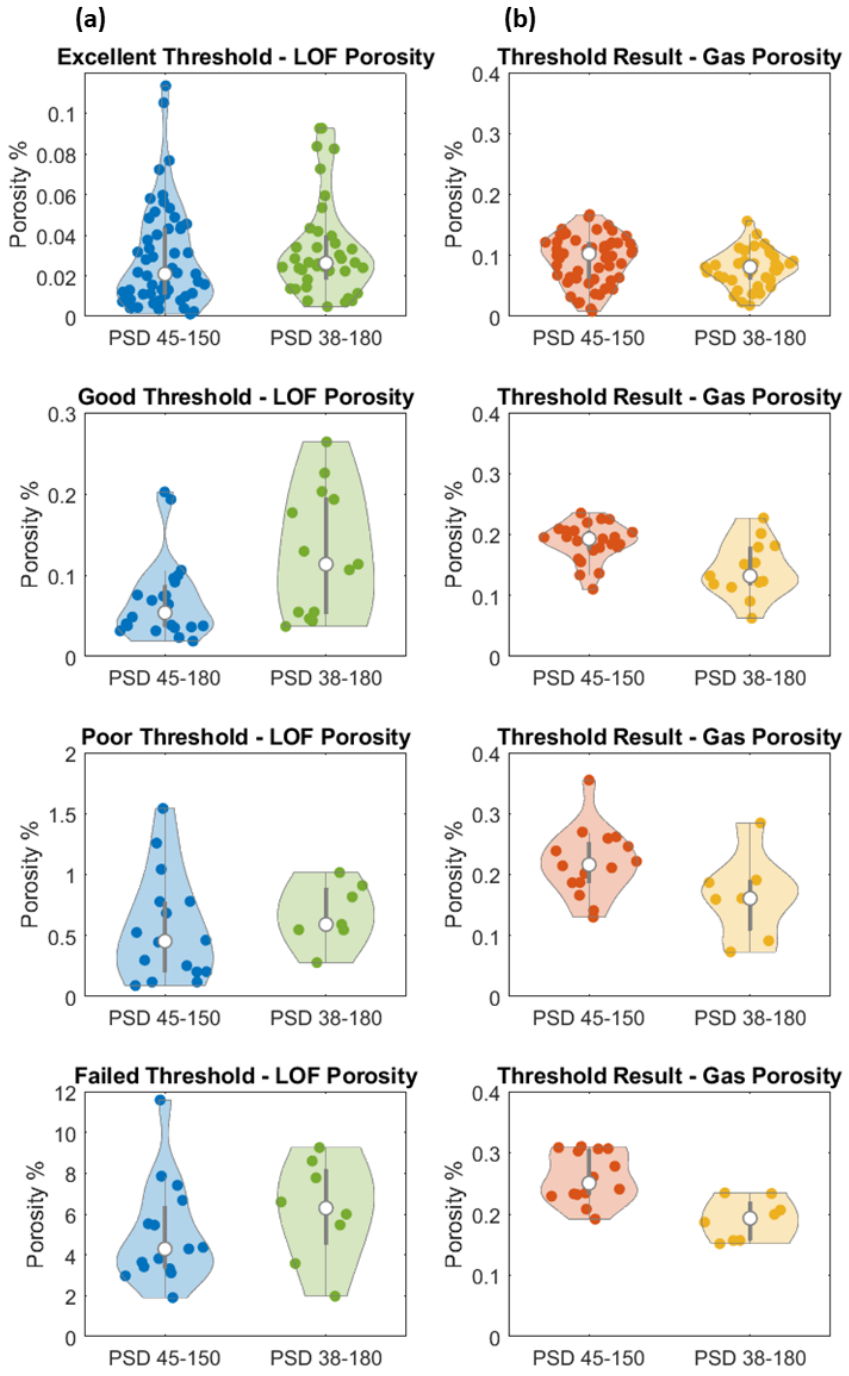


Figure 38. Showcase different violin plots for each threshold class containing the experimentally derived results for the EBM-printed parts of each threshold bin for both PSD 45-150 µm and 38-180 µm: (a) represents the distribution of the LOF porosity in each threshold bins; (b) represents the distribution of the Gas porosity in each threshold bins.

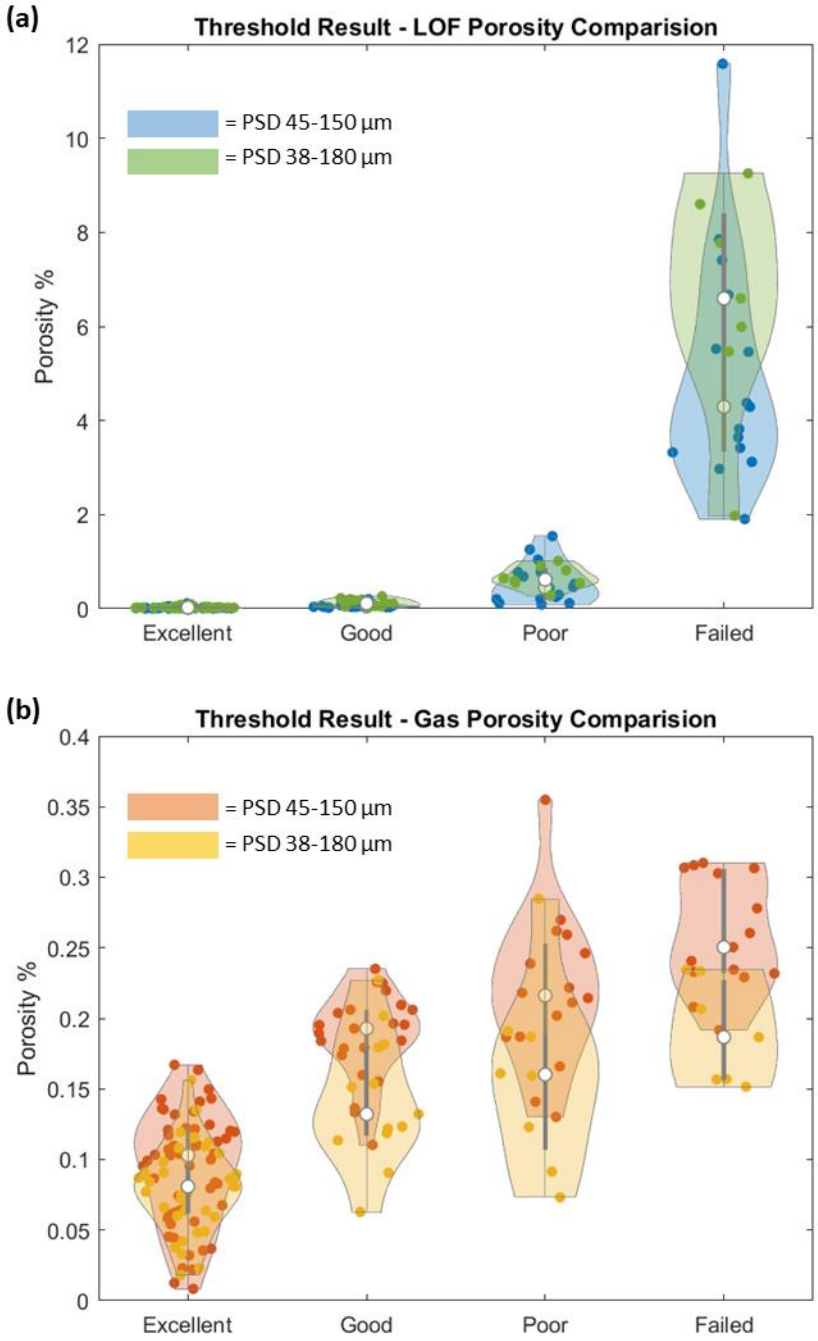


Figure 39. Showcase different violin plots for each threshold class containing the experimentally derived results for the EBM-printed parts for both PSD 45-150 µm and 38-180 µm: (a) represents the distribution of the LOF porosity in each threshold bins; (b) represents the distribution of the Gas porosity in each threshold bins.

It is crucial to delve deeper into these findings to explore how specific process parameters interact with each PSD to influence defect characteristics. For example, the energy density, scan speed, and powder layer thickness have been found to be critical parameters that determine the extent of energy applied to the powder bed [31,32]. The interaction between these parameters and powder size distribution can influence the resulting porosity levels and ultimately affect the mechanical properties of the final product [29,30].

Overall, the study suggested that PSD 38-180 µm emerged as a promising PSD range for optimization, showcasing high potential for achieving porosity levels below 0.2% [35]. This is particularly significant, as such low porosity levels can be effectively closed through Hot Isostatic Pressing (HIP), promising enhanced mechanical properties and heightened structural integrity in Ti-48Al-2Cr-2Nb samples produced through the EBM process [35,67]. Additionally, the PSD 38-180 µm can be more economically sustainable to utilize, as it utilizes a higher yield from the atomization process, without the need for further classification to narrow the PSD down to the typical 45-150 µm utilized in the EBM process. The study findings provide valuable insights into the complex relationships among process parameters, powder size distributions, and overall porosity levels and offer a path forward for optimizing the EBM process for producing Ti-48Al-2Cr-2Nb components with enhanced mechanical properties and structural integrity.

4.3.1 Statistical analysis

For this study, three regimes where defined to analyze the effect of process parameter on the resulting density for PSD 45-150 µm and 38-180 µm. The three regimes have different thresholds for the current and speed, where both variable increase as the regime moves from low, high and super-higher. Using this study, insights into the effect of current and speed can be inferred further. The statistical analysis utilizes a DOE for a full factorial design with 4 process parameter factors, 1 replicate parameter combination, and 3 medium process parameter values totaling to 19 runs under the DOE. The selected parameter range is as shown in Table 9, where the derived full factorial DOE is developed from this experimental design setup. The process parameters, designated as A (Focus Offset), B (Speed), C (Current), and D (Line Offset), are recognized as the defined experimental values in this study. To confirm the main data analysis, the statistical analysis software Minitab is utilized to establish the

relationships in the different regimes. For all statistical analysis, the Pareto chart and the Factorial plots are utilized to confirm the findings in this study.

Table 9. Experimental design for the low, high, and super-high regime.

Experimental Design	Parameter	Level of hatch process parameter		
		Low	Medium	High
Low Regime	Focus offset (mA)	0	10	20
	Beam Speed (mm/s)	1000	1500	2000
	Beam current (mA)	7	8.5	10
	Line Offset (µm)	0.1	0.2	0.3
High Regime	Focus offset (mA)	0	10	20
	Beam Speed (mm/s)	2000	2500	3000
	Beam current (mA)	12	15	18
	Line Offset (µm)	0.1	0.2	0.3
Super-High Regime	Focus offset (mA)	0	10	20
	Beam Speed (mm/s)	3000	3500	4000
	Beam current (mA)	20	22.5	25
	Line Offset (µm)	0.1	0.2	0.3

Low regime

For the low regime runs, the DOE uses parameters as shown in Table 9; the results shown in Figure 40 showcase the relationship between the 4 defined process parameters in the DOE and the performance based on the two PSDs when considering the bulk density, LOF, and gas pores as the performance criteria. The bulk density is considered in this study instead of the bulk porosity since both bulk features report the exact same pareto chart statistical analysis (considering bulk porosity and bulk density are complement of a percentage). Figure 40 is the pareto charts that represents the significant standardized effect for each parameter or combination of parameters. The Significance level for all the data is consistent at 0.05%, which when converted to standardized effect, the value is 4.30. Figure 40 a, b, and c represents the Density, total LOF pores size, and total Gas pores size relationships respectively. At the low regime, the selected process parameter has a larger effect on the Density and LOF pores for PSD 38-180 µm as compared to PSD 45-150 µm, which is expected since LOF and Density are heavily correlated according to the results in this experiment (Figure 35 and Figure 36) as well as the literature

findings. For both Density and LOF, the current and speed is identified as the highest influential process parameters. For the Gas pores, the standardized effect is significantly lower than the Density and LOF according to the reported axis in Figure 40, which is accurately represented based on the information reported by Tammas-Williams et al. [35], where the gas pores are presumed to be largely contributed from the feedstock porosity rather than from the process parameters [35]. However, based on Figure 40, the current is considered to have the highest significance effect on the Gas pores, although the combination of a lot of the other parameters influence the Gas pore to a large degree. This relationship can be assumed to be developed from the effect of a higher input energy allowing for the porosity to escape during melting before full solidification [33,74]. Therefore, the change in current at the low regime range can still influence the gas pores.

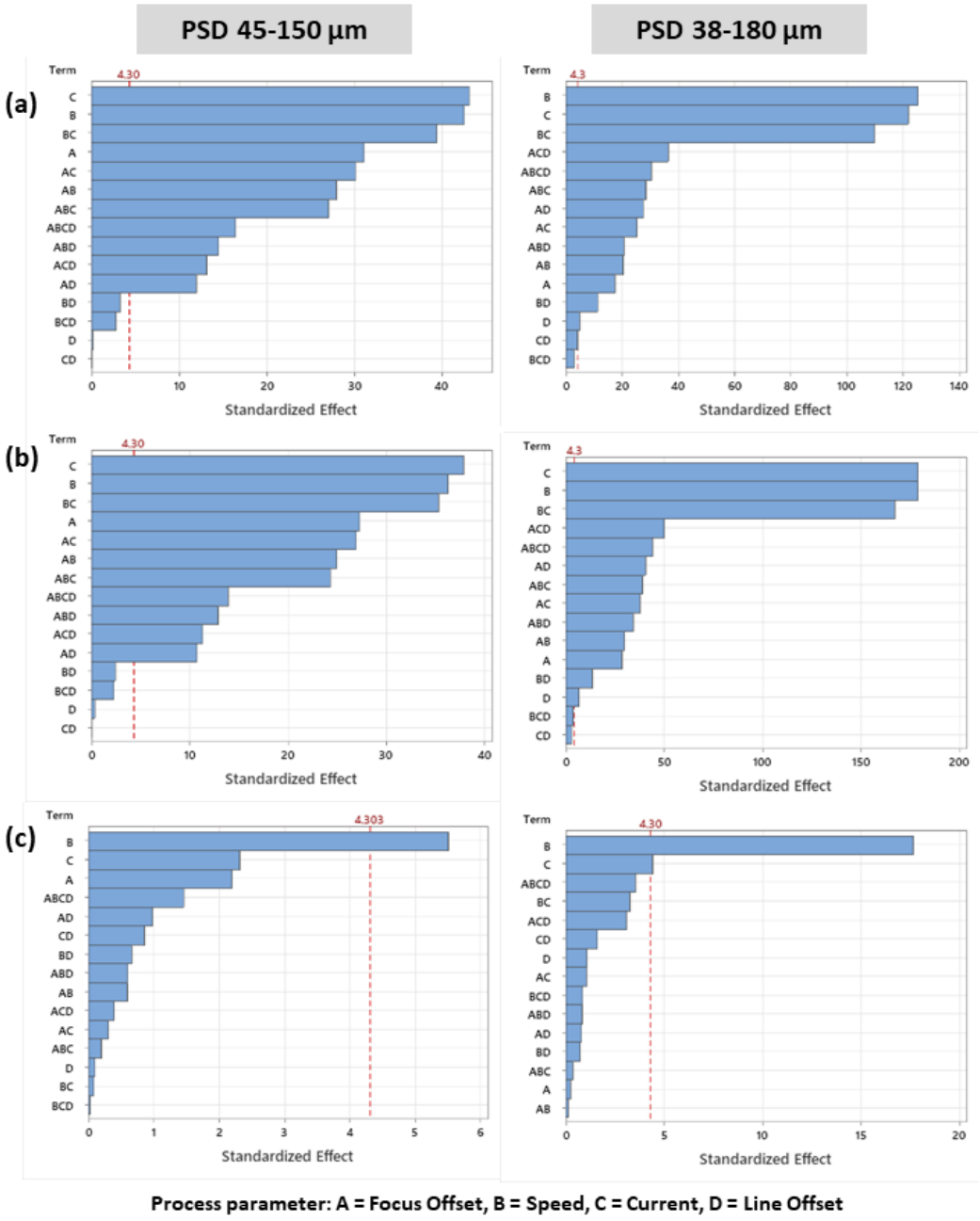


Figure 40. Pareto chart representing the relationship between the process parameters (focus offset, speed, current, and line offset) and the resulting EBM printed samples for the low regime analysis, where the significant standardized effect (4.30) or a significance level of 0.05 for both PSD 45-150 µm and 38-180 µm. a) The pareto chart for the relative density; b) The pareto chart representing the LOF porosity density; c) The pareto chart for the Gas porosity.

High regime

For the High regime runs, the DOE parameters were as shown in Table 9; the results shown in Figure 41 showcase the relationship between the pore defect outcomes and the four defined process parameters in the DOE and the PSDs utilized. Similar to the previous regime, Figure 41 displays the pareto charts that represents the significant standardized effect for each parameter or combination of parameters. The significance level for all the data is consistent at 0.05%, which when converted to standardized effect, the value is 4.30. Figure 41 a, b, and c represents the Density, total LOF pores size, and total Gas pores size relationships respectively. At the high regime, the selected process parameters have a larger effect on the Density and LOF pores for PSD 45-150 µm, when compared to PSD 38-180 µm. The standardized effect range for the parameters reduced for PSD 38-180 µm from the low regime to the high regime, while the opposite happened for PSD 45-150 µm. This means the process parameter at a lower regime for PSD 38-180 µm has a larger control on the Density and LOF porosity level developed in the EBM process. Meanwhile, for PSD 45-150 µm, the process parameters in the high regime range have a higher influence on the Density and LOF.

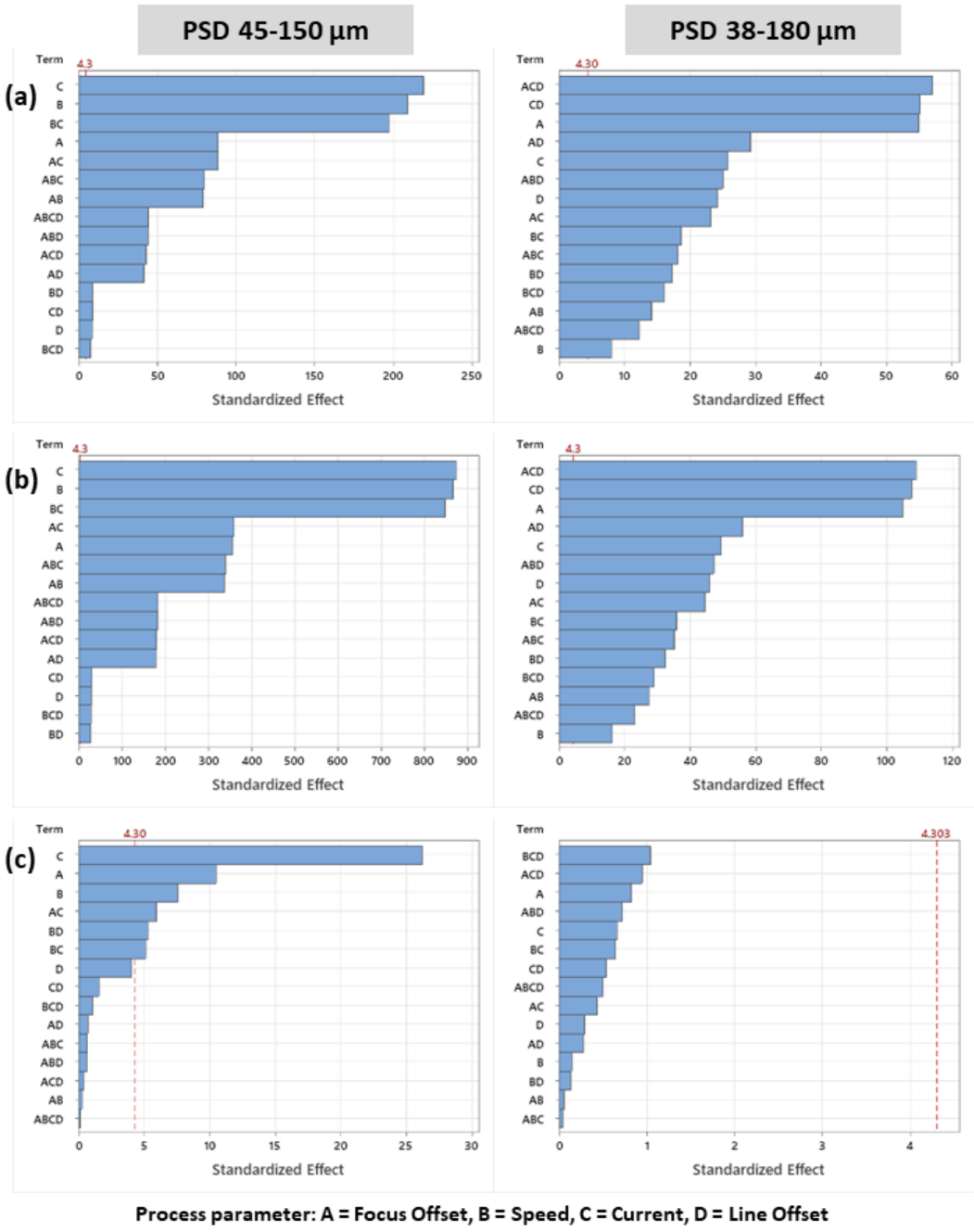


Figure 41. Pareto chart representing the relationship between the process parameters (focus offset, speed, current, and line offset) and the resulting EBM printed samples for the high regime analysis, where the significant standardized effect (4.30) or a significance level of 0.05 for both PSD 45-150 µm and 38-180 µm. a) The pareto chart for the relative density; b) The pareto chart representing the LOF porosity density; c) The pareto chart for the Gas porosity.

The LOF and Density are heavily correlated according to the results in this experiment (Figure 37 and Figure 38) as well as the literature findings. In PSD 45-150 µm, for both Density and LOF, the current and speed is identified as the highest influential process parameters. However, for PSD 38-180 µm the combination of Focus offset, Current, and Line Offset is considered the highest influencing parameter in the Density and LOF porosity. For the wider PSD range, the reduction in influence, although small, can be attributed to the difference in size range. The difference in the powder morphology creates a reduction in flowability and packing density, which can influence the powder bed, and creates discrepancies in the melt pool during the EBM melting process; as such, an increased focus offset changes the effective beam spot diameter and results in a different distribution of energy spatially, which may assist in correcting such powder spread challenges.

For the Gas pores, the standardized effect is significantly lower than the Density and LOF according to the reported axis in Figure 41, which is accurately represented due to the gas pores presumably being largely contributed from the feedstock porosity. However, based on Figure 41, various parameters are considered to have a significant enough effect on the Gas pores in PSD 45-150 µm, however, this is not the case in PSD 38-180 µm. For PSD 38-180 µm, the individual parameters are not significant in the Gas porosity change. Based on studies in Section 2.3.6, the porosity in PSD 38-180 µm powder particles is much larger in quantity as compared to the PSD 45-150 µm. Therefore, for PSD 38-180 µm, the powder feature requires an interplay between multiple process parameters to influence the gas pores.

Super-high regime

For the Super-High regime runs, the DOE uses parameters as shown in Table 9; the results shown in Figure 42 showcase the relationship between the resulting pore defect metrics and the defined process parameters in the DOE and the PSDs. Similar to the previous regime, Figure 42 displays the Pareto charts that represents the significant standardized effect for each parameter, or combination of parameters. The significance level for all the data is consistent at 0.05%, which when converted to standardized effect, the value is 4.30. Figure 42 a, b, and c represents the density, total LOF pores size, and total Gas pores size relationships respectively. At the super-high regime, similar to the high regime, the selected process parameters have a larger effect on the density and LOF pores for PSD 45-150 µm, as compared to PSD 38-180 µm. For PSD 45-150 µm, there is a slight reduction in standardized effect

of the parameters from high to super-high regime, however, the process parameters in the super-high regime range still has a high influence on the Density and LOF. Meanwhile, the standardized effect range for the parameters is the lowest for PSD 38-180 µm in the super-high regime. Based on the statistical analysis, the process parameters resulting in a super-high regime for PSD 38-180 µm have the lowest control or influence on the density and LOF porosity level developed in the EBM process.

The LOF and Density are heavily correlated according to the results in this experiment (Figure 37 and Figure 38) as well as the literature findings. In PSD 45-150 µm, the combination of ABD (Focus offset, Speed, and Line Offset) is considered the highest influencing parameter in the density and LOF porosity. AB (Focus Offset and Speed) combination is considered the most significant for the Density and LOF porosity in PSD 38-180 µm. As the regime increases, the influence of other features in the EBM process can be considered as higher inputs to the density results. For example, powder morphology, layer thickness, and other beam features could have a higher effect on the density as the current and speed increases.

For the gas pores, the super-high regime shows a different relationship between the pore features and the process parameters as compared to the previous regimes. Firstly, for PSD 45-150 µm, the significant parameter combination is the exact same as the highest effect in the Density and LOF. Therefore, at a higher regime, the overall Gas porosity has a much higher correlation to the LOF porosity to a certain degree when it comes to the process parameter combination.

Additionally, in the super-high regime PSD 45-150 µm analysis, the standardized effect is slightly lowered as compared to the high regime which showcases the highest standardized effect in the entire study. This trend identifies a potential threshold in the combination of parameter regimes, where although a high regime is preferred when identifying the process parameter effects, once the regime gets too high, other features of the EBM process appear to influence the resulting density to a higher degree.

In the super-high regime, the standardized effect for PSD 38-180 µm is significantly lower for the Density and LOF as compared to the low and high regime according to the reported axis in Figure 41. Additionally, based on the previous low and high regime trends in Figure 40 and Figure 41, various parameters are considered to have a significant enough effect on the Gas pores in PSD 45-150 µm, however, in the super-high regime, this is not the case in PSD 38-180 µm. For PSD 38-180 µm, the parameters are not significant in the Gas porosity change. This trends hypothesis a potential threshold

for the evaporation of the Gas pores right before solidification when it comes to the applied energy [33,74]. The high regime reports an overall high VED (ranging from 13.33 – 60) and an even higher NE (ranging from 9..93 – 17.25) amongst all the regimes. Meanwhile, both the low and super-high regime has a NE range 6.7 – 12.75 and 8.26 – 11.93 respectively and VED range 11.11 – 55.56 and 7.78 – 66.67 respectively. This trend is presumed to be accurately represented due to the presence of gas pores largely contributed from the feedstock porosity appearing in the super-high regime at a lower percentage [35]. The porosity in PSD 38-180 µm powder particles is significantly larger in quantity as compared to the PSD 45-150 µm based on the analysis in Section 2.3.6. Therefore, the powder feature has a larger effect on the gas pores as compared to the process parameter for PSD 38-180 µm.

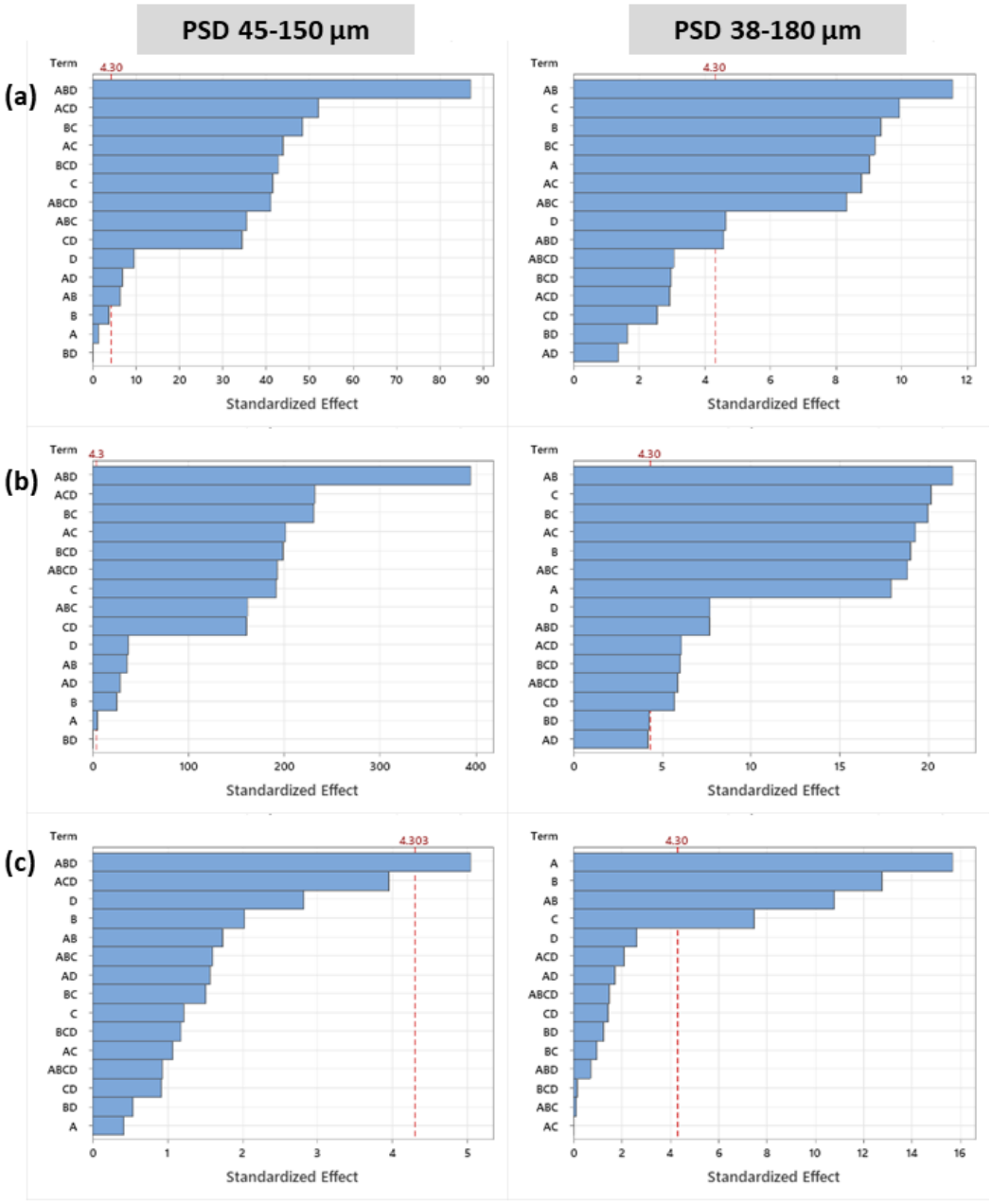


Figure 42. Pareto chart representing the relationship between the process parameters (focus offset, speed, current, and line offset) and the resulting EBM printed samples for the super-high regime analysis, where the significant standardized effect (4.30) or a significance level of 0.05 for both PSD 45-150 µm and 38-180 µm. a) The pareto chart for the relative density; b) The pareto chart representing the LOF porosity density; c) The pareto chart for the Gas porosity.

4.3.2 Further analysis

Based on the analysis of the Pareto charts, for PSD 38-180 µm, the range of parameters that heavily influence the density results is in the low regime range. For PSD 45-150 µm, the optimal parameter range that can control the resulting density is around the high regime. However, this relationship does not directly inform that these regimes identified are the ranges expected to produces the best density result, since there are other features that can affect the results. The analysis does provide the range that is potentially more reliable and consistent in achieving a specified density results when using the defined parameters in this study (focus offset, speed, current, and line offset) as the driving features for density analysis.

As seen in Figure 43 and Figure 44, the regime with the most consistent average density across the experimental designs actually falls in the super-high regime. As the regime moves from low to high, there is less influence from the process parameter in changing the density results. PSD 45-150 µm predicts a lower density for the super-high regime, however, achieving a very high density is possible in the other two regimes (low and high regime) depending on the process parameter combination. However, PSD 38-180 µm predicts a higher density across the experiment for the super-high regime, and the other two regimes depict a wider variety in the resulting density values.

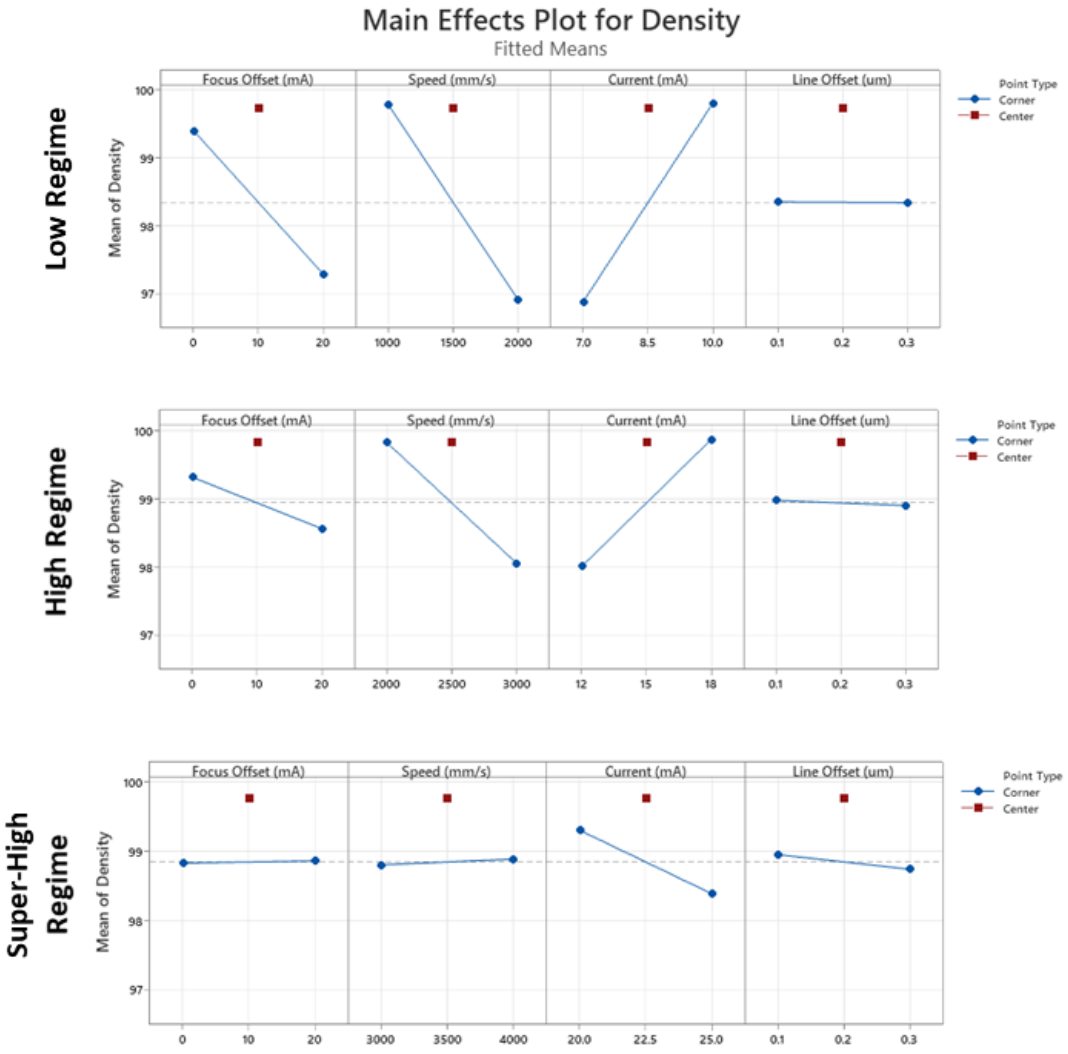


Figure 43. The main effect plots for the relative density in the low, high, and super-high regime for PSD 45-150 µm.

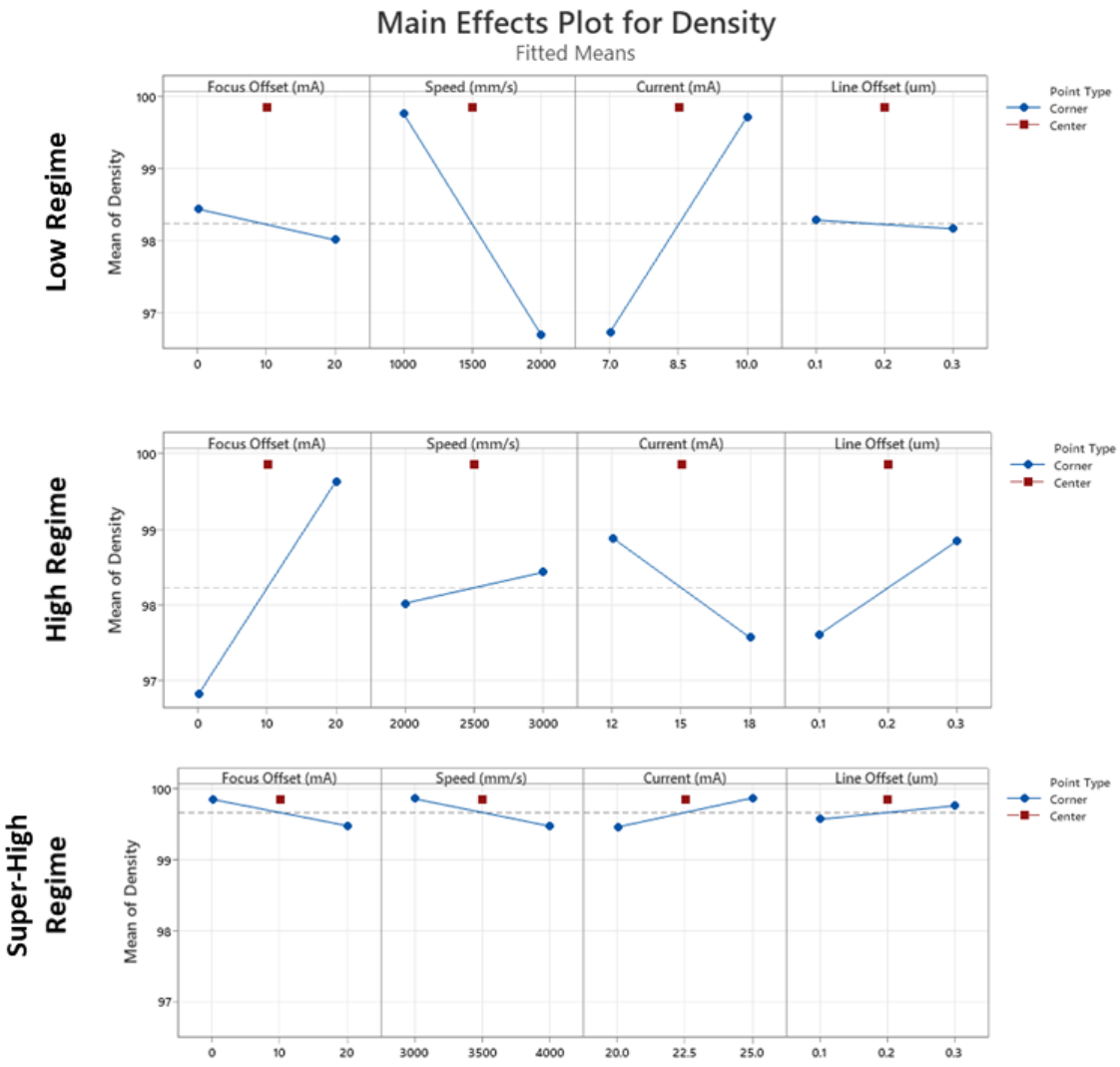


Figure 44. The main effect plots for the relative density in the low, high, and super-high regime for PSD 38-180 µm.

Response optimizer

The Response Optimizer is a sophisticated tool that adds value to the analysis by identifying the best combinations of input variable or process parameter settings in the EBM process which provides the best surface roughness feature values also improving specific responses. In this particular case, the goal is to simultaneously forecast the maximum bulk density and minimize the LOF pores. The gas pores are not included in this optimizer due to the random nature of the gas pore formation.

Minitab software uses advanced techniques to predict responses and pinpoint the optimal parameter settings required to achieve these desired outcomes, based on the bounds of the original experiment (low regime, high regime and super-high regime). Table 10 reports the process parameter and forecasted maximum density for each regime in this study.

Table 10. The forecasted optimized density and LOF pore voxel count for the low regime, high regime, and super-high regime.

	Experimental Design	Focus Offset	Speed	Current	Line Offset	Bulk Density %	LOF (voxel count)
PSD 45-150 µm	**Low Regime**	0	1000	10	0.1	99.951	24935
	High Regime	20	2000	18	0.3	99.9433	72832
	Super-High Regime	0	3000	25	0.1	99.8831	277541
PSD 38-180 µm	**Low Regime**	20	1000	10	0.1	99.9314	29463
	High Regime	0	3000	12	0.3	99.893	123661
	Super-High Regime	0	4000	25	0.3	99.9486	104988

Based on the resulting Density and LOF pore voxel count values and their corresponding process parameters, the trend across the experiment is identified. The overall trend for the process parameter for PSD 45-150 µm across all the regime is to have a high applied energy (slow speed and high current) for the defined ranges of all the parameters specified (Focus offset, speed, current, and line offset). However, the recommended input process parameter is not consistent in the applied energy recommendation, for example low regime recommends slow speed and high current, high regime recommends high speed and low current, and the super-high regime recommends high speed and high current. This parameter combination alludes to the hypothesis that the higher PSD powder feedstock has other parameters like the powder features (morphology, flowability, spreading behavior) that influence the density result to a larger degree than the process parameter. Table 11 showcases the applied energy representation for the selected optimized process parameters.

Table 11. The energy representation for the VED and NE for the forecasted optimized process parameter reported for each PSD and experimental regime.

	Experimental Design	Volumetric Energy Density (J/mm^3)	Normalized Enthalpy
PSD 45-150 µm	**Low Regime**	66.666667	12.753302
	High Regime	20	17.25035
	Super-High Regime	55.555556	11.925083
PSD 38-180 µm	**Low Regime**	66.666667	13.553155
	High Regime	8.8888889	8.8357469
	Super-High Regime	13.888889	10.327425

Chapter 5
Surface Roughness Analysis

5.1 Introduction

This study aims to deploy a statistical design of experiments approach to establish the relationship between process inputs such as powder properties (powder size distribution) and process parameters (speed, current, focus offset, number of contours, and layer thickness), and the resulting surface quality outcomes (SA, SPC, STR). Various hypotheses were tested to identify the relationship between the surface roughness and the EBM process inputs. This structured experimental investigation, provides the basis for understanding trends towards surface roughness optimization for different powder size distributions.

5.2 Materials and methods

This study was conducted by experimentally printing 114 samples via EBM (Arcam A2X, GE Additive, Boston, USA), produced using Ti-48Al-2Cr-2Nb powder particles. The contour printing parameters were varied to conduct the study and optimization, while the bulk (core) printing parameters were kept constant to reduce data inference and bias caused by the core printing conditions. Out of the 114 cubic samples printed, half of the samples were printed using the 45-150 µm PSD and the other 38-180 µm, where the printing conditions were identical for each powder batch. Details on powder properties for these two powder material systems are described in Section 2.3. Of note, the powder size distribution and sphericity are of relevance to the discussions captured in this study. The printing conditions defined for this study were developed using a statistical design of experiment (DOE) approach via factorial design. A factorial design allows for the study of effects of several factors or process parameters on a response. When conducting an experiment, varying the levels of all the process parameters or factors allows for the detailed study of interactions between the parameters.

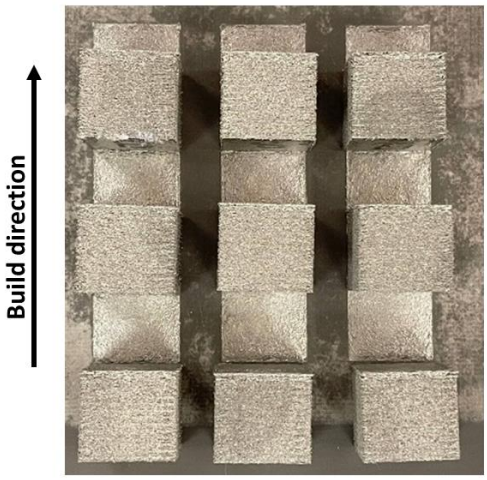


Figure 45. Image of the side surface for the Ti-48Al-2Cr-2Nb EBM-printed samples in this experiment.

Surface roughness is one of the part quality outcomes that is dependent on the EBM parameters selected at the periphery of the sample. The process parameters that are varied in this study, for each of the powders, are the focus offset, number of contours, contour scanning speed, and the contour beam current. This study looks to observe the extent of influence that different combinations of parameters has on the side surface roughness as seen in Figure 45, therefore three factorial designs were created based on different hypotheses. The first set of runs was designed based on a commonly prescribed range of parameters, were the aim was to observe the overall effect the selection of parameter values has on the surface roughness. The second run considered the hypothesis that a smaller layer thickness improves the quality of the surface roughness response. In the second run, the process parameters were kept as identical to the first run, while the layer thickness was changed to 70 µm. The third run considered a hypothesis to observe the effect of a sharper and slower electron beam on the surface roughness parameters. The beam current was increased, the focus offset and the beam speed were reduced in comparison to the first and second run to achieve the slower and faster electron beam feature. As for the layer thickness, the value was increased back to the base run 1 value of 90 µm to keep a consistent analysis and reduce other confounding factors when defining the relationship of other process parameters like the current, speed, focus offset and number of contours).

The three experimental runs were identical for both 45-150 µm and 38-180 µm design and all the parameters applied to the surface for each experimental run are shown in Table 12 below. The core

parameters are focus offset, current, layer thickness, speed, and number of contours. The preheating theme was set prior to the printing process. Before printing the samples, the first layer of powder and the build plate were preheated to 970°C, the accelerating voltage was set to 60V, and the fabrication chamber pressure reached 2 × 10−3 mbar. The study focused on surface roughness of vertical surfaces; as such, cuboid samples of dimensions 20 mm x 20mm x 25 mm were manufactured using the process parameters described.

Table 12. Identical experimental design for both PSD 45-150 µm and PSD 38-180 µm in this study.

Experimental Design	Parameter	Level of contour parameter			Layer Thickness (µm)
		Low	Medium	High	
Run 1 – Base Experiment	Beam current (mA)	4	6	8	90
	Focus offset (mA)	5	10	20	
	Beam Velocity (mm/s)	200	450	700	
	Number of contours	1	2	4	
Run 2 – Layer Thickness Experiment	Beam current (mA)	4	6	8	70
	Focus offset (mA)	5	10	20	
	Beam Velocity (mm/s)	200	450	700	
	Number of contours	1	2	4	
Run 3 – Slower Sharper Experiment	Beam current (mA)	5	7.5	10	90
	focus offset (mA)	0	5	10	
	Beam Velocity (mm/s)	200	300	400	
	Number of contours	1	2	3	

5.2.1 Sample characterization methodologies

All the samples printed in this study were cleaned post-EBM printing to remove as much loose powder from the surface. The cleaning process was applied for all the samples to maintain consistent surface results. Firstly, the coupons were air blasted in a powder recovery system (ArcamEBM, GE Additive) and lightly brushed, followed sonication in water for 30 minutes. The samples were then analyzed to complete the data collection. To analyze the surface topology, surface roughness was measured for each sample using a profilometer (Keyence, VK-X250). Data was collected from two sides of the cuboid-shaped samples with the scanning surface area approximately 2mm by 2mm, at a resolution of 10X with a z-pitch of 2 µm. To achieve the specified scan size a stitch measurement was done to enlarge

the surface area of interest. The side surface is the area of interest in this study as seen in Figure 46. The front and left side of each sample were analyzed using the profilometer, which the orientation (left, front, right and back) was defined based on the position of each sample in the EBM printing chamber. The side surface closest to the from of the chamber entrance was defined as the front, and all the other orientation was dependent on this alignment. Every profilometry scan was set at an approximate midpoint of the intended surface. Additionally, the top surface measurements were taken but is out of scope for this comparison study.

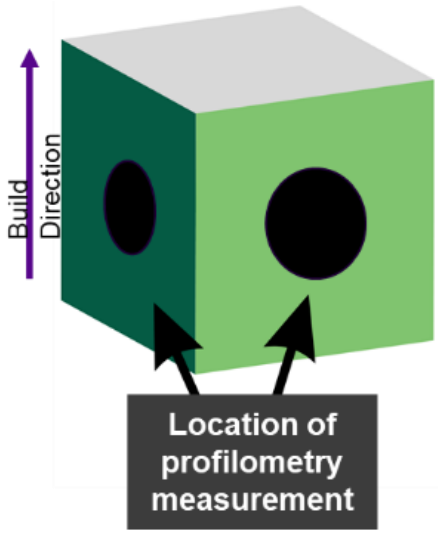


Figure 46. Schematic of printed samples and the surface roughness scanning location.

The profilometer was used to measure the topology structure of all the samples and the compiles various information on the surface. There are many features and categories that classify the surface topology, such as the height, special, hybrid, functional and feature parameters. Each of these categories have a list of parameters that represent each category. For this study, three parameters are selected to identify and represent the surface roughness results. These parameters are aspect mean height (SA) categorized under the height parameter, which focuses on the displacement of the measured surface. Followed by the texture aspect ratio (STR) categorized under the spatial parameter, which reports on the direction of the peaks or wavelength direction on the surface plane. And lastly, arithmetic mean peak curvature (SPC) categorized under the feature parameter, which represents the segmented area different from the scale-limited surface that focuses on the features of the peaks and valleys.

Arithmetic mean height (SA): SA a height parameter that is an absolute value representing the mean height of the measured surface area and is often defined as an extension of the RA measurement[79,80]. In this case RA refers to the arithmetical mean height of a line. During the profilometry scan, the average height of all the peaks and valleys are compiled and averaged out to represent the SA value. Figure 47 showcases an example of the calculation for the SA. Equation 10) represent the SA calculation where A represents the number of peaks and valleys, while the integral calculates the height based on the x-y-z coordinate system. For this study, a smaller SA value represents a better and more desirable quality surface for post processing and potentially better mechanical properties

$$\boldsymbol{SA} = \frac{\mathbf{1}}{\boldsymbol{A}} \iint_{\boldsymbol{A}} |\boldsymbol{Z}(\boldsymbol{x}, \boldsymbol{y})| \boldsymbol{dx\ dy} \text{ [80]} \qquad \textbf{(10)}$$

Texture aspect ratio (STR): STR is a scale measure of uniformity of surface texture with values ranging from 0-1 [80]. Values closer to 0 represents a more uniform/repeated surface, which can be interpreted as effects predominantly stemming from layering effects; these features can lead to reduced failure life and cracking. A higher STR value closer to 1 represents a more random distribution of surface peaks be interpreted as more stochastic powder adherence effects and are often more desirable due to a reduced chance of cracking incident formed with a more randomly patterned surface. Equation 11 and 12) indicates how to calculate the STR based on the surface spatial values.

$$\boldsymbol{STR} = \frac{\min\limits_{t_x, ty \in R} \sqrt{t_x^2 + t_y^2}}{\max\limits_{t_x, ty \in R} \sqrt{t_x^2 + t_y^2}} \quad \boldsymbol{where} \quad \begin{matrix} \boldsymbol{R} = \{(\boldsymbol{t_x}, \boldsymbol{t_y}) : \boldsymbol{f_{ACF}}(\boldsymbol{t_x}, \boldsymbol{t_y}) \leq \boldsymbol{s}\} \\ \boldsymbol{Q} = \{(\boldsymbol{t_x}, \boldsymbol{t_y}) : \boldsymbol{f_{ACF}}(\boldsymbol{t_x}, \boldsymbol{t_y}) \geq \boldsymbol{s\ and}\ **\} \end{matrix} \text{ [80]} \qquad \textbf{(11)}$$

** is the property where $f_{ACF} \geq s$ connects with (t_x, t_y) on a straight line to the origin.

$$\boldsymbol{f_{ACF}}(\boldsymbol{t_x}, \boldsymbol{t_y}) = \frac{\iint_A \boldsymbol{z(x,y) z(x - t_x, y - t_y)\ dx\ dy}}{\iint_A \boldsymbol{z(x,y) z(x,y)\ dx\ dy}} \text{ [80]} \qquad \textbf{(12)}$$

Arithmetic mean peak curvature (SPC): SPC represents the arithmetic mean of the principal curvature of the peaks on the surface [79]. A larger SPC value represents a wider surface peak and is usually not the preferred, as it increases the overall dimensional deviation of the components [79,80]. Equation 13) defines the equation needed to calculate SPC, where the dimensions and locations of each point in the measured surface is defined by the x-y-z coordinate.

$$\boldsymbol{SPC} = -\frac{\mathbf{1}}{\mathbf{2}} \frac{\mathbf{1}}{\boldsymbol{n}} \sum_{\boldsymbol{k}=\mathbf{1}}^{\boldsymbol{n}} \left(\frac{\boldsymbol{\partial^2 Z(x,y)}}{\boldsymbol{\partial x^2}} + \frac{\boldsymbol{\partial^2 Z(x,y)}}{\boldsymbol{\partial y^2}} \right) \text{ [79,80]} \qquad \textbf{(13)}$$

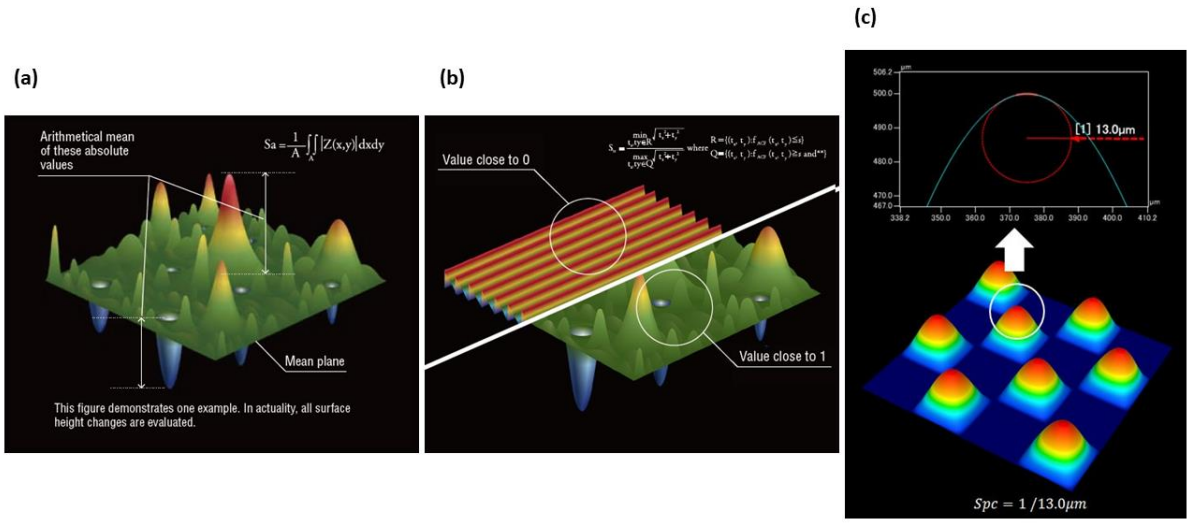


Figure 47. Schematic images of the three surface roughness parameters and their derived calculation; a) SA; b) STR; c) SPC. [80]

5.3 Results and discussion

The surface roughness analysis is conducted to identify the effect of varying process parameters and powder features like PSD on the resulting surface roughness parameter (SA, STR, and SPC).

5.3.1 Powder characteristics

The powder size distribution plot and the powder sphericity for the two powder types is captured in Figure 48 a and b respectively. These datasets illustrate the maximum range of SA and SPC expected as a contribution of direct powder particle adherence. The D10, D50 and D90 of the powders are as seen in table 2, where SA values reported to be below the D50 shows a relatively good result in regard to the PSD. If the SA values is below D10, the surface quality is said to be optimized to a really high quality and the reported SA is seen as an excellent result. Additionally, the effect of the PSD D10, D50, and D90 can inform on the formation of the peaks for the SPC analysis in this study.

Table 13. The specific powder size of the PSD 45-150 µm and 38-180 µm for D10, D50 and D90.

PSD	D10 (µm)	D50 (µm)	D90 (µm)
PSD 45-150 µm	56.94	80.12	131.14
PSD 38-180 µm	46.34	81.17	161.68

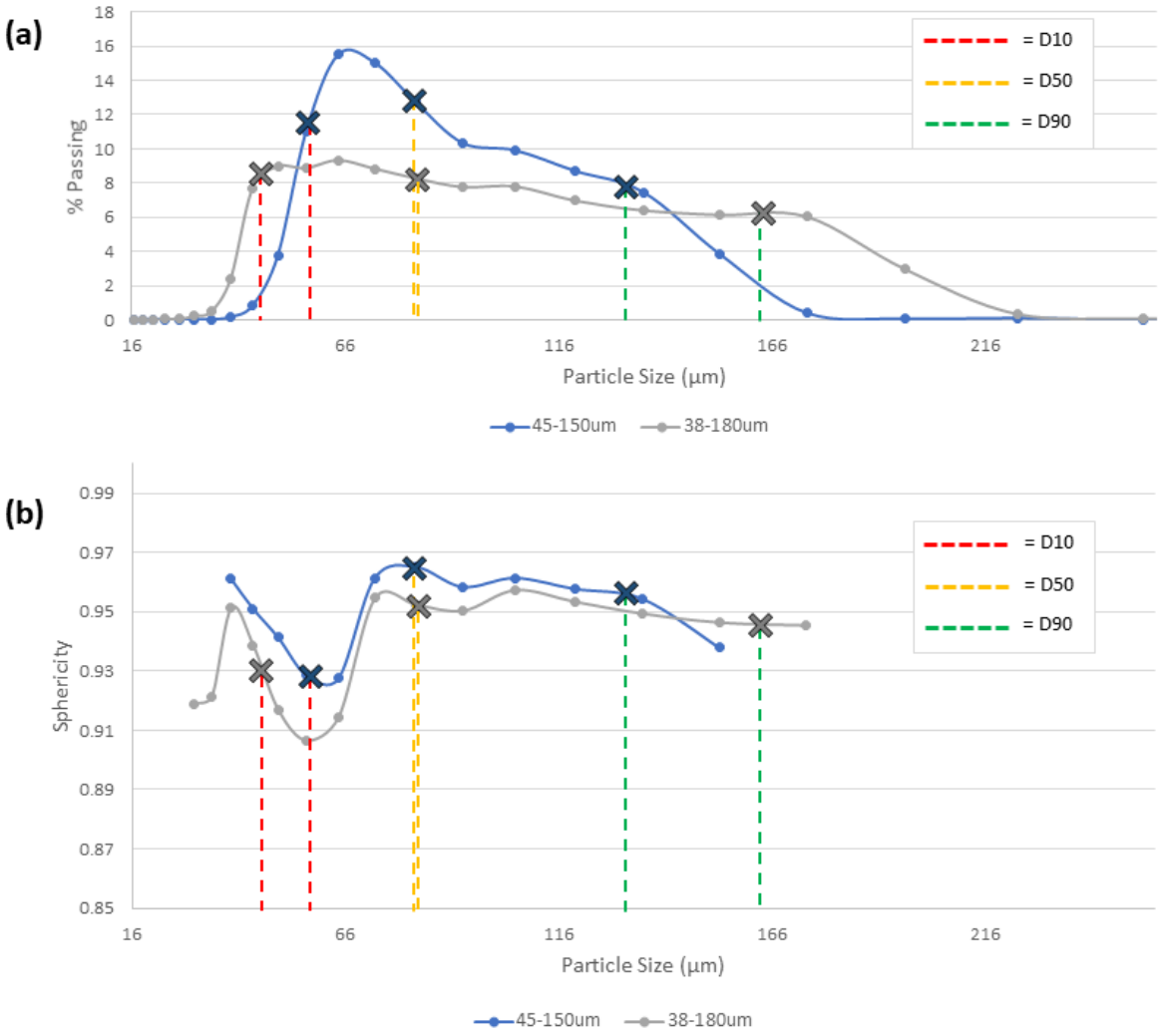


Figure 48. Powder representative graphs for both PSD 45-150 µm and 38-180 µm; a) The PSD distribution and; b) the sphericity for the PSD distribution.

5.3.2 General observations

Preliminary data distribution analysis

Preliminary data visualization is aimed at understanding the relationship between input parameters and resulting surface roughness. The data visualization in Figures 4, 5, & 6 shows the distribution for each run of all PSD samples (PSD 45-150 µm & 38-180 µm) where the responses Arithmetic Mean Height (SA), Texture aspect ratio (STR), and Arithmetic mean peak curvature (SPC) are presented as the surface roughness features. The hypotheses for each run are evaluated where the effect of changing the layer thickness and the beam factors are confirmed, and the comparison between the PSD 45-150 µm and PSD 38-180 µm is defined. The best surface roughness values for SA, STR, and SPC as shown in the table 2 below. A lower SA and SPC value and a higher STR value is preferred based on the definitions and explanations in Section 5.2.1. Overall, the experimental plan resulted in the lowest range for $SA \in [39.41 - 43.27]$ µm for PSD 45-150 µm and the lowest range for $SA \in [45.09 - 49.64]$ µm for PSD 38-180 µm. For this experimental study, one of the target surface roughness goals when optimizing the surface roughness is to achieve a SA value below the D50 and as close to the D10 as possible (PSD 45-150 µm: [D10 = 56.94, D50 = 80.12], and 38-180 µm: [D10 = 46.34, D50 = 81.17]).

Surface roughness in EBM is generally much higher than for other additive manufacturing (AM) technologies [22]. The surface roughness of titanium aluminide varies depending on the percentage of Aluminum and other deposit metals in the structure. For materials such as Ti6Al4V processed via EBM, the side surface roughness is usually ranging from 30-130 µm, where an optimized process produces results in surface roughness as low as 20 µm [81]. The Ti6Al4V surface roughness is expected to be different than the Ti-48Al-2Cr-2Nb material. Generally, Ti-48Al-2Cr-2Nb produces much higher surface roughness values; for example, Demirtas et al. [82] reported the as-build side surface roughness to be approximately 60.3 µm [82]. Even with a refinement of process parameters based on the literature findings, the SA or RA value is roughly around the 60 µm range [82]. A feasibility study was conducted prior to this experiment to confirm the literature claims and based on a preliminary surface roughness analysis using an initial screening with PSD 45-150 µm for 9 EBM-printed Ti-48Al-2Cr-2Nb samples, with three measurements (left, center, and right) collected for each side surface. The average SA value was determined to be within a range of 54-136 µm as seen in

Table 14 below.

Table 14. Feasibility study to define the SA range for Ti-48Al-2Cr-2Nb printed in the EBM system.

TiAl - Side Surface			
Sample	**Surface Roughness, Sa (µm)**		
	Left	**Center**	**Right**
1	270.69	62.00	165.85
2	185.43	76.69	205.71
3	224.45	50.61	191.11
4	240.18	51.98	255.31
5	195.31	55.15	180.83
6	252.72	62.13	244.36
7	150.46	60.69	167.01
8	170.68	71.63	215.89
9	137.52	59.62	257.21

Table 15. Showcases the process parameter that results in the best surface roughness (SA, STR, and SPC) for each experimental run hypothesis, with the corresponding best surface roughness and the reported worst surface roughness (SA, STR, and SPC).

Surface Roughness Feature	Run Type	PSD	Sample no	Speed (mm/s)	Focus Offset (mA)	No of Contours	Current (mA)	Best Surface roughness value	Worst Surface roughness value
SA (µm)	Run 1: Base	45-150 µm	Sample 6 (front)	200	5	4	8	43.27	127.2
		38-180 µm	Sample 1 (front)	450	12.5	2	6	49.64	109.76
	Run 2: Layer Thickness	45-150 µm	Sample 6 (front)	200	5	4	8	39.41	99.25
		38-180 µm	Sample 8 (left)	700	5	4	4	48.64	98.64
	Run 3: Slower & Sharper	45-150 µm	Sample 6 (front)	200	5	4	8	43.02	85.83
		38-180 µm	Sample 9 (left)	450	12.5	2	6	45.09	108.02
STR ()	Run 1: Base	45-150 µm	Sample 3 (left)	700	20	4	8	0.6982	0.1317
		38-180 µm	Sample 16 (front)	200	20	1	8	0.8126	0.0954
	Run 2: Layer Thickness	45-150 µm	Sample 18 (left)	700	5	1	4	0.6581	0.1072
		38-180 µm	Sample 16 (front)	200	20	1	8	0.7097	0.1094
	Run 3: Slower & Sharper	45-150 µm	Sample 8 (front)	300	5	2	7.5	0.6925	0.0984
		38-180 µm	Sample 12 (front)	400	10	1	5	0.6711	0.1171
SPC (1/mm)	Run 1: Base	45-150 µm	Sample 13 (front)	700	20	4	4	2689.12	3956.04
		38-180 µm	Sample 1 (front)	450	12.5	2	6	2344.20	3974.69
	Run 2: Layer Thickness	45-150 µm	Sample 7 (left)	200	5	1	4	2507.61	4084.31
		38-180 µm	Sample 1 (front)	450	12.5	2	6	2453.61	4120.85
	Run 3: Slower & Sharper	45-150 µm	Sample 9 (front)	400	10	3	5	2404.03	3941.63
		38-180 µm	Sample 8 (front)	300	5	2	7.5	2522.01	3983.59

Arithmetic mean height (SA)

The SA value is a commonly used surface roughness features employed to describe the surface outcomes for powder bed metal AM processes.

For this study, a bulk comparison between the SA quality outcomes based on the PSD and the experimental run (process parameter combinations) is captured. As seen in Figure 49, the narrower PSD range results in a slightly lower SA value based on the violin plot distributions of the surface roughness results. This comparison is consistent for all the experimental runs. Additionally, when comparing the experimental runs, the best reported SA values is 39 µm obtained from Run 2 PSD 45-150 µm. Run 2 analyzes the lower layer thickness hypothesis, which is expected to result in a low SA value [44], which is consistent for both PSD 45-150 µm and 38-180 µm. Run 1 shows the widest SA distribution width and Run 3 shows a smaller SA distribution width. Figure 49 also showcases the SA performance when compared to SA values, as reported in literature [44]. it can be seen that the datasets presented in this study outperformed the reported values in literature for both PSDs [82]. What is important to note is that the process parameters and layer thickness in Run 2 dampened completely the effects of PSD on the resulting outcomes, illustrating that there is promise in using the broader PSD range (38-180 µm) to obtain results similar to the narrower PSD range (45-150 µm). Regarding the literature review, there are a few studies analyzing the surface roughness using simulation approaches for laser powder-bed fusion (LPBF) [54]. Also, regarding experimental analysis, there have not been a lot of studies on the effect of PSD on AM surface quality outcomes. The few studies that are available typically inform on the LPBF technology for example Zhao Y et al. [54,83] conducted a study to review the effect of a lognormal distribution change that is used to define different ranges of PSD starting from 10% - 70% range with a 10% increment. Zhao Y et al. [54] states that as PSD range or layer thickness increases, so does the roughness of the bed surface [54]. Due to the increased number of potential combinations of particle arrangement for a wider range of particle sizes, the broader PSDs result in bigger fluctuations of surface roughness and solid volume fraction [54]. Our current study in EBM agrees with these general trends as well.

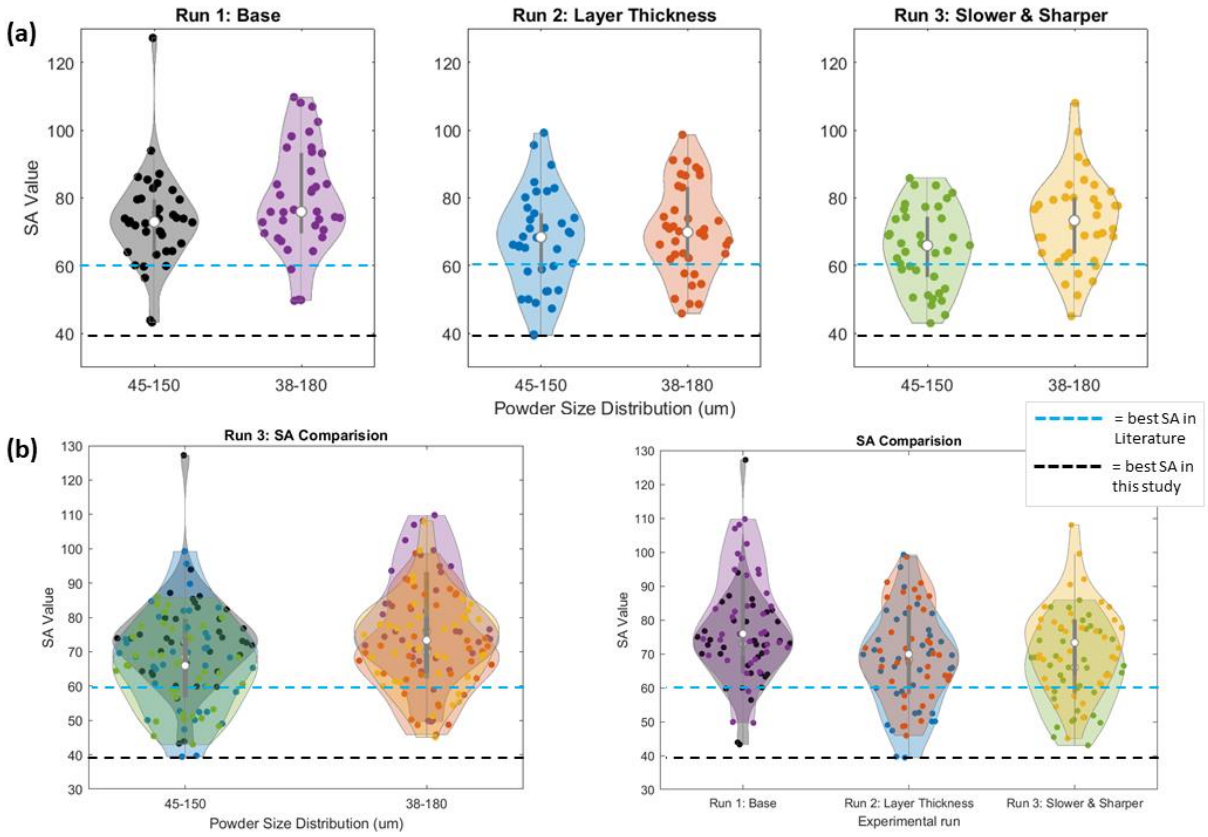


Figure 49. Violin plots showcasing the SA distribution for all the experimental analysis; a)The overal distribution; b) the distribution of SA results are overlayed to identify the change in values for the powder size distribution and the experimental runs. The blue dotted line indicates the best performing surface roughness for this material, as reported in the literature [82] and the black dotted line indicates the best surface roughness (SA) for Ti-48Al-2Cr-2Nb material in this experiment.

Texture aspect ratio (STR)

To the best of the author's knowledge, this is the first study describing the STR parameter in the context of PSD for EBM surface roughness. The STR value is another surface roughness feature that appears to influence the mechanical properties of printed parts. This is primarily due to the effect of having a uniform or random distribution of peaks on a surface. A more uniform peak is said to create larger stress points in the divots on the surface of the printed samples where failure can easily propagate through the uniform alignment of peaks. However, the randomized distribution does not have a surface

topology that allows for easy propagation of failure due to the random peak placement. Therefore, the STR value is an important feature that gives insight the potential mechanical behaviour of the observed object.

In this study, a bulk comparison between the STR quality outcomes based on the PSD and the experimental run (process parameter combinations) is captured. As seen in Figure 50, The highest obtained STR is 0.81 which fall under the PSD 38-180 µm for Run 1, which analysis the base parameter hypothesis. Overall, the 45-150 µm PSD range results in a slightly narrower STR distribution range for all three runs in this experiment. Slightly higher STR values are preferred, to reduce the repeated patterned layer effects and result in a more randomly-distributed surface. Additionally, when comparing the experimental runs, Run 1 and 2 which analysis the base parameter and lower layer thickness hypothesis respectively, the STR distribution are comparable with similar behaviours for the PSD. Run 1 and 2 provide the highest STR value distribution, which is consistent for both PSD 45-150 µm and 38-180 µm. As seen in the previous SA analysis, Run 2 shows a lower SA and high STR overall, therefore is seen as the better strategy when overlooking all three-hypothesis defined for this study. For Run 2, PSD 38-180 µm has a slightly higher STR value as compared to the 45-150 µm. Overall, Run 2 showcases the best result, however, base on the STR only, there is not a large discrepancy between the base process parameter combination and having a lower layer thickness.

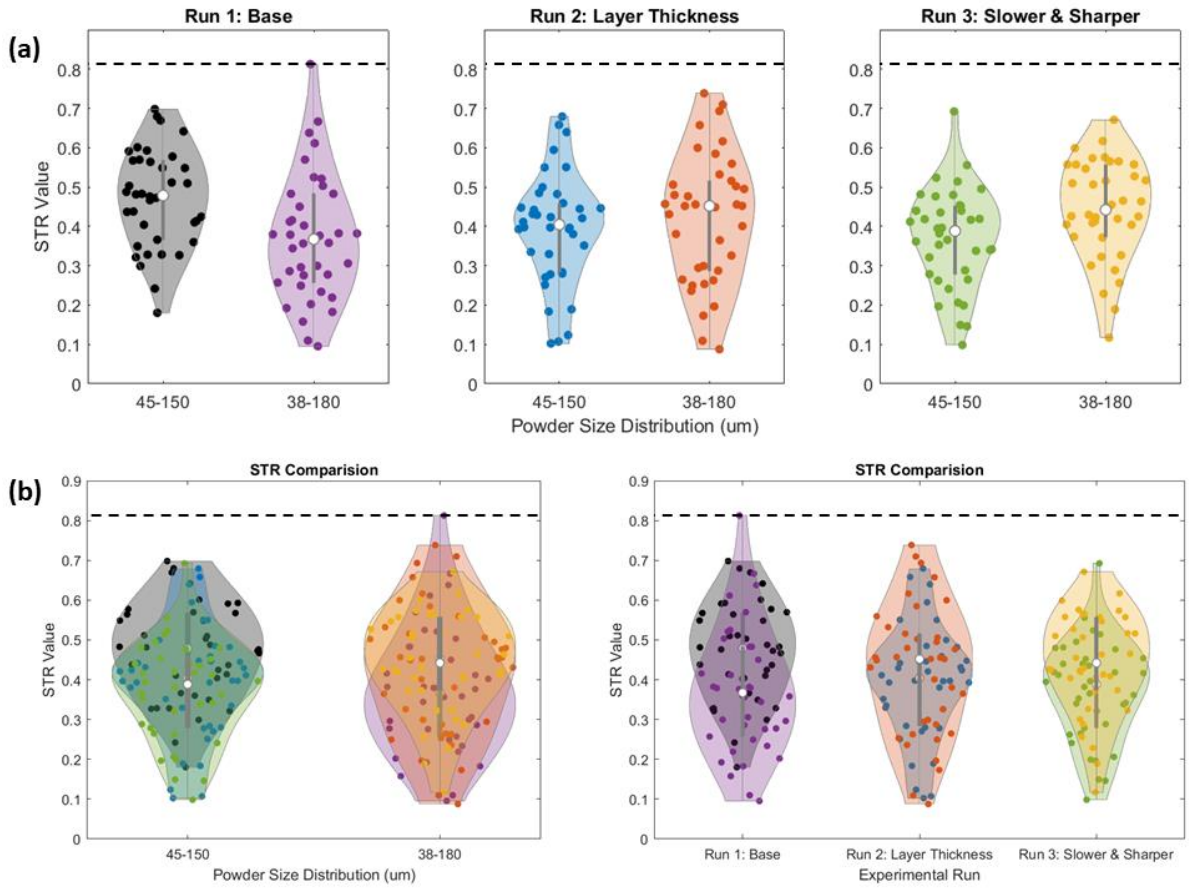


Figure 50. Violin plots showcasing the STR distribution for all the experimental analysis; a)The overall STR distribution; b) The distribution of STR results are overlayed to identify the change in values for the powder size distribution and the experimental runs. The dotted line indicates the the best surface roughness (STR) for Ti-48Al-2Cr-2Nb material in this experiment.

Arithmetic mean peak curvature (SPC)

To the best of the author's knowledge, this is the first study describing the SPC parameter for EBM surface roughness. The SPC is a surface roughness feature that influences the geometric fidelity of printed parts. This feature primarily describes the size (volume) of the peaks created during the EBM process. For this surface roughness feature, a high SPC value represents larger and wider peaks on the surface analyzed. A large SPC results in a large "bump" in the surface, creating a deviation from the ideal geometry, when compared to the expected geometry. Therefore, a smaller SPC is preferred to reduce the overall geometric deviations.

In this present study, comparison between the SPC quality outcomes based on the PSD and the experimental run (process parameter combinations) is captured. As seen in Figure 51, Run 2 showcases the best SPC result in the experiment at 1980 1/mm for the PSD 45-150 µm. Run 1 and 2 experiment showcases a similar distribution between the PSD 45-150 µm and 38-180 µm. For Run 3, however, there is a difference between the distribution witnessed for PSD 45-150 µm and 38-180 µm. The PSD 45-150 µm in run 3 has a lower distribution as compared to the 38-180 µm for the run 3 experiment. This difference is SPC distribution width is the largest for the run3 experiment which looks at investigating a smaller and sharper electron beam. Generally, PSD 45-150 µm has the widest SPC distribution width as seen in Figure 51 as compared to 38-180 µm, and the SPC average over the entire experiment is lowest in PSD 45-150 µm.

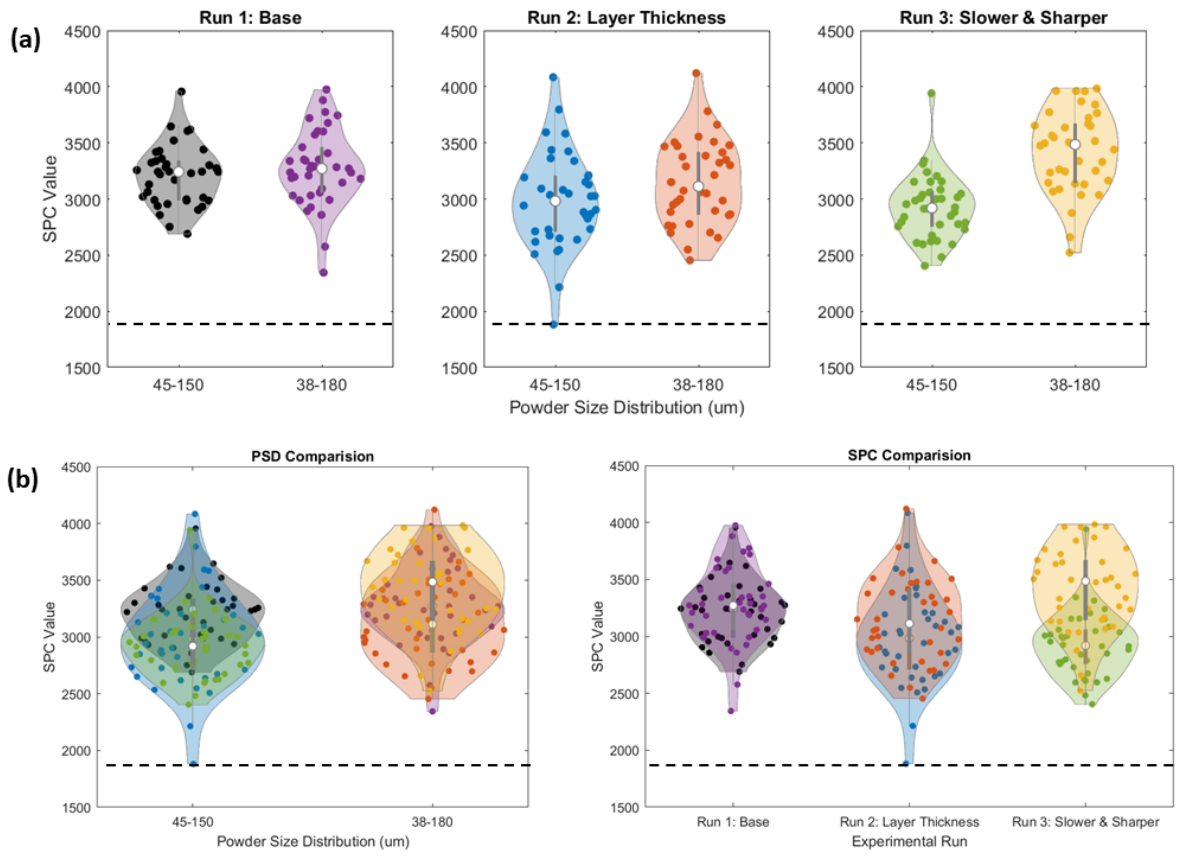


Figure 51. Violin plots showcasing the SPC distribution for all the experimental analysis; a)The overall SPC distribution; b) The distribution of SPC results overlayed to identify the change in values for the powder size distribution and the experimental runs. the black dotted line indicates the best surface roughness (SPC) for Ti-48Al-2Cr-2Nb material in this experiment.

5.3.3 Statistical analysis

The present study includes a comprehensive statistical analysis of the experimental data, covering PSD ranges of 45-150 µm and 38-180 µm, using Minitab software. With the help of this powerful statistical analysis tool, the study was able to shed light on the significant factors influencing the EBM process. The data analyzed in this study was designed through a Design of Experiments (DOE) framework, using a full factorial design. Based on a preliminary outlook into the statistical analysis of the resulting surface roughness values, there is a random pattern in residuals which affirms the robustness of the

statistical analysis. Therefore, using the full-factorial design is optimal and the study validated the unbiased nature of the data.

The study aimed to identify the key process parameters contributing to variability in the surface roughness response and to confirm the statistically significant effects of these process parameters on the surface roughness features. Additionally, the optimized response for each DOE and the impact of particle size distribution (PSD) on the resulting surface roughness is established. Minitab software develops a systematic DOE approach and provides a robust foundation for drawing meaningful insights into the relationships governing the EBM process variables and their effects on the final product's surface quality. The main areas of focus behind the statistical analysis are summarized below:

- Determine which factors contribute the most to the variability in the response
- Determine which factors have statistically significant effects on the response
- Determine the optimized response based on each DOE
- Determine the effect of PSD on the resulting surface roughness

The analysis of contour parameters in conjunction with PSD variations provides valuable insights into the intricate interactions between the EBM process parameters and PSD, and the impact on SA values. The contour process parameters, designated as A (focus offset), B (Speed), C (current), and D (number of contours), are the defined experimental values in this study. The PSD was considered to be an additional factor. It is imperative to emphasize that the significance of each factor corresponds to the degree of influence the contour parameter exerts on the SA value.

Pareto Chart Analysis – Overview

The process parameters observed and defined for the experimental analysis are: current, speed, number of contours and focus offset. Utilizing the full factorial analysis, statistical analysis was conducted. The Pareto chart is one of the resulting analysis complied for this study to showcase the statistical relationship between the process parameters and the surface roughness features. The Pareto chart shows the absolute values of the standardized effects from the largest effect to the smallest effect on the average surface roughness quality descriptors SA, STR, and SPC. The chart also plots a reference line to indicate which effects are statistically significant. The higher the significance of each factor, the

more the contour parameter affects the target surface roughness quality outcome value. For this experimental study, the critical standardized effect for all the analysis in this study is 4.303, which is equivalent to the significance level often denoted by α of 0.05, which translates to a 95 % confidence rate for the statistical predication made. The Pareto chart displays the absolute value of the effects; therefore, the degree of influence can be determined. Of note, a negative or positive relationship to the parameters cannot be determined using the Pareto analysis alone.

Pareto chart analysis – arithmetic mean height (SA)

The arithmetic mean height (SA) is a feature of Surface roughness that identifies the mean value of the peaks formed on the surface of the EBM-printed samples. SA is denoted as an absolute value representing the mean height of a specified measured surface area. During the profilometry scan, the difference in all the height of each surface peak achieve the arithmetical mean of the surface. Therefore, SA is identified as an important feature of the surface roughness, since it directly informs the peak and valley heights of the measured surface [50]. Further analysis is needed; therefore, the Pareto chart investigation for SA on all the experimental runs are defined in Figure 52.

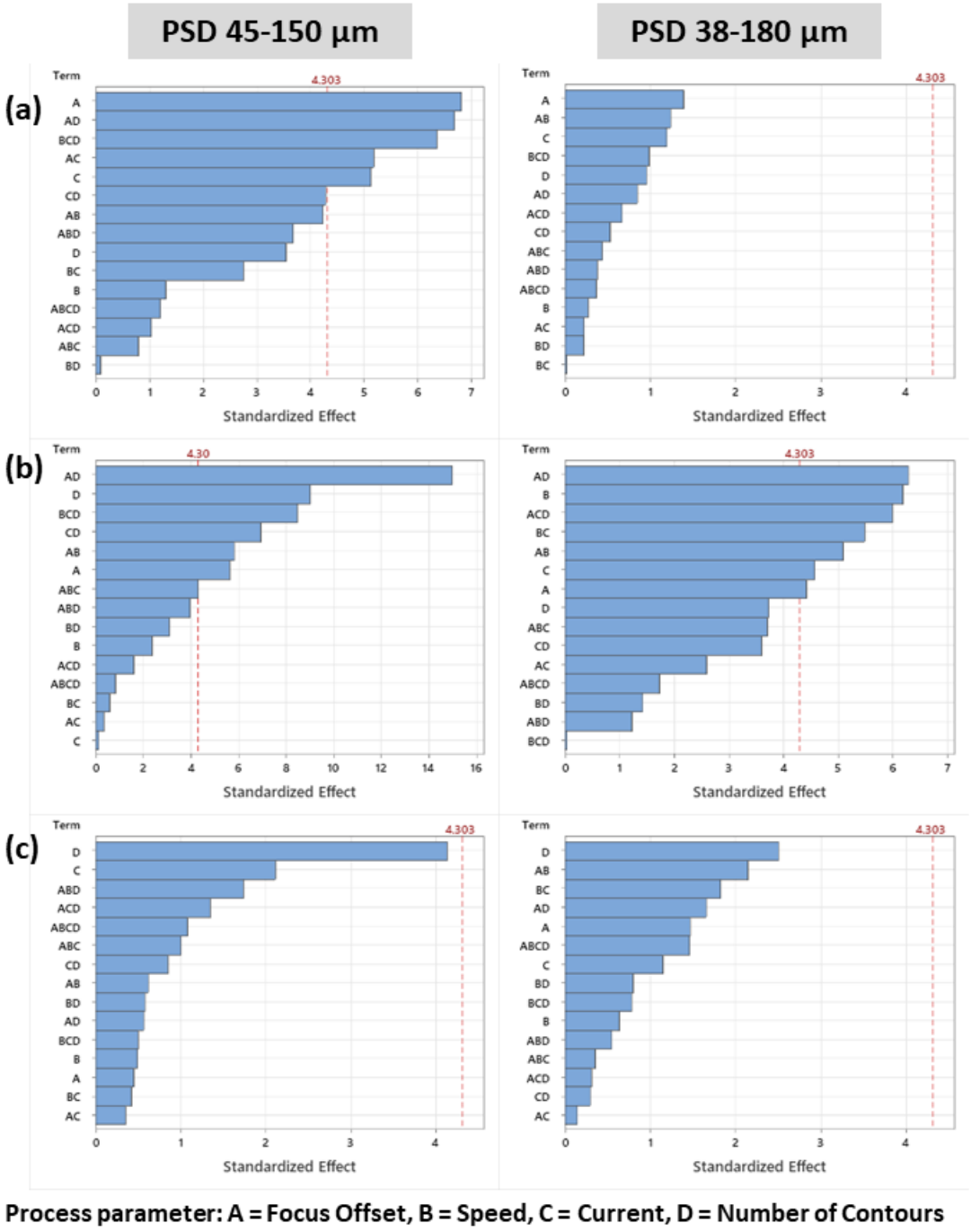


Figure 52. The Pareto Chart derived for all the SA experimental analysis for both PSD 45-150 µm and 38-180 µm; a) Run 1 base experiment; b) Run 2 layer thickness experiment; c) slower and sharper beam experiment.

Comparing the influence of PSD on SA values, a distinctive pattern emerges. For PSD 45-150 µm, contour parameters exhibit substantial influence on the SA values. Therefore, the resulting SA values are dependent on the specific contour parameters selected. Conversely, for PSD 38-180 µm, the contour parameters are not as significant when comparing the standardized effect of both PSDs. There are other features of the powder and the EBM process that play a larger role in the SA value formed in the experiment for the wider PSD range (PSD 38-180 µm). The powder morphology emerges as a dominant factor, overshadowing the influence of contour parameters on SA values, as we see a much smaller standardized effect for all the contour parameters.

In-depth analysis of specific runs provides further details to these observations. In Run 1, where base parameters were applied, the focus offset (A) was identified as the most influential factor on SA values, underscoring its critical role in shaping surface roughness outcomes. Run 2, incorporating variations in layer thickness, highlighted the heightened influence of focus offset and the number of contours on SA values. Notably, a lower layer thickness was found to mitigate the influence of PSD, emphasizing the enduring significance of process parameters irrespective of PSD variations. This is an important finding, as this underscores that, with the correct selection of layer thickness and process parameters, the two powders can have a comparable surface roughness performance, with similar trends in importance of factors A and D.

In the context of Run 3, characterized by slower and sharper conditions, the number of contours emerged as the most significant parameter affecting the SA result. Notably, as the electron beam stability increased, the impact of selected parameters on SA values decreased, indicating a nuanced relationship between beam stability and parameter influence. These findings contribute to a comprehensive understanding of how specific contour parameters, PSD variations, and overall process conditions collectively shape the surface characteristics in the EBM process, enriching our insights into the intricacies of this additive manufacturing technique.

Pareto chart analysis – texture aspect ratio (STR)

The texture aspect ratio (STR) is another feature of surface roughness that identifies the uniformity of the peaks formed on the surface of the EBM-printed samples. A more uniform peak location distribution is denoted with values closer to 1. Generally, for the EBM printed samples, the surface peaks and valleys showcase a pattern parallel to the build direction as seen in Figure 45. To achieve the best mechanical properties, a more random distribution of peaks at the surface is preferred, as it is indicative

of uniform boding of layers at the contours. Stress formation on the surface of the EBM sample are more likely to exist in the divots of a more uniform pattern, meanwhile a random peak distribution reduces the chances of stress buildup on the surface that can lead to surface cracking. Based on the resulting STR values from the experimental analysis, the Pareto chart analysis for STR on all the experimental runs are defined in Figure 53. The PSD 45-150 µm and 38-180 µm have a different analysis result.

For PSD 45-150 µm, the overall standardized effect for the contour parameters are smaller that the PSD 38-180 µm in each equivalent run experiment. Therefore, the process parameters in the PSD 38-180 µm affect the STR results to a larger degree, as compared to PSD 45-150 µm. The hypothetical reason for this is due to the morphology of the feedstocks. For PSD 45-150 µm, the powder distribution is smaller than the PSD 38-180 µm feedstock and this uniformity in the powder can more directly be translated to the resulting STR since there isn't as large of a change in powder size. Inversely, the PSD 38-180 µm, which is a wider powder size contains larger powder particles which can create a more random peak formation due to random placement as the powder is spread on the powder-bed. This occurrence can also be highlighted in the results identified in the Run 2 experiment for both 45-150 µm and 38-180 µm. This experiment utilized a reduced layer thickness as the primary point of analysis. Due to the reduced layer thickness (70 µm), there is a chance that layers are re-melted or that the larger particles are removed from the powder-bed by the re-coating process before melting. Based on this experiment for both PSDs', the standardized effect for the contour parameters are reduced to a similar level. The highest influencing parameters are roughly at 2 standardized effect value. This showcases that the process parameters are not significant enough to be statistically considered as a feature that influences the STR values. Therefore, the powder morphology is a more dominant feature in this scenario.

Additionally, in the Pareto Chart analysis in Figure 53, none of the process/contour parameters in the PSD 45-150 µm are statistically significant in the STR formation. However, for PSD 38-180µm, the most prominent parameter that influence the STR value is the Current. A combination of Current and Speed in the Run 1 experiment is also considered as the most significant parameter. However, generally, regardless of the specified process parameter range defined, the current is considered as one of the parameters with the highest influence on the STR value. It is possible that the higher current results in a higher propensity for re-melting of contours in prior layers, resulting in a lower overall surface roughness.

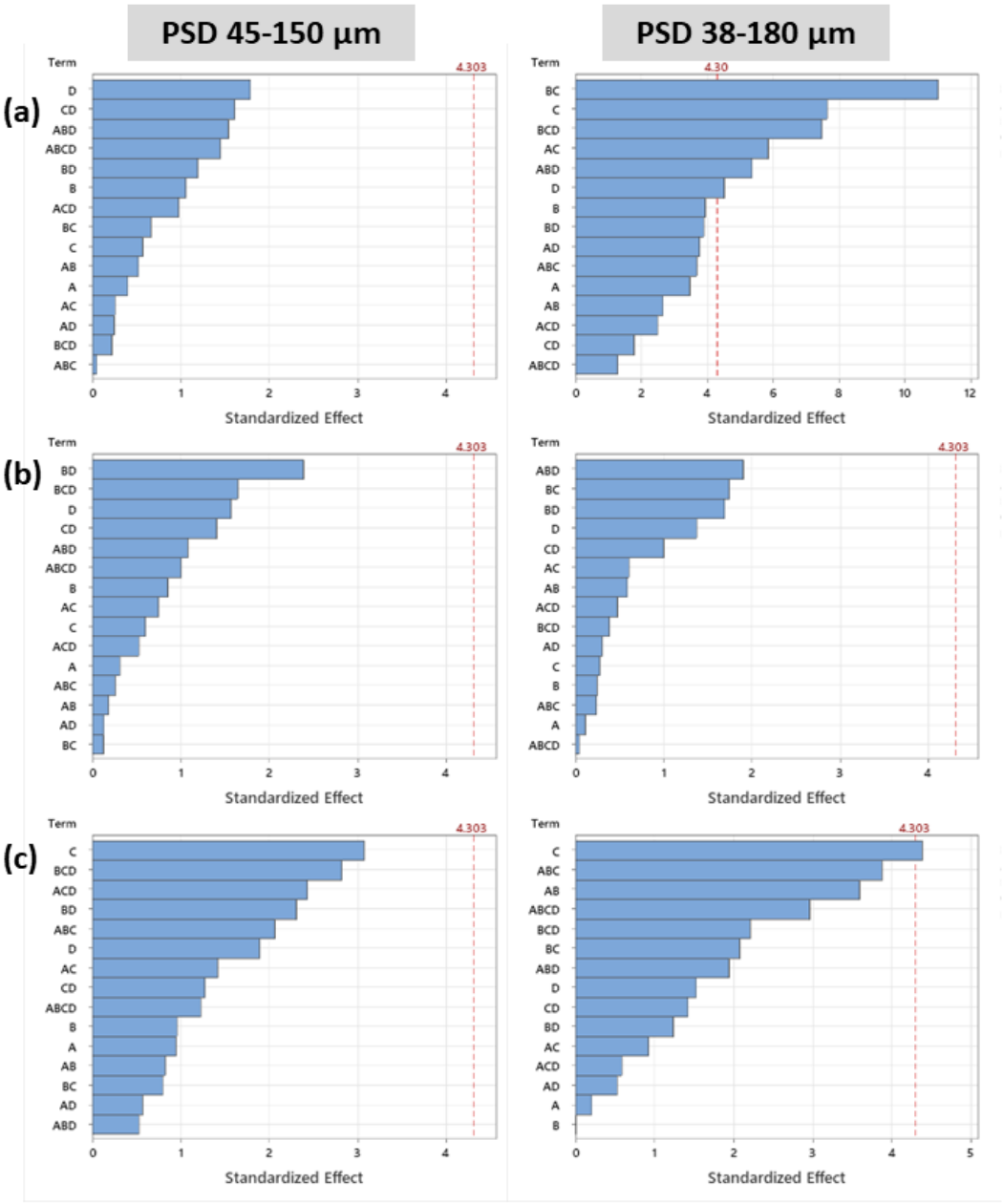


Figure 53. The Pareto Chart derived for all the STR experimental analysis for both PSD 45-150 µm and 38-180 µm; a) Run 1 base experiment; b) Run 2 layer thickness experiment; c) slower and sharper beam experiment.

Pareto chart analysis – arithmetic mean peak curvature (SPC)

The Arithmetic mean peak curvature (SPC) is another feature of Surface roughness that represents the arithmetic mean of the principal curvature of the peaks on the surface of the EBM-printed samples. A larger SPC value represents a wider surface peak and is usually not the preferred. Based on the resulting SPC values from the experimental analysis, the Pareto chart analysis for SPC on all the experimental runs are defined in Figure 54. The PSD 45-150 µm and 38-180 µm have a different analysis result.

The SPC results is different from the SA and STR results. The contour parameter as a whole does not have a large influence on the SPC regardless of the PSD. The only run experiment that has parameters considered as statistically significant in defining the SPC is the run that analysis a lower layer thickness as the main hypothesis. The parameter combination that was statistically significant is Speed and Number of Contours. Overall, the number of contours is considered as the highest influencing parameter regardless of the statistical significance.

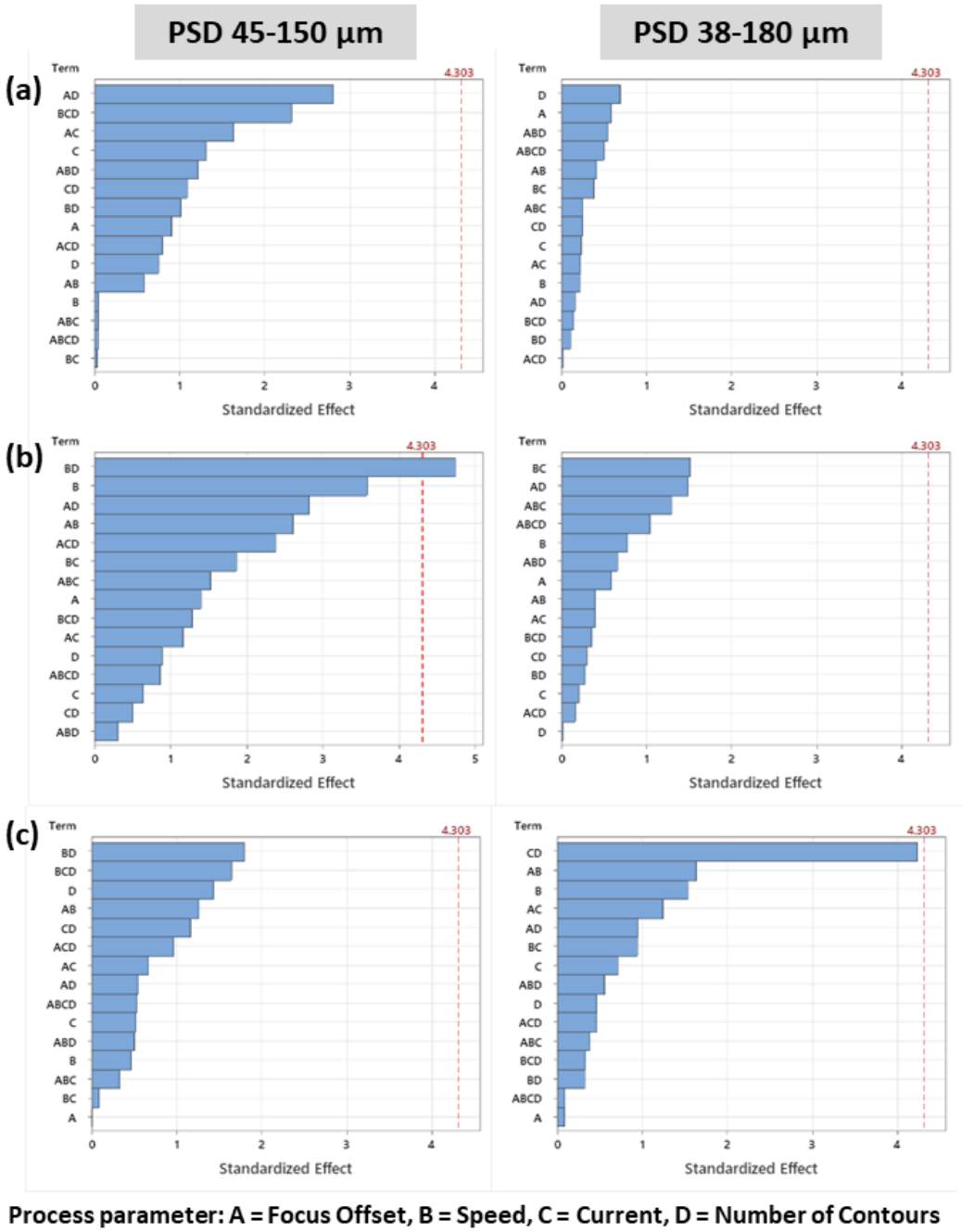


Figure 54. The Pareto Chart derived for all the SPC experimental analysis for both PSD 45-150 µm and 38-180 µm; a) Run 1 base experiment; b) Run 2 layer thickness experiment; c) slower and sharper beam experiment.

Response optimizer – overview

The Response Optimizer is a sophisticated tool that adds value to the analysis by identifying the best combinations of input variable or process parameter settings in the EBM process which provides the best surface roughness feature values also improving specific responses. In this particular case, the goal is to simultaneously reduce SA, increase STR, and decrease SPC values. Minitab software uses advanced techniques to predict responses and pinpoint the optimal parameter settings required to achieve these desired outcomes, based on the bounds of the original experiment.

The current ranking of responses reflects their respective importance in the context of the EBM process. The primary consideration is SA, followed by STR and then SPC. This ranking highlights the importance of achieving the right balance between minimizing SA, maximizing STR, and minimizing SPC simultaneously. The Response Optimizer aligns with these priorities and becomes a useful tool in selecting parameter settings that yield the most favorable outcomes across multiple surface roughness responses, improving the efficiency and effectiveness of the EBM process in achieving quality surface topology. The multiple response optimizer for all the experiment and surface roughness features is shown in Table 16. The confidence level of the reported values is based on 95%

Table 16. The resulting optimized Surface roughness for SA, STR, and SPC with the corresponding process parameter predicted

PSD	Experimental Design	Focus Offset	Speed	Current	No of Contour	SA	STR	SPC
45-150 µm	**Base**	5	200	8	4	42.86	0.5160	3011
	Layer Thickness	5	200	8	4	40.65	0.5364	2956
	Slower & Sharper	10	400	5	3	55.62	0.5380	2621
38-180 µm	**Base**	5	200	8	4	50.81	0.3978	3197
	Layer Thickness	20	700	4	1	57.84	0.5446	2941
	Slower & Sharper	11	200	5	3	62.14	0.5491	3202

The use of Response Optimizer, along with a thorough analysis of contour parameters and Particle Size Distribution (PSD) variations provides valuable insights into optimizing the EBM process for important surface roughness features like SA, STR, and SPC.

To achieve optimal SA, STR, and SPC values, an appropriate combination of various contour parameters is required. The Response Optimizer confirms the critical contour parameter combination

and highlights the crucial role of parameter selection in navigating the complex relationships between contour parameters and surface roughness response variables. The optimizer suggests that a reduced layer thickness yields the best results for all response variables. However, a sharper and slower beam configuration consistently produces less favorable outcomes.

Comparing PSD variations, both PSDs exhibit normal distribution, enhancing the reliability of the comparative analysis. PSD 45-150 µm predicts a lower SA value of 40.65, as compared to the PSD 38-180 µm 50.81. For STR values, PSD 38-180 µm outperforms PSD 45-150 µm, potentially due to the larger particles present in the feedstock, which are randomly fused at the surface creating scattered peaks on the EBM printed side surface. Analyzing SPC, PSD 38-180 reveals lower sensitivity to contour parameters, while the narrower PSD 45-150 consistently yields smaller SPC values, emphasizing the impact of PSD on resulting porosity.

These findings emphasize the complex interplay between contour parameters, PSD variations, and key response variables in the EBM process. The Response Optimizer proves to be a useful tool in selecting optimal parameter settings to enhance efficiency and performance. This comprehensive approach towards process optimization ensures a thorough understanding of the intricate relationships governing the EBM process, which can lead to advancements in additive manufacturing.

Response optimizer – arithmetic mean height (SA)

Generally, the SA value is the most commonly utilized surface roughness feature to confirm the quality of the resulting surface roughness. This is primarily due to the availability and necessity of post processing of the surface. Due to the need of post processing, by considering the SA value exclusively, the time, effort and cost required to achieve an excellent surface finish is more heavily dependent on the SA value. Having a smaller SA value can reduce the amount of time and cost needed to polish the surface significantly. Additionally, based on the Pareto chart analysis, the SA is most largely influenced by the process parameters and the other two features (STR, and SPC) are more heavily dependent on the powder feature. For this reason, a singular Response Optimizer is considered to achieve the lowest possible SA value, regardless of the STR and SPC results. Based on the surface roughness requirements, the results of the Response optimizer is shown in Table 17.

Table 17. The resulting optimized Surface roughness for SA, STR, and SPC with the corresponding process parameter predicted

PSD	Experimental Design	Focus Offset	Speed	Current	No of Contour	SA
45-150 µm	**Base**	5	200	8	4	42.86
	Layer Thickness	5	200	8	4	40.65
	Slower & Sharper	10	200	10	3	49.32
38-180 µm	**Base**	5	200	8	4	49.9
	Layer Thickness	5	700	8	4	49.46
	Slower & Sharper	0	400	5	3	57.92

Based on the resulting SA values and their corresponding process parameters, the trend across the experiment is identified. The optimized number of contours value is high. Based on the experiment, the recommended value for the number of contours is 4 and 3, which are the highest values used through this experiment. Therefore, to achieve a reduced SA value, increasing the number of contour is necessary.

Generally, in PSD 45-150 µm, a higher current and slower speed and sharper beam produces the best results for the run 1 and 2, however, when the beam parameters were changed for run 3 to test the hypothesis that a slower and sharper beam is preferred, the focus offset was increased to achieved to best parameter combination, which effectively diminishes the beam sharpness. This shows that there is a threshold of the current, speed, and focus offset combination that produces the best results for PSD 45-150 µm. Additionally, for PSD 38-180 µm, a similar relationship is witnessed. Run 1 predicts a higher current, slower speed and sharper beam as the best contour parameter combination to produce the lowest SA result. Run 2, however recommends the higher speed within the specified range of the experiment (high speed, high current and sharper focus offset was recommended). Additionally, for Run 3, which tests the hypothesis of a slower and sharper beam, the recommended parameter combination is a faster speed and a smaller current with the expected sharper focus offset. Therefore, there is a specific ratio relationship of these three parameters (current, speed, and focus offset) that produced and ideal SA result. In PSD 45-150, the range of the current, speed, and focus offset combination threshold is different from the PSD 38-180 µm. PSD 45-150 µm allows a much sharper and slower speed combination as compared to PSD 38-180 µm when aiming to obtain a minimized SA result.

Chapter 6
Conclusion and Future Works

The overall objective of this study is to elucidate the relationship between the various levels of the PSD on the density, porosity type, and surface roughness. The trend and threshold of the density, porosity type, and surface roughness formations for each PSD type are understood by examining the EBM process parameter combination themes (high energy combination, low energy combination) and result distribution. Overall, this work confirms the inherent behavior of Ti-48Al-2Cr-2Nb material in EBM, opening the door to the development of machine learning (ML) models or analyses that can reliably and precisely anticipate the results of EBM printing.

Objective 1: Investigating the powder features of three different PSD ranges for Ti-48Al-2Cr-2Nb powder particles.

i. All the PSD's measured in this study for Ti-48Al-2Cr-2Nb appear to be spherical in shape for the virgin powder. Particle size ranging from 0 – 66 µm (approximately) produces a slightly lower sphericity (0.9 as compared to 0.96 for the larger virgin particles) in each PSD category. Therefore, the smaller particles in the virgin powder are usually not perfectly spherical in shape as compared to the higher particle sizes.

ii. The flowability and packing density for Ti-48Al-2Cr-2Nb are different for all PSD's measured (PSD 38-150 µm, PSD 45-150 µm, and PSD 38-180 µm). PSD 45-150 µm has the best flowability and density, followed by PSD 38-150 µm and then PSD 38-180 µm. However, all the reported flowability and packing density for the virgin powder of all PSD's are considered to be excellent.

iii. PSD 45-150 µm has the best cohesive index and is considered to be good. The other PSD's measured show a higher cohesion level in comparison with the widest PSD (38-180 µm) shows a slightly better cohesion than the 38-150 µm. The 38-150 µm particles enters the "poor" cohesion level. Based on this trend, it is likely that having a dominant percentile of smaller particles in the distribution increases cohesion of the bulk.

iv. Based on the powder computed tomography analysis,

a. The powder porosity across all PSD's generally appear in the larger powder particles. There is a larger powder porosity ratio in the powder feedstock in PSD 38-180 µm followed by PSD 45-150 µm and then PSD 38-150 µm.

b. Most powder porosity found in the powder particles is spherical in shape.

c. The reused powder for all PSD's in this study contains some large particle volumes that are attributed to the powder recovery process and sintering of the powder during EBM-printing.

Future Works: Some of the investigations that can be conducted based on the conclusions of this objective includes:

i. Creating models and simulations to demonstrate the behaviour of the Ti-48Al-2Cr-2Nb powder in the EBM printing chamber. This includes powder spreading behaviour for the different PSD's (PSD 38-150 µm, PSD 45-150 µm, and PSD 38-180 µm) and the effect different levels of applied energy or melting process parameter combination has on the melted powder-bed layers.

Objective 2: Investigating the comprehensive pore defect analysis for EBM-printed Ti-48Al-2Cr-2Nb

This thesis investigates the relationships between process parameters, applied energy, density / porosity and types of porosity for Ti-48Al-2Cr-2Nb EBM-printed samples.

i. The Gas pores formed in the EBM-printed samples are the result of porosity in the feedstock utilized. Gas porosity levels are generally low, in the range of (0.01% – 0.17% for the Excellent threshold, 0.1% – 0.23% for the Good threshold, 0.12% - 0.3% for the Poor threshold, and 0.2% – 0.3% for the Failed threshold). The levels remain relatively consistent with overlapping values regardless of bulk density results across all four performance classes, with a slight increase in porosity as the threshold moves from Excellent to Failed.

ii. The Lack of Fusion pores created in the EBM printed samples emerge as a result of a low applied energy input to the process. This porosity type has a high correlation to the overall bulk porosity level, with LOF porosity in the range of (0.001% – 0.1% for the Excellent threshold, 0.02% – 0.2% for the Good threshold, 0.09% - 1.5% for the Poor threshold, and 1.9% – 12% for the Failed threshold).

iii. High density samples tend to have a predominant Gas pores fraction as compared to LOF, however as the density level reduces, this relationship is reversed, with higher dominance of LOF pores as compared to Gas pores.

iv. As the applied energy (often denoted by the Normalized Enthalpy and Volumetric Energy Density) in the EBM process increases, the resulting general porosity level decreases.

v. Normalized Enthalpy is a better identifier for representing the applied energy. Thresholds or regions can be defined in the NE due to the inclusion on multiple parameter features in the NE as compared to VED. A NE>15 appears to consistently result in Excellent performance, whereas a NE<10 appears to result in a Failed performance class outcome.

Future Works: Some of the investigations that can be conducted based on the conclusions of this objective includes:

i. Creating ML model that can predict and replicate the density based on the EBM parameters and the applied energy threshold defined for the reference PSD (PSD 45-150 μm). This includes investigating the specific process parameter combination that results in a specific applied energy (using VED and NE as our energy representation) and identifying the specified energy level that results in density that falls in each classified threshold (excellent, good, poor, failed).

ii. Analysis on the LOF pore morphology can be conducted. Insufficient applied energy is identified as the reason for LOF pore formation, but the shape and morphology of these pores can vary as well as the location and propagation of these porosities across the entire EBM build. Therefore, investigating other features of the EBM that influences the LOF pores, for example, the powder-bed behaviour and instabilities in the melt pool can give insight on ways to achieve a better density result at a lower applied energy process.

iii. More research needed to be done to identify potential way gas porosity can be reduced substantially within the EBM process. This could include investigating extremely highly energy levels to identify the threshold for gas to escape from within the melt pool, or changing melting strategies that more efficiently create a melt pool layer where gas pores can easily escape the melt pool before solidification.

Objective 3: Investigating and comparison analysis of pore defect for different PSD EBM-printed Ti-48Al-2Cr-2Nb

This thesis investigates the relationships between process parameters, applied energy, density / porosity and types of porosity for two different PSD sizes (45-150 µm and 38-180 µm) Ti-48Al-2Cr-2Nb EBM-printed samples. The effect and trends for each PSD and the hypothesis behind the density behavior is elucidated in this study.

i. The bulk porosity levels for both PSD 45-150 µm and 38-180 µm consistently increased as thresholds shifted from 'Excellent' to 'Failed' states. This highlighted the similar influence of PSD on resulting bulk porosity, within the studied process parameter windows. It was also discovered that breaking down the overall porosity into LOF and Gas porosity types could help in better understanding other changes.
ii. As the applied energy VED and NE increases in the EBM system, the expected overall porosity is reduced. This trend was identified in all the experimental samples regardless of the threshold.
iii. NE provided a better representation of the relationship between the applied energy and porosity as compared to VED for both PSD 45-150 µm and 38-180 µm. Samples in the Failed category had a lower NE value, as compared to the higher density thresholds which had a wider range of NE values.
iv. While the range of gas porosity remained similar in both PSD 45-150µm and PSD 38-180 µm, a slight increase in gas porosity was observed in PSD 45-150 µm, when going from the Excellent to the Failed class. Interestingly, PSD 38-180 µm exhibited a slightly lower Gas porosity level compared to PSD 45-150 µm. This observation suggested that the powder feature for the wider PSD 38-180 µm range may contribute to mitigating variations in defect morphology and size, influencing the resulting porosity levels in Ti-48Al-2Cr-2Nb EBM-printed samples.
v. The LOF pore distribution for PSD 45-150 µm and 38-180 µm showcased a similar distribution regardless of the threshold levels, more so than the Gas pore distribution. Although, it appeared PSD 45-150 µm presented a lower porosity limit in the distribution for all four thresholds, as compared to the PSD 38-180 µm.
vi. As the regime (speed and current combination) moves from low to high, there is less influence from the process parameter in changing the density results. PSD 45-150 µm predicts a lower

density for the super-high regime (super high speed and current combination), however, achieving a very high density is possible in the other two regimes (low and high regime – low speed and current combination and high speed and current combination respectively) and is dependent on the process parameter combination. However, PSD 38-180 µm predicts a higher density across the experiment for the super-high regime, and the other two regimes depict a wider variety in the resulting density values, where the influence of process parameter is not as straightforward.

Overall, these conclusions provide valuable insights into the relationship between process parameters and structural integrity of Ti-48Al-2Cr-2Nb EBM-printed samples, and could inform future research in this area.

Future Works: Some of the investigations that can be conducted based on the conclusions of this objective includes:

i. Experimental validation of the proposed forecasted density result based on the DOE should be conducted to confirm the relationship and trends identified in this study across the varied PSD.
ii. An experimental study that investigates the changes in density for process parameter combinations that result in the same or closely reported NE or VED values for the varied PSD can be conducted. This analysis can give more insight into potential features of the EBM-process that influences the density results to a larger degree than the largely varied reported applied energy.
iii. Analysis conducted on the types of porosity formed during printing for various PSD. This includes analysis to what creates the changes in the gas pore level for both PSD, which will include the differences on the PSD powder features such as porosity, morphology, flowability and powder-bed behaviour. Understanding how the powder features influence the resulting porosity development in the EBM-process can create an avenue to reduce porosity formation, specifically the gas pores.

Objective 4: Investigating and comparison analysis of surface roughness for different PSD EBM-printed Ti-48Al-2Cr-2Nb

i. Comparing PSD variations, both PSDs exhibit normal distribution. Based on the response optimizer, PSD 45-150 µm predicts a lower SA value of 40.65 µm, as compared to the PSD

38-180 µm 50.81 µm. For STR values, PSD 38-180 µm outperforms PSD 45-150 µm, potentially due to the larger particles present in the feedstock, which are randomly fused at the surface creating scattered peaks on the EBM printed side surface. Analyzing SPC, PSD 38-180 reveals lower sensitivity to contour parameters, while the narrower PSD 45-150 consistently yields smaller SPC values, emphasizing the impact of PSD on resulting porosity.

ii. SA Surface roughness

   a. Layer thickness highly influences the surface roughness results to a large degree. For SA, the layer thickness runs produces the best value of 39 µm. A lower layer thickness was found to mitigate the influence of PSD, highlighting the importance of process parameters, irrespective of PSD variations. This is an important finding, as this underscores that, with the correct selection of layer thickness and process parameters, the two powders can have a comparable surface roughness performance.
   b. In-depth analysis of specific process parameter across the entire experiments highlights the heightened influence of focus offset and the number of contours on SA values. The focus offset and number of contours generally hold the highest standardized effect in the selection of process parameter: speed, current, focus offset, and number of contours.

iii. STR Surface roughness: Stress formation on the surface of the EBM sample are more likely to exist in the divots of a more uniform pattern, meanwhile a random peak distribution on the surface reduces the chances of stress buildup that can often lead to surface cracking.

   a. PSD 45-150 µm has a smaller powder distribution than the PSD 38-180 µm feedstock and this uniformity in the PSD 45-150 µm powder can more directly be translated to the a smaller STR (more uniform surface peak alignment) since there isn't a large change in powder size. Inversely, the PSD 38-180 µm, which is a wider powder size contains larger powder particles which can create a more random peak formation due to random placement of the larger particles as the powder is spread on the powder-bed.

iv. SPC Surface roughness:

   a. The contour parameter as a whole does not have a large influence on the SPC regardless of the PSD. However, a lower layer thickness is expected to result in smaller SPC values. With a smaller layer thickness, the Speed and Number of Contours parameter

combination is considered statistically significant, or tends to have the highest influence on the SPC result.

b. Overall, the number of contours is considered as the highest influencing parameter regardless of the statistical significance.

Future Works: Some of the investigations that can be conducted based on the conclusions of this objective includes:

i. Experimental validation of the proposed best forecasted surface roughness parameters (SA, STR, and SPC) result based on the DOE should be conducted to confirm the relationship and trends identified in this study across the varied PSD.

ii. Investigation of the surface cracking and the surface roughness parameters (SA, STR, and SPC) relationship can be conducted across different Ti-48Al-2Cr-2Nb PSDs (PSD 38-150 µm, PSD 45-150 µm, and PSD 38-180 µm) to understand the effect of surface roughness on the mechanical properties.

iii. ML models can be developed to defined and forecast process parameter combination that result in a specified surface roughness parameter value.

Letter of Copyright Permission

Letter 1: Copyright Letter for Figure 1

ELSEVIER LICENSE TERMS AND CONDITIONS

Apr 22, 2024

This Agreement between Tomisin Oluwajuyigbe ("You") and Elsevier ("Elsevier") consists of your license details and the terms and conditions provided by Elsevier and Copyright Clearance Center.

License Number	5774290254426
License date	Apr 22, 2024
Licensed Content Publisher	Elsevier
Licensed Content Publication	Elsevier Books
Licensed Content Title	Reference Module in Materials Science and Materials Engineering
Licensed Content Author	Hafiz M. Alojaly,Abdelmonem Hammouda,Khaled Y. Benyounis
Licensed Content Date	Jan 1, 2023
Licensed Content Pages	1
Start Page	0
End Page	0
Type of Use	reuse in a thesis/dissertation
Portion	figures/tables/illustrations
Number of figures/tables/illustrations	1
Format	electronic
Are you the author of this Elsevier chapter?	No
Will you be translating?	No
Title of new work	Variation in powder size distribution for electron beam melting of TiAl - density and surface roughness effects
Institution name	University of Waterloo
Expected presentation date	May 2024
Portions	Fig. 15
Requestor Location	Tomisin Oluwajuyigbe 102 Courtland ave E Kitchener, ON N2G2V1 Canada Attn: University of Waterloo
Publisher Tax ID	GB 494 6272 12
Total	**0.00 CAD**

Letter 2: Copyright license for Figure 2

ELSEVIER LICENSE TERMS AND CONDITIONS

Apr 22, 2024

This Agreement between Tomisin Oluwajuyigbe ("You") and Elsevier ("Elsevier") consists of your license details and the terms and conditions provided by Elsevier and Copyright Clearance Center.

License Number 5774260179319

License date Apr 22, 2024

Licensed Content Publisher Elsevier

Licensed Content Publication Vacuum

Licensed Content Title Electron beam welding – Techniques and trends – Review

Licensed Content Author M.St. Węglowski,S. Błacha,A. Phillips

Licensed Content Date Aug 1, 2016

Licensed Content Volume 130

Licensed Content Issue n/a

Licensed Content Pages 21

Start Page 72

End Page 92

Type of Use reuse in a thesis/dissertation

Portion figures/tables/illustrations

Number of figures/tables/illustrations 1

Format electronic

Are you the author of this Elsevier article? No

Will you be translating? No

Title of new work Variation in powder size distribution for electron beam melting of TiAl - density and surface roughness effects

Institution name University of Waterloo

Expected presentation date May 2024

Portions Fig. 3

Requestor Location Tomisin Oluwajuyigbe
102 Courtland ave E

Kitchener, ON N2G2V1
Canada
Attn: University of Waterloo

Publisher Tax ID GB 494 6272 12

Total 0.00 CAD

Letter 3: Copyright license for Figure 6

ELSEVIER LICENSE TERMS AND CONDITIONS

Apr 22, 2024

This Agreement between Tomisin Oluwajuyigbe ("You") and Elsevier ("Elsevier") consists of your license details and the terms and conditions provided by Elsevier and Copyright Clearance Center.

License Number	5774260064937
License date	Apr 22, 2024
Licensed Content Publisher	Elsevier
Licensed Content Publication	Journal of Volcanology and Geothermal Research
Licensed Content Title	Measuring the size of non-spherical particles and the implications for grain size analysis in volcanology
Licensed Content Author	Hannah M. Buckland,Jennifer Saxby,Matt Roche,Phoebe Meredith,Alison C. Rust,Katharine V. Cashman,Samantha L. Engwell
Licensed Content Date	Jul 1, 2021
Licensed Content Volume	415
Licensed Content Issue	n/a
Licensed Content Pages	1
Start Page	107257
End Page	0
Type of Use	reuse in a thesis/dissertation
Portion	figures/tables/illustrations
Number of figures/tables/illustrations	1
Format	electronic
Are you the author of this Elsevier article?	No
Will you be translating?	No
Title of new work	Variation in powder size distribution for electron beam melting of TiAl - density and surface roughness effects
Institution name	University of Waterloo
Expected presentation date	May 2024
Portions	Fig. 2
Requestor Location	Tomisin Oluwajuyigbe 102 Courtland ave E Kitchener, ON N2G2V1 Canada Attn: University of Waterloo
Publisher Tax ID	GB 494 6272 12
Total	**0.00 CAD**

References

[1] S. Fager, F.J. Karlsson, M. Knutson Wedel, γ-Titanium Aluminide Manufactured by Electron Beam Melting An Investigation of Microstructural Behavior and Related Mechanical Properties for Aerospace Applications Diploma work in the Master programme Advanced Engineering Material, n.d.

[2] S. Biamino, A. Penna, U. Ackelid, S. Sabbadini, O. Tassa, P. Fino, M. Pavese, P. Gennaro, C. Badini, Electron beam melting of Ti-48Al-2Cr-2Nb alloy: Microstructure and mechanical properties investigation, Intermetallics (Barking) 19 (2011) 776–781. https://doi.org/10.1016/j.intermet.2010.11.017.

[3] A. Mohammad, A.M. Al-Ahmari, A. AlFaify, M.K. Mohammed, Effect of melt parameters on density and surface roughness in electron beam melting of gamma titanium aluminide alloy, Rapid Prototyp J 23 (2017) 474–485. https://doi.org/10.1108/RPJ-12-2014-0187.

[4] S. Biamino, A. Penna, U. Ackelid, S. Sabbadini, O. Tassa, P. Fino, M. Pavese, P. Gennaro, C. Badini, Electron beam melting of Ti-48Al-2Cr-2Nb alloy: Microstructure and mechanical properties investigation, Intermetallics (Barking) 19 (2011) 776–781. https://doi.org/10.1016/j.intermet.2010.11.017.

[5] E. Toyserkani, D. Sarker, F. Liravi, P. Russo, K. Taherkhani, Metal Additive Manufacturing A comprehensive review of additive manufacturing processes for metallic structures, n.d. www.wiley.com.

[6] J. Hernandez, L.E. Murr, S.M. Gaytan, E. Martinez, F. Medina, R.B. Wicker, Microstructures for Two-Phase Gamma Titanium Aluminide Fabricated by Electron Beam Melting, Metallography, Microstructure, and Analysis 1 (2012) 14–27. https://doi.org/10.1007/s13632-011-0001-9.

[7] L. Kourtis, Electron Beam Melting of Titanium Aluminides; Process Development and Material Properties Optimisation I. SUMMARY, 2017.

[8] L.E. Murr, S.M. Gaytan, A. Ceylan, E. Martinez, J.L. Martinez, D.H. Hernandez, B.I. Machado, D.A. Ramirez, F. Medina, S. Collins, R.B. Wicker, Characterization of titanium

aluminide alloy components fabricated by additive manufacturing using electron beam melting, Acta Mater 58 (2010) 1887–1894. https://doi.org/10.1016/j.actamat.2009.11.032.

[9] M. Seifi, A.A. Salem, D.P. Satko, U. Ackelid, S.L. Semiatin, J.J. Lewandowski, Effects of HIP on microstructural heterogeneity, defect distribution and mechanical properties of additively manufactured EBM Ti-48Al-2Cr-2Nb, J Alloys Compd 729 (2017) 1118–1135. https://doi.org/10.1016/j.jallcom.2017.09.163.

[10] T.C. Dzogbewu, W.B. du Preez, Additive manufacturing of ti-based intermetallic alloys: A review and conceptualization of a next-generation machine, Materials 14 (2021). https://doi.org/10.3390/ma14154317.

[11] X. Gong, T. Anderson, K. Chou, Review on powder-based electron beam additive manufacturing Technology, Manuf Rev (Les Ulis) 1 (2014). https://doi.org/10.1051/mfreview/2014001.

[12] C. Körner, Additive manufacturing of metallic components by selective electron beam melting - A review, International Materials Reviews 61 (2016) 361–377. https://doi.org/10.1080/09506608.2016.1176289.

[13] M.S. Węglowski, S. Błacha, A. Phillips, Electron beam welding - Techniques and trends - Review, Vacuum 130 (2016) 72–92. https://doi.org/10.1016/j.vacuum.2016.05.004.

[14] S. Yim, H. Bian, K. Aoyagi, K. Yamanaka, A. Chiba, Effect of powder morphology on flowability and spreading behavior in powder bed fusion additive manufacturing process: A particle-scale modeling study, Addit Manuf 72 (2023). https://doi.org/10.1016/j.addma.2023.103612.

[15] L.C. Zhang, Y. Liu, S. Li, Y. Hao, Additive Manufacturing of Titanium Alloys by Electron Beam Melting: A Review, Adv Eng Mater 20 (2018). https://doi.org/10.1002/adem.201700842.

[16] L.E. Murr, S.M. Gaytan, D.A. Ramirez, E. Martinez, J. Hernandez, K.N. Amato, P.W. Shindo, F.R. Medina, R.B. Wicker, • Invited Review Metal Fabrication by Additive Manufacturing Using Laser and Electron Beam Melting Technologies, 2012.

[17] H.M. Alojaly, A. Hammouda, K.Y. Benyounis, Review of recent developments on metal matrix composites with particulate reinforcement, in: Reference Module in Materials Science

and Materials Engineering, Elsevier, 2023. https://doi.org/10.1016/B978-0-323-96020-5.00041-8.

[18] P.K. Gokuldoss, S. Kolla, J. Eckert, Additive manufacturing processes: Selective laser melting, electron beam melting and binder jetting-selection guidelines, Materials 10 (2017). https://doi.org/10.3390/ma10060672.

[19] B. chao Lin, W. Chen, Mechanical properties of TiAl fabricated by electron beam melting — A review, China Foundry 18 (2021) 307–316. https://doi.org/10.1007/s41230-021-1093-8.

[20] F. Appel, U. Brossmann, U. Christoph, S. Eggert, P. Janschek, U. Lorenz, J. Müllauer, M. Oehring, J.D.H. Paul, Recent Progress in the Development of Gamma Titanium Aluminide Alloys**, n.d.

[21] L. Salou, A. Hoornaert, G. Louarn, P. Layrolle, Enhanced osseointegration of titanium implants with nanostructured surfaces: An experimental study in rabbits, Acta Biomater 11 (2015) 494–502. https://doi.org/10.1016/j.actbio.2014.10.017.

[22] M. Galati, P. Minetola, G. Rizza, Surface roughness characterisation and analysis of the Electron Beam Melting (EBM) process, Materials 12 (2019). https://doi.org/10.3390/ma12132211.

[23] A. Mussatto, R. Groarke, A. O'Neill, M.A. Obeidi, Y. Delaure, D. Brabazon, Influences of powder morphology and spreading parameters on the powder bed topography uniformity in powder bed fusion metal additive manufacturing, Addit Manuf 38 (2021). https://doi.org/10.1016/j.addma.2020.101807.

[24] H.P. Tang, M. Qian, N. Liu, X.Z. Zhang, G.Y. Yang, J. Wang, Effect of Powder Reuse Times on Additive Manufacturing of Ti-6Al-4V by Selective Electron Beam Melting, JOM 67 (2015) 555–563. https://doi.org/10.1007/s11837-015-1300-4.

[25] A.T. Sutton, C.S. Kriewall, M.-C. Leu, J.W. Newkirk, Powders for Additive Manufacturing Processes: Characterization Techniques and Effects on Part Properties, 2016. https://scholarsmine.mst.edu/mec_aereng_facwork.

[26] Y.Y. Sun, S. Gulizia, C.H. Oh, C. Doblin, Y.F. Yang, M. Qian, Manipulation and Characterization of a Novel Titanium Powder Precursor for Additive Manufacturing Applications, JOM 67 (2015) 564–572. https://doi.org/10.1007/s11837-015-1301-3.

[27] P. Mellin, O. Lyckfeldt, P. Harlin, H. Brodin, H. Blom, A. Strondl, Evaluating flowability of additive manufacturing powders, using the Gustavsson flow meter, Metal Powder Report 72 (2017) 322–326. https://doi.org/10.1016/j.mprp.2017.06.003.

[28] V. V. Popov, A. Katz-Demyanetz, A. Garkun, M. Bamberger, The effect of powder recycling on the mechanical properties and microstructure of electron beam melted Ti-6Al-4 V specimens, Addit Manuf 22 (2018) 834–843. https://doi.org/10.1016/j.addma.2018.06.003.

[29] H. Galarraga, D.A. Lados, R.R. Dehoff, M.M. Kirka, P. Nandwana, Effects of the microstructure and porosity on properties of Ti-6Al-4V ELI alloy fabricated by electron beam melting (EBM), Addit Manuf 10 (2016) 47–57. https://doi.org/10.1016/j.addma.2016.02.003.

[30] H. Gong, K. Rafi, H. Gu, G.D. Janaki Ram, T. Starr, B. Stucker, Influence of defects on mechanical properties of Ti-6Al-4V components produced by selective laser melting and electron beam melting, Mater Des 86 (2015) 545–554. https://doi.org/10.1016/j.matdes.2015.07.147.

[31] G. Baudana, S. Biamino, D. Ugues, M. Lombardi, P. Fino, M. Pavese, C. Badini, Titanium aluminides for aerospace and automotive applications processed by Electron Beam Melting: Contribution of Politecnico di Torino, Metal Powder Report 71 (2016) 193–199. https://doi.org/10.1016/j.mprp.2016.02.058.

[32] S.M. Gaytan, L.E. Murr, F. Medina, E. Martinez, M.I. Lopez, R.B. Wicker, Advanced metal powder based manufacturing of complex components by electron beam melting, Materials Technology 24 (2009) 180–190. https://doi.org/10.1179/106678509X12475882446133.

[33] M. Iebba, A. Astarita, D. Mistretta, I. Colonna, M. Liberini, F. Scherillo, C. Pirozzi, R. Borrelli, S. Franchitti, A. Squillace, Influence of Powder Characteristics on Formation of Porosity in Additive Manufacturing of Ti-6Al-4V Components, J Mater Eng Perform 26 (2017) 4138–4147. https://doi.org/10.1007/s11665-017-2796-2.

[34] M. Seifi, A.A. Salem, D.P. Satko, U. Ackelid, S.L. Semiatin, J.J. Lewandowski, Effects of HIP on microstructural heterogeneity, defect distribution and mechanical properties of additively manufactured EBM Ti-48Al-2Cr-2Nb, J Alloys Compd 729 (2017) 1118–1135. https://doi.org/10.1016/j.jallcom.2017.09.163.

[35] S. Tammas-Williams, P.J. Withers, I. Todd, P.B. Prangnell, The Effectiveness of Hot Isostatic Pressing for Closing Porosity in Titanium Parts Manufactured by Selective Electron Beam Melting, Metall Mater Trans A Phys Metall Mater Sci 47 (2016) 1939–1946. https://doi.org/10.1007/s11661-016-3429-3.

[36] R. Cunningham, A. Nicolas, J. Madsen, E. Fodran, E. Anagnostou, M.D. Sangid, A.D. Rollett, Analyzing the effects of powder and post-processing on porosity and properties of electron beam melted Ti-6Al-4V, Mater Res Lett 5 (2017) 516–525. https://doi.org/10.1080/21663831.2017.1340911.

[37] A.B. Spierings, M. Schneider, R. Eggenberger, Comparison of density measurement techniques for additive manufactured metallic parts, Rapid Prototyp J 17 (2011) 380–386. https://doi.org/10.1108/13552541111156504.

[38] S. Tammas-Williams, H. Zhao, F. Léonard, F. Derguti, I. Todd, P.B. Prangnell, XCT analysis of the influence of melt strategies on defect population in Ti-6Al-4V components manufactured by Selective Electron Beam Melting, Mater Charact 102 (2015) 47–61. https://doi.org/10.1016/j.matchar.2015.02.008.

[39] M. Habibnejad-korayem, J. Zhang, Y. Zou, Effect of particle size distribution on the flowability of plasma atomized Ti-6Al-4V powders, Powder Technol 392 (2021) 536–543. https://doi.org/10.1016/j.powtec.2021.07.026.

[40] Y. Zhao, Y. Koizumi, K. Aoyagi, K. Yamanaka, A. Chiba, Characterization of powder bed generation in electron beam additive manufacturing by discrete element method (DEM), 2017. www.sciencedirect.comwww.materialstoday.com/proceedings2214-7853.

[41] D.D. Deligianni, N. Katsala, S. Ladas, D. Sotiropoulou, J. Amedee, Y.F. Missirlis, Effect of surface roughness of the titanium alloy Ti-6Al-4V on human bone marrow cell response and on protein adsorption, 2001.

[42] S. Ponader, E. Vairaktaris, P. Heinl, C. V. Wilmowsky, A. Rottmair, C. Körner, R.F. Singer, S. Holst, K.A. Schlegel, F.W. Neukam, E. Nkenke, Effects of topographical surface modifications of electron beam melted Ti-6Al-4V titanium on human fetal osteoblasts, J Biomed Mater Res A 84 (2008) 1111–1119. https://doi.org/10.1002/jbm.a.31540.

[43] I. Kaur, P. Singh, State-of-the-art in heat exchanger additive manufacturing, Int J Heat Mass Transf 178 (2021). https://doi.org/10.1016/j.ijheatmasstransfer.2021.121600.

[44] L. C. B. Carolo, R.E. Cooper O., A review on the influence of process variables on the surface roughness of Ti-6Al-4V by electron beam powder bed fusion, Addit Manuf 59 (2022). https://doi.org/10.1016/j.addma.2022.103103.

[45] A.H. Chern, P. Nandwana, T. Yuan, M.M. Kirka, R.R. Dehoff, P.K. Liaw, C.E. Duty, A review on the fatigue behavior of Ti-6Al-4V fabricated by electron beam melting additive manufacturing, Int J Fatigue 119 (2019) 173–184. https://doi.org/10.1016/j.ijfatigue.2018.09.022.

[46] G. Nicoletto, R. Konečná, M. Frkáň, E. Riva, Surface roughness and directional fatigue behavior of as-built EBM and DMLS Ti6Al4V, Int J Fatigue 116 (2018) 140–148. https://doi.org/10.1016/j.ijfatigue.2018.06.011.

[47] P. Wang, W.J. Sin, M.L.S. Nai, J. Wei, Effects of processing parameters on surface roughness of additive manufactured Ti-6Al-4V via electron beam melting, Materials 10 (2017). https://doi.org/10.3390/ma10101121.

[48] A. Safdar, H.Z. He, L.Y. Wei, A. Snis, L.E. Chavez De Paz, Effect of process parameters settings and thickness on surface roughness of EBM produced Ti-6Al-4V, Rapid Prototyp J 18 (2012) 401–408. https://doi.org/10.1108/13552541211250391.

[49] R.K. Ek, L.E. Rännar, M. Bäckstöm, P. Carlsson, The effect of EBM process parameters upon surface roughness, Rapid Prototyp J 22 (2016) 495–503. https://doi.org/10.1108/RPJ-10-2013-0102.

[50] M. Rosentritt, S. Schneider-Feyrer, L. Kurzendorfer, Comparison of surface roughness parameters Ra/Sa and Rz/Sz with different measuring devices, J Mech Behav Biomed Mater (2023) 106349. https://doi.org/10.1016/j.jmbbm.2023.106349.

[51] E. Jansons, J. Lungevics, K. Agris Gross, Surface Roughness Measure That Best Correlates to Ease of Sliding, 2016.

[52] G. Shanbhag, M. Vlasea, Powder reuse cycles in electron beam powder bed fusion— variation of powder characteristics, Materials 14 (2021). https://doi.org/10.3390/ma14164602.

[53] H.M. Buckland, J. Saxby, M. Roche, P. Meredith, A.C. Rust, K. V. Cashman, S.L. Engwell, Measuring the size of non-spherical particles and the implications for grain size analysis in volcanology, Journal of Volcanology and Geothermal Research 415 (2021). https://doi.org/10.1016/j.jvolgeores.2021.107257.

[54] Y. Zhao, J.W. Chew, Effect of lognormal particle size distributions on particle spreading in additive manufacturing, Advanced Powder Technology 32 (2021) 1127–1144. https://doi.org/10.1016/j.apt.2021.02.019.

[55] G. Shanbhag, M. Vlasea, The effect of reuse cycles on Ti-6Al-4V powder properties processed by electron beam powder bed fusion, Manuf Lett 25 (2020) 60–63. https://doi.org/10.1016/j.mfglet.2020.07.007.

[56] A. Goyal, V. Sharma, M.K. Sihag, S.K. Tomar, S. Arora, L. Sabikhi, A.K. Singh, Development and physico-chemical characterization of microencapsulated flaxseed oil powder: A functional ingredient for omega-3 fortification, Powder Technol 286 (2015) 527–537. https://doi.org/10.1016/j.powtec.2015.08.050.

[57] E.R.L. Espiritu, A. Kumar, A. Nommeots-Nomm, J.A.M. Lerma, M. Brochu, Investigation of the rotating drum technique to characterise powder flow in controlled and low pressure environments, Powder Technol 366 (2020) 925–937. https://doi.org/10.1016/j.powtec.2020.03.029.

[58] G. Shanbhag, Performance Analytics for Electron Beam Powder Bed Fusion of Ti-6Al-4V, 2021.

[59] A.M. Kiss, A.Y. Fong, N.P. Calta, V. Thampy, A.A. Martin, P.J. Depond, J. Wang, M.J. Matthews, R.T. Ott, C.J. Tassone, K.H. Stone, M.J. Kramer, A. van Buuren, M.F. Toney, J. Nelson Weker, Laser-Induced Keyhole Defect Dynamics during Metal Additive Manufacturing, Adv Eng Mater 21 (2019) 1900455. https://doi.org/10.1002/adem.201900455.

[60] A.M. Rubenchik, W.E. King, S.S. Wu, Scaling laws for the additive manufacturing, J Mater Process Technol 257 (2018) 234–243. https://doi.org/10.1016/j.jmatprotec.2018.02.034.

[61] A. Salazar, On thermal diffusivity You may also like On thermal diffusivity, 2003.

[62] M. Doubenskaia, A. Domashenkov, I. Smurov, P. Petrovskiy, Study of Selective Laser Melting of intermetallic TiAl powder using integral analysis, Int J Mach Tools Manuf 129 (2018) 1–14. https://doi.org/10.1016/j.ijmachtools.2018.02.003.

[63] GE Additive, Inside Electron Beam Melting, (n.d.).

[64] U. Scipioni Bertoli, A.J. Wolfer, M.J. Matthews, J.P.R. Delplanque, J.M. Schoenung, On the limitations of Volumetric Energy Density as a design parameter for Selective Laser Melting, Mater Des 113 (2017) 331–340. https://doi.org/10.1016/j.matdes.2016.10.037.

[65] W.C. Scarfe, A.G. Farman, What is Cone-Beam CT and How Does it Work?, Dent Clin North Am 52 (2008) 707–730. https://doi.org/10.1016/j.cden.2008.05.005.

[66] Y. Chen, H. Yue, X. Wang, Microstructure, texture and tensile property as a function of scanning speed of Ti-47Al-2Cr-2Nb alloy fabricated by selective electron beam melting, Materials Science and Engineering A 713 (2018) 195–205. https://doi.org/10.1016/j.msea.2017.12.020.

[67] The Effect of HIP Treatment on the Mechanical Properties of Titanium Aluminide Additive Manufactured by EBM, in: 2019: pp. 114–120. https://doi.org/10.21741/9781644900031-16.

[68] C. Bellini, F. Berto, R. Borrelli, V. Di Cocco, S. Franchitti, F. Iacoviello, L.P. Mocanu, S.M.J. Razavi, Effects of recycling on defects and microstructure in Ti-6Al-4V powder particles and samples fabricated by Electron Beam Melting process, Procedia Structural Integrity 47 (2023) 359–369. https://doi.org/10.1016/j.prostr.2023.07.088.

[69] K. Cho, H. Kawabata, T. Hayashi, H.Y. Yasuda, H. Nakashima, M. Takeyama, T. Nakano, Peculiar microstructural evolution and tensile properties of β-containing γ-TiAl alloys fabricated by electron beam melting, Addit Manuf 46 (2021). https://doi.org/10.1016/j.addma.2021.102091.

[70] A.M. Rausch, V.E. Küng, C. Pobel, M. Markl, C. Körner, Predictive Simulation of Process Windows for Powder Bed Fusion Additive Manufacturing: Influence of the Powder Bulk Density, Materials 10 (2017). https://doi.org/10.3390/ma10101117.

[71] G. Chen, Q. Zhou, S.Y. Zhao, J.O. Yin, P. Tan, Z.F. Li, Y. Ge, J. Wang, H.P. Tang, A pore morphological study of gas-atomized Ti-6Al-4V powders by scanning electron microscopy

and synchrotron X-ray computed tomography, Powder Technol 330 (2018) 425–430. https://doi.org/10.1016/j.powtec.2018.02.053.

[72] A.M. Rausch, M. Markl, C. Körner, Predictive simulation of process windows for powder bed fusion additive manufacturing: Influence of the powder size distribution, Computers and Mathematics with Applications 78 (2019) 2351–2359. https://doi.org/10.1016/j.camwa.2018.06.029.

[73] A. Bauereiß, T. Scharowsky, C. Körner, Defect generation and propagation mechanism during additive manufacturing by selective beam melting, J Mater Process Technol 214 (2014) 2522–2528. https://doi.org/10.1016/j.jmatprotec.2014.05.002.

[74] C. Pirozzi, S. Franchitti, R. Borrelli, G. Diodati, G. Vattasso, Experimental Study on the Porosity of Electron Beam Melting-Manufactured Ti6Al4V, J Mater Eng Perform 28 (2019) 2649–2660. https://doi.org/10.1007/s11665-019-04038-7.

[75] G.K.L. Ng, A.E.W. Jarfors, G. Bi, H.Y. Zheng, Porosity formation and gas bubble retention in laser metal deposition, Appl Phys A Mater Sci Process 97 (2009) 641–649. https://doi.org/10.1007/s00339-009-5266-3.

[76] A. Mohammad, A.M. Alahmari, M.K. Mohammed, R.K. Renganayagalu, K. Moiduddin, Effect of energy input on microstructure and mechanical properties of titanium aluminide alloy fabricated by the additive manufacturing process of electron beam melting, Materials 10 (2017). https://doi.org/10.3390/ma10020211.

[77] S. Patel, M. Vlasea, Melting modes in laser powder bed fusion, Materialia (Oxf) 9 (2020) 100591. https://doi.org/10.1016/j.mtla.2020.100591.

[78] A.T. Sutton, C.S. Kriewall, M.C. Leu, J.W. Newkirk, Powder characterisation techniques and effects of powder characteristics on part properties in powder-bed fusion processes, Virtual Phys Prototyp 12 (2017) 3–29. https://doi.org/10.1080/17452759.2016.1250605.

[79] Keyence, Introduction to Surface Roughness, (n.d.).

[80] Keyence, Solving the questions about profile and surface roughness measurements! Introduction to Roughness, (n.d.).

[81] B. Vayssette, N. Saintier, C. Brugger, M. Elmay, E. Pessard, Surface roughness of Ti-6Al-4V parts obtained by SLM and EBM: Effect on the High Cycle Fatigue life, in: Procedia Eng, Elsevier Ltd, 2018: pp. 89–97. https://doi.org/10.1016/j.proeng.2018.02.010.

[82] H. Demirtas, A. Cebi, M.T. Aslan, O. Yilmaz, S. Nesli, L. Subasi, A. Gunaydin, G.M. Bilgin, A. Orhangul, G. Akbulut, Electrochemical machining of additively manufactured γ-TiAl parts: post-processing technique to reduce surface roughness, International Journal of Advanced Manufacturing Technology 127 (2023) 2475–2485. https://doi.org/10.1007/s00170-023-11690-w.

[83] A. Phua, P.S. Cook, C.H.J. Davies, G.W. Delaney, Powder spreading over realistic laser melted surfaces in metal additive manufacturing, Additive Manufacturing Letters 3 (2022). https://doi.org/10.1016/j.addlet.2022.100039.

Appendix

Supplementary Tables

Supplementary Table 1. Process parameter selection and calculated energy input for each sample in this study for PSD 45-150µm

Experimental Phase	*Sample No*	*Speed (mm/s)*	*Current (mA)*	*Line offset (mm)*	*Focus Offset (mA)*	*Volumetric Energy Density (mm/s³)*	*Normalized Enthalpy h**
Round 1	Sample 1	1600	12	0.2	20	25.000	12.858
	Sample 2	1600	12	0.3	20	16.667	12.858
	Sample 3	2200	12	0.2	0	18.182	10.318
	Sample 4	1800	12	0.2	0	22.222	11.407
	Sample 5	1600	12	0.2	0	25.000	12.099
	Sample 6	1600	8	0.2	0	16.667	8.066
	Sample 7	1600	10	0.2	0	20.833	10.082
	Sample 8	1300	12	0.2	25	30.769	13.066
	Sample 9	1400	12	0.2	20	28.571	13.745
Round 2: Run 1	Sample 1	1000	8	0.2	0	26.667	10.203
	Sample 2	1000	8	0.2	10	26.667	11.451
	Sample 3	1000	8	0.2	20	26.667	10.843
	Sample 4	1500	8	0.2	0	17.778	8.330
	Sample 5	1500	10	0.2	10	22.222	11.688
	Sample 6	1500	12	0.2	20	26.667	13.279
	Sample 7	1500	12	0.2	0	26.667	12.496
	Sample 8	1500	12	0.2	20	26.667	13.279
	Sample 9	2000	10	0.2	0	16.667	9.018
	Sample 10	2000	10	0.2	20	16.667	9.584
	Sample 11	800	12	0.2	0	50.000	17.110
	Sample 12	800	12	0.2	20	50.000	18.183
Round 2: Run 2	Sample 1	800	7	0.2	0	29.167	9.981
	Sample 2	800	7	0.2	10	29.167	11.203
	Sample 3	800	7	0.2	20	29.167	10.607
	Sample 4	1300	7	0.2	0	17.949	7.830
	Sample 5	1300	7	0.2	10	17.949	8.788
	Sample 6	1300	7	0.2	20	17.949	8.321
	Sample 7	2000	7	0.2	0	11.667	6.313
	Sample 8	2000	7	0.2	10	11.667	7.085
	Sample 9	2000	7	0.2	20	11.667	6.708
	Sample 10	800	10	0.2	0	41.667	14.259
	Sample 11	800	10	0.2	10	41.667	16.004
	Sample 12	800	10	0.2	20	41.667	15.153
	Sample 13	1300	10	0.2	0	25.641	11.185
	Sample 14	1300	10	0.2	10	25.641	12.554

	Sample 15	1300	10	0.2	20	25.641	11.887
	Sample 16	2000	10	0.2	0	16.667	9.018
	Sample 17	2000	10	0.2	10	16.667	10.122
	Sample 18	2000	10	0.2	20	16.667	9.584
	Sample 19	1300	10	0.1	0	51.282	11.185
	Sample 20	1300	10	0.1	10	51.282	12.554
	Sample 21	1300	10	0.1	20	51.282	11.887
Round 2: Run 3	Sample 1	1000	10	0.3	0	22.222	12.753
	Sample 2	1000	7	0.3	0	15.556	8.927
	Sample 3	1000	10	0.1	0	66.667	12.753
	Sample 4	2000	10	0.1	20	33.333	9.584
	Sample 5	1000	7	0.3	20	15.556	9.487
	Sample 6	2000	7	0.3	20	7.778	6.708
	Sample 7	1500	8.5	0.2	10	18.889	9.934
	Sample 8	1000	7	0.1	0	46.667	8.927
	Sample 9	2000	10	0.3	20	11.111	9.584
	Sample 10	2000	10	0.1	0	33.333	9.018
	Sample 11	2000	7	0.1	20	23.333	6.708
	Sample 12	2000	7	0.3	0	7.778	6.313
	Sample 13	2000	7	0.1	0	23.333	6.313
	Sample 14	2000	10	0.3	0	11.111	9.018
	Sample 15	1000	10	0.1	20	66.667	13.553
	Sample 16	1500	8.5	0.2	10	18.889	9.934
	Sample 17	1000	7	0.1	20	46.667	9.487
	Sample 18	1500	8.5	0.2	10	18.889	9.934
	Sample 19	1000	10	0.3	20	22.222	13.553
	Sample 20	1500	8.5	0.25	10	15.111	9.934
	Sample 21	1500	8.5	0.05	10	75.556	9.934
	Sample 22	1500	8.5	0.08	10	47.222	9.934
	Sample 23	1500	8.5	0.1	10	37.778	9.934
	Sample 24	1500	8.5	0.15	10	25.185	9.934
Round 2: Run 4	Sample 1	2000	18	0.3	20	17.250	20
	Sample 2	2500	15	0.2	10	13.580	20
	Sample 3	2000	18	0.1	20	17.250	60
	Sample 4	2000	12	0.3	20	11.500	13.333
	Sample 5	3000	12	0.3	20	9.390	8.8889
	Sample 6	2000	18	0.3	0	16.232	20
	Sample 7	3000	18	0.3	0	13.254	13.33
	Sample 8	3000	12	0.1	20	9.390	26.667
	Sample 9	3000	12	0.1	0	8.836	26.667
	Sample 10	2000	12	0.1	20	11.500	40
	Sample 11	2500	15	0.2	10	13.580	20
	Sample 12	2000	18	0.1	0	16.232	60
	Sample 13	3000	12	0.3	0	8.836	8.889
	Sample 14	2000	12	0.1	0	10.822	40
	Sample 15	3000	18	0.3	20	14.085	13.333
	Sample 16	2000	12	0.3	0	10.822	13.333
	Sample 17	3000	18	0.1	0	13.254	40

	Sample 18	3000	18	0.1	20	14.085	40
	Sample 19	2500	15	0.2	10	13.580	20
Round 2: Run 5	Sample 1	4000	20	0.1	0	33.333	8.262
	Sample 2	4000	25	0.3	0	13.889	10.327
	Sample 3	3500	22.5	0.2	10	21.429	8.685
	Sample 4	3000	25	0.1	0	55.556	11.925
	Sample 5	3500	22.5	0.2	10	21.429	8.685
	Sample 6	3000	20	0.1	0	44.444	9.540
	Sample 7	4000	20	0.3	20	11.111	6.160
	Sample 8	3000	20	0.1	20	44.444	7.113
	Sample 9	3000	25	0.3	20	18.519	8.891
	Sample 10	4000	20	0.3	0	11.111	8.262
	Sample 11	3000	25	0.3	0	18.519	11.925
	Sample 12	4000	25	0.1	20	41.667	7.700
	Sample 13	3000	25	0.1	20	55.556	8.891
	Sample 14	4000	25	0.3	20	13.889	7.700
	Sample 15	4000	25	0.1	0	41.667	10.327
	Sample 16	4000	20	0.1	20	33.333	6.160
	Sample 17	3000	20	0.3	0	14.815	9.540
	Sample 18	3500	22.5	0.2	10	21.429	8.685
	Sample 19	3000	20	0.3	20	14.815	7.113
	Sample 20	3500	22.5	0.2	10	21.429	8.685
	Sample 21	3500	22.5	0.2	10	21.429	8.685
	Sample 24	3500	22.5	0.2	10	21.429	8.685

Supplementary Table 2. Process parameter selection and calculated energy input for each sample in this study for 38-180µm

Experimental Phase	***Sample No***	***Speed (mm/s)***	***Current (mA)***	***Line offset (mm)***	***Focus Offset (mA)***	***Volumetric Energy Density (mm/s³)***	***Normalized Enthalpy h****
Round 2: Run 1	Sample 1	1000	10	0.3	0	22.222	12.753
	Sample 2	1000	7	0.3	0	15.556	8.927
	Sample 3	1000	10	0.1	0	66.667	12.753
	Sample 4	2000	10	0.1	20	33.333	9.584
	Sample 5	1000	7	0.3	20	15.556	9.487
	Sample 6	2000	7	0.3	20	7.778	6.708
	Sample 7	1500	8.5	0.2	10	18.889	9.934
	Sample 8	1000	7	0.1	0	46.667	8.927
	Sample 9	2000	10	0.3	20	11.111	9.584
	Sample 10	2000	10	0.1	0	33.333	9.018
	Sample 11	2000	7	0.1	20	23.333	6.708
	Sample 12	2000	7	0.3	0	7.778	6.313

	Sample 13	2000	7	0.1	0	23.333	6.313
	Sample 14	2000	10	0.3	0	11.111	9.018
	Sample 15	1000	10	0.1	20	66.667	13.553
	Sample 16	1500	8.5	0.2	10	18.889	9.934
	Sample 17	1000	7	0.1	20	46.667	9.487
	Sample 18	1500	8.5	0.2	10	18.889	9.934
	Sample 19	1000	10	0.3	20	22.222	13.553
	Sample 20	1500	8.5	0.25	10	15.111	9.934
	Sample 21	1500	8.5	0.05	10	75.556	9.934
	Sample 22	1500	8.5	0.08	10	47.222	9.934
	Sample 23	1500	8.5	0.1	10	37.778	9.934
	Sample 24	1500	8.5	0.15	10	25.185	9.934
Round 2: Run 2	Sample 1	2000	18	0.3	20	17.250	20
	Sample 2	2500	15	0.2	10	13.580	20
	Sample 3	2000	18	0.1	20	17.250	60
	Sample 4	2000	12	0.3	20	11.500	13.333
	Sample 5	3000	12	0.3	20	9.390	8.8889
	Sample 6	2000	18	0.3	0	16.232	20
	Sample 7	3000	18	0.3	0	13.254	13.33
	Sample 8	3000	12	0.1	20	9.390	26.667
	Sample 9	3000	12	0.1	0	8.836	26.667
	Sample 10	2000	12	0.1	20	11.500	40
	Sample 11	2500	15	0.2	10	13.580	20
	Sample 12	2000	18	0.1	0	16.232	60
	Sample 13	3000	12	0.3	0	8.836	8.889
	Sample 14	2000	12	0.1	0	10.822	40
	Sample 15	3000	18	0.3	20	14.085	13.333
	Sample 16	2000	12	0.3	0	10.822	13.333
	Sample 17	3000	18	0.1	0	13.254	40
	Sample 18	3000	18	0.1	20	14.085	40
	Sample 19	2500	15	0.2	10	13.580	20
Round 2: Run 3	Sample 1	4000	20	0.1	0	33.333	8.262
	Sample 2	4000	25	0.3	0	13.889	10.327
	Sample 3	3500	22.5	0.2	10	21.429	8.685
	Sample 4	3000	25	0.1	0	55.556	11.925
	Sample 5	3500	22.5	0.2	10	21.429	8.685
	Sample 6	3000	20	0.1	0	44.444	9.540
	Sample 7	4000	20	0.3	20	11.111	6.160
	Sample 8	3000	20	0.1	20	44.444	7.113
	Sample 9	3000	25	0.3	20	18.519	8.891
	Sample 10	4000	20	0.3	0	11.111	8.262
	Sample 11	3000	25	0.3	0	18.519	11.925
	Sample 12	4000	25	0.1	20	41.667	7.700
	Sample 13	3000	25	0.1	20	55.556	8.891
	Sample 14	4000	25	0.3	20	13.889	7.700
	Sample 15	4000	25	0.1	0	41.667	10.327
	Sample 16	4000	20	0.1	20	33.333	6.160
	Sample 17	3000	20	0.3	0	14.815	9.540

Sample 18	3500	22.5	0.2	10	21.429	8.685
Sample 19	3000	20	0.3	20	14.815	7.113
Sample 20	3500	22.5	0.2	10	21.429	8.685
Sample 21	3500	22.5	0.2	10	21.429	8.685
Sample 24	3500	22.5	0.2	10	21.429	8.685